ISSN 0915-6348

NATIONAL INSTITUTE FOR FUSION SCIENCE

Frontiers in Pluse-Power-based High Energy Density Plasma Physics and Its Applications

(Ed.) K. Horioka

(Received - Feb. 20, 2008)

NIFS-PROC-72 Mar. 2007

RESEARCH REPORT
NIFS-PROC Series

TOKI, JAPAN

Frontiers in Pulse-Power-based High Energy Density Plasma Physics and Its Applications

Edited by Kazuhiko Horioka

March 5-6, 2007
National Institute for Fusion Science,
Toki, Gifu, Japan

Abstract

The papers in this volume of report were presented at the Symposium on "Frontiers in Pulse-power-based High Energy Density Physics" held by National Institute for Fusion Science. The topics include the present status of high energy density plasma researches, extreme ultraviolet sources, intense radiation sources, high power ion beams, and R&D of related pulse power technologies.

Keywards: plasma, high energy density, pulse power, radiation source, extreme ultraviolet source, plasma focus, charged particle beams

PREFACE

The symposium “Frontiers in High Energy Density Plasma Physics and Its Applications” was organized as a collaboration research program of National Institute for Fusion Sciences (NIFS). It was held March 5-6, 2007 at NIFS Toki. During the symposium, 24 papers were presented and totally 36 people attended this symposium. This issue of report contains a collection of papers dedicated to Dr. Teruhiko Tazima on the occasion of his retirement from NIFS.

The research program started in 1990, and the efforts have been continuously made for more than 15 years. The purpose of this symposium has been to provide a forum to discuss important technical developments, increased understandings, new trends and the prospect on the future of high energy density research as well as the issues of pulsed power technology. Keeping this field active and attractive has been of primary concern for all of the organizing members of this collaboration program. I believe that this symposium can provide that kind of opportunity for all of the attended people, especially for young scientists.

I would like to express my sincere thanks to all of the participants, advisory council of NIFS. In particular, on behalf of organizing members of this program, I wish express our special thanks to Dr. Teruhiko Tazima, for keeping this collaborating works active and valuable. He started research activities in this field more than 15years ago, using pulse power generator LIMAY-I at the Institute of Plasma Physics, Nagoya University. After the move of the institute to Toki, he has also made tremendous and substantial contributions for coordination of activities in this field at NIFS.

Kazuhiko Horioka
Department of Energy Sciences,
Tokyo Institute of Technology

NIFS 2007 Coordinated Research (Symposium)
Project Title: Frontiers in Pulse-power based High Energy Density Plasma Physics
Project ID: NIFS06KKGJ002
NIFS Contact Person: Dr. Teruhiko Tazima

PROGRAM

March 5 (Conference Room, Research Building 1)

Introductory Talk
Kazuhiko Horioka

[Pulse Powered Radiation Source] **Chair: Eiki Hotta**

Development of High Power Pumping System for Capillary Discharge EUV Laser
Yusuke Sakai, Takanori Komatsu, Masato Watanabe, Akitoshi Okino and Eiki Hotta

Research on Z-pinch Type Plasma EUV Source
N.Kishi, N.Iizuka, J.Fei, S.Orishimo, A.Okino, M.Watanabe, T.Kawamura, K.Horioka and E.Hotta

Plasma Control for Efficient Extreme Ultra-violet Source
Kensaku Takahashi, Mitsuo Nakajima, Tohru Kawamura, Makoto Shiho, Eiki Hotta and Kazuhiko Horioka

Experimental Study of Z-pinch Xenon Plasma Dynamics for Extreme Ultraviolet Source
S.Katsuki, N.Tomimaru, H.Imamura, T.Namihira, T.Sakugawa, H.Akiyama

Formation of X-Ray Point Source in the Gas-puff Plasma Focus Experiment
Keiichi Takasugi and Ena Kiuchi

Development of High Repetition Rate Marx Generator
K.Igawa, H.Ontachi, I.Kitamura, H.Ito and K.Masugata

[Pulse Power Technology] **Chair: Hidenori Akiyama**

Evaluation of Switching Characteristics of SiC-JFET for Pulsed Power Application
Kazumasa Narita, Hirokazu Honma, Tomoyuki Yokoo, Weihua Jiang

Repetitive Pulsed Power Generation using Semiconductor Opening Switch
Kunihiko Saiki, Tomoyuki Yokoo, Kazuaki Hotta, and Weihua Jiang

Spectroscopic Measurements in 120kJ Plasma Focus Device
T.Uchida, K.Shimoda and M.Sato

[Special Lecture] **Chair: Kazuhiko Horioka**

Memory of the Pulse Power Researches and Nuclear Fusion
Teruhiko Tazima

March 6 (Conference Room, Research Building 1)

[Pulse Power Technology and Applications] **Chair: Tsutomu Takahashi**

Control of Atmospheric Pressure Transient Glow Discharge in Microgap Electrodes utilizing High Voltage Generator
S.Ibuka, F.Furuya, K.Ogura, K.Yasuoka and S.Ishii
Generation of Microplasmas using Electrolyte Cathode at Atmospheric Pressure
N.Shirai, K.Matsui, S.Ibuka, K.Yasuoka and S.Ishii

[Microwaves and Intense Ion Beams] **Chair: Keiichi Kamada**

A Study on External Magnetic Field and Power Export for High-power Magnetron with ETIGO IV
H.Yamazaki, K.Hashimoto, M.Daimon and Weihua Jiang
Conversion of 5 GHz High Power Microwave to Gaussian Beam with Quasi Optical Anntena
Tomoaki Kurihara, Masatoshi Ohbayashi and Ritoku Ando
Evaluation of Pulse Ion Beam Ability in the Middle Energy Plasma Focus for Material Engineering
H.R.Yousefi, Y.Nakata, H.Ito and K.Masugata

[Ion Beams, Neutron Sources] **Chair: Keiichi Takasugi, Morihiko Sato**

Observation of Neutron Flux Produced in Plasma Focus
Y.Nakata, T.Mizuno, H.R.Youseifi, I.Kitamura, H.Ito and K.Masugata
Evaluation of Bipolar Pulse Generator for High-purity Pulsed Ion Beam
H.Ito, I.Kitamura and K.Masugata
Diagnosis of Pulsed Heavy Ion Beam by Magnetically Insulated Ion Diode
H.Miyake, T.Ebie, R.Ou, I.Kitamura, H.Ito and K.Masugata

[Intense Charged Particle Beams] **Chair: Katsumi Masugata**

3D Simulation of Negative Ion Beams for NBI
W.Jiang, T.Yoshiji, K.Tsumori, O.Kaneko
Effect of Longitudinal Self-Electric Field during Pulse Compression for High-Current Heavy-Ion Beams
Takashi Kikuchi, Shigeo Kawata and Kazuhiko Horioka

Beam Manipulation with Controllable Induction Voltage Cell
Takato Ishii, Toru Sasaki, Mitsuo Nakajima, Tohru Kawamura and Kazuhiko Horioka

[High Energy Density Plasma] **Chair: Takashi Kikuchi**

Simulation on Energy Deposition Process due to Anisotropic Fast Electron Transport in High Density Plasma
Wataru Sekine, Mitsuo Nakajima, Kazuhiko Horioka and Tohru Kawamura
Quasi-uniform Tamped Target for Beam-driven Warm Dense Matter Experiments
Toru Sasaki, Takashi Kikuchi, Mitsuo Nakajima, Tohru Kawamura and Kazuhiko Horioka
Evaluating Conductivity of Warm Dense Matter using Wire Discharges in Water
Yuuri Yano, Toru Sasaki, Mitsuo Nakajima, Tohru Kawamura and Kazuhiko Horioka

Concluding Remarks
Teruhiko Tazima

CONTENTS

List of participants

Aizawa.K	Kanazawa University
Akiyama.H	Kumamoto University
Ando.R	Kanazawa University
Ito.H	Toyama University
Igawa.K	Toyama University
Ibuka.S	Tokyo Institute of Technology
Ishii.T	Tokyo Institute of Technology
Uchida	Gunma University
Ozaki.T	National Institute for Fusion Science
Ohbayashi.M	Kanazawa University
Kamada.K	Kanazawa University
Kawamura.M	Kanazawa University
Katsuki.S	Kumamoto University
Kishi.N	Tokyo Institute of Technology
Kikuchi.T	Utsunomiya University
Kurihara.T	Kanazawa University
Komatsu.T	Tokyo Institute of Technology
Saiki.K	Nagaoka University of Technology
Sato.M	Gunma University
Sasaki.T	Tokyo Institute of Technology
Jiang.W	Nagaoka University of Technology
Shirai.N	Tokyo Institute of Technology
Sekine.W	Tokyo Institute of Technology
Takasugi.K	Nihon University
Takahashi.K	Tokyo Institute of Technology
Takahashi.T	Nihon University
Tazima.T	National Institute for Fusion Science
Nakata.Y	Toyama University
Narita.K	Nagaoka University of Technology
Hotta.E	Tokyo Institute of Technology
Horioka.K	Tokyo Institute of Technology
Masugata.K	Toyama University
Miyake.H	Toyama University
Yada.K	Kanazawa University
Yamazaki.H	Nagaoka University of Technology
Yano.Y	Tokyo Institute of Technology
Yousefi.H.R	Toyama University

DEVELOPMENT OF HIGH POWER PUMPING SYSTEM FOR CAPILLARY DISCHARGE EUV LASER

Yusuke Sakai, Takanori Komatsu, Masato Watanabe, Akitoshi Okino and Eiki Hotta

Department of Energy Sciences, Tokyo Institute of Technology,
4259-J2-35, Nagatsuta, Midori-ku, Yokohama 226-8502, Japan

ABSTRACT

Development of high power pumping system for capillary discharge soft X-ray laser is reported. The pulsed power system consists of a 2.2 μF LC generator, a 2:54 step-up transformer and a 3 nF water capacitor. Taking advantage of high efficiency configuration, step-up ratio of water capacitor voltage to LC generator initial voltage is about 40 times. Consequently, obtained water capacitor voltage reaches about 450 kV when LC generator was charged to 12.5 kV. As a consequent, possibility of charging a water capacitor to 1 MV is demonstrated. With this extremely compact system, discharge current could be increased to nearly 100 kA through moderately long capillary, which leads to generation of high-density and high-temperature plasma column in order to realize EUV laser.

I. Introduction

Wavelength of the laser has been shortened to soft X-ray region with technological advancement of recent years. Owing to its high coherence, high brilliance and short wavelength, the soft X-ray laser shows strong interaction with matter on the atomic and molecular level. It is strongly expected to apply to wide range of the field such as a nanotechnology, a life science and elucidation of physical or chemical phenomena. Much effort has been made to realize soft X-ray lasers with shorter wavelengths. Lasing of saturated short wavelength soft-Xray laser was demonstrated at the wavelength as short as 5.9 nm Ni-like Dy(1). However, the life time of the excited states of the lasing medium is so short, required pumping power is increased inversely proportional to 4^{th} power of its wavelength. Moreover, absorption, divergence or broadening of the radiation through the high energy density plasma are so significant that the pumping power required should be higher. Therefore, pumping devices becomes extremely large in size such as high power pumping lasers used for production of high-density high-temperature plasma and it is still difficult to generate highly uniform long plasma columns by utilizing these laser pumping schemes. More recently, lasing of saturated Ni-like ions soft-X-ray laser at wavelengths ranging from 16.5 nm to 10.9 nm using chirped-pulse Ti saphire laser system by optimizing the angle of incidence for maximum energy deposition was reported(2). Although, it is still difficult to amplify soft-X-ray lasers in plasma ablated by high power lasers.

In 1994, utilizing fast capillary discharge scheme, lasing of 46.9 nm Ne-like Ar highly saturated soft X-ray laser was demonstrated by J.J. Rocca et al(3). In this scheme, using magnetic force of fast capillary discharge, hot and dense long plasma column is generated, where amplification of radiation is obtained by collisional excitation. A particle number density of about 5 X 10^{19} cm^{-3} and a plasma temperature of about 60–90 eV is efficiently generated by fast current pulse of about a few tens of kiloampere in a few hundreds ns. Taking advantage of the pulsed power system consisting of a Marx generator, a water capacitor and a gap switch, it can be possible to generate such a high-density and high-temperature long plasma column by only several hundreds kilojoule in a laboratory scale. In 2001, in addition to effective use of preliminary discharge to generate highly uniform plasma column, utilizing the pulse compression system that consists of a 2:28 step-up pulse transformer between a Marx generator and a water capacitor, highly reproducible lasing of 46.9 nm Ne-like Ar laser was demonstrated by Niimi et al., which leads to pumping system being smaller in size(4). More recently, in 2005, making use of a very low inductance co-axial configuration without Marx generator, the lasing of 46.9 nm laser at 12 Hz repetition rate was also demonstrated, resulting

in significant decrease of the size of pumping device to desk-top size(5).

Also, to realize the lasing pumped by capillary discharge with shorter wavelengths, a 13.2 nm Ni-like Cd soft-X-ray laser and, making use of recombination scheme, amplification of 18.2 nm H-like C VI line were reported(6-8). However, there are no demonstration of amplifying these EUV soft-X-ray lasers up to saturation, because it is not easy to generate highly uniform long plasma column, which is suitable for amplification, of about a few tens of centimeters with higher-density and higher-temperature than that used for 46.9 nm Ne-like Ar laser. Additionally, there is no mirror appropriate for these soft-X-ray lasers, so that application of these laser is limited.

To shorten the wavelength of a laser and to promote application of soft X-ray laser pumped by capillary discharge scheme, we are investigating the possibility of an H-like N recombination pumped soft X-ray laser, the wavelength of which is 13.4 nm emitted by quantum transition from n = 3 to n = 2. This EUV laser is so attractive because of existence of a Mo/Si multi-layer mirror capable of focusing the laser for application. The possibility of realizing an H-like N recombination laser by capillary discharge has been reported by Vrba et al(9). To realize the 13.4 nm soft X-ray laser, it is estimated that required plasma temperature is a few hundreds eV to ionize nitrogen to NVIII and particle number density is the order of 1.0 X 10^{20}cm^{-3} to initiate lasing in the plasma column, which needs discharge current of nearly 100 kA. So as to generate such a high discharge current through a long capillary of about a few tens of centimeters to achieve enough gain length product for EUV laser, because the stray inductance of the load capillary should be large, the water capacitor voltage is necessarily to be large enough. To this end, in this paper, development of a new high-power, and high-efficient pulse power system which is capable of charging the water capacitor to 1 MV in order to generate high discharge current through the long capillary plasma column is reported.

II. Experimental set-up

Developed pulsed power system mainly consists of a 2.2 μF two stage LC generator, a 2:54 step-up pulse transformer and a 3 nF water capacitor as shown in Fig.1. Minimizing inductance which exists between the LC generator and the water capacitor, it can be possible to transfer a large amount of energy of about several hundreds Joules, from the 2.2 μF primary capacitor to the 3 nF secondary capacitor rapidly. The inductance is chiefly composed of stray inductance of transmission line and leakage inductance of a high voltage step-up transformer. Making use of the 24 RG-8U coaxial cable in parallel and parallel plate with high aspect ratio, the stray inductance of a transmission line can be minimized to about 350 nH. In addition, by pressurizing 2 atm SF_6 gas to increase dielectric strength, it is allowed to decrease the space which exists between the primary windings and secondary windings of step-up transformer. As a result, the leakage inductance of the high voltage step-up transformer can be minimized to around 350 nH. Consequently, total inductance related to charging of the water capacitor succeeded to be reduced to nearly 700 nH, resulting rapid charging of a water capacitor within 3 μs. Thanks to such rapid charging, it is possible to minimize energy loss, caused by natural discharge through the water, to several percent approximately.

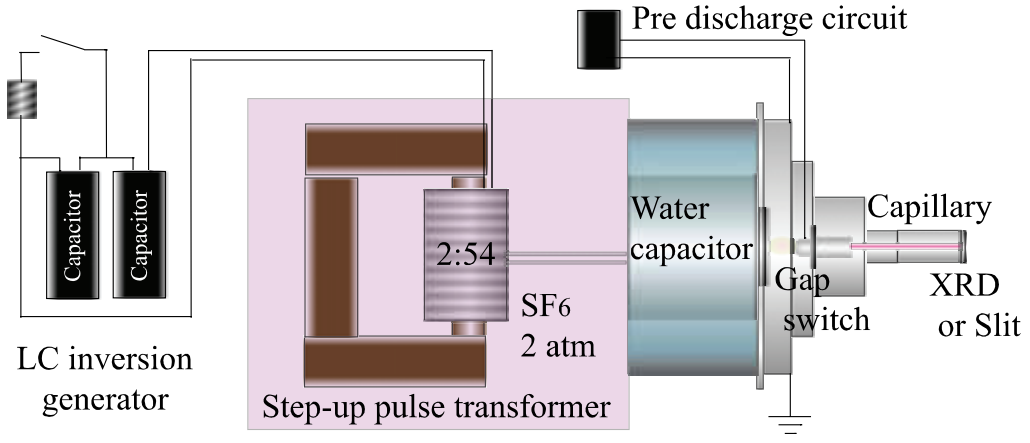

Fig.1 The pulsed power system consisted of a LC generator, a step-up transformer and a water capacitor.

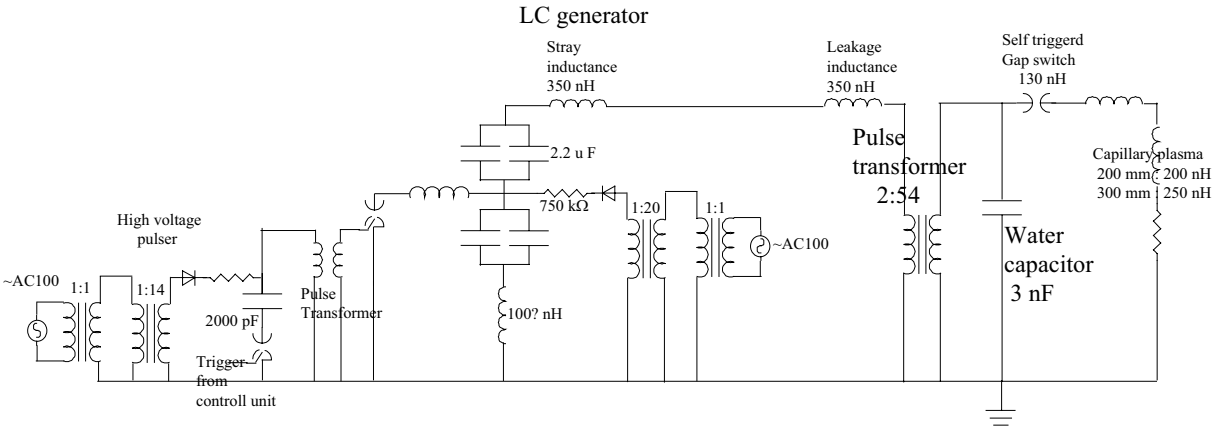

Fig. 2 Circuit of pulsed power system

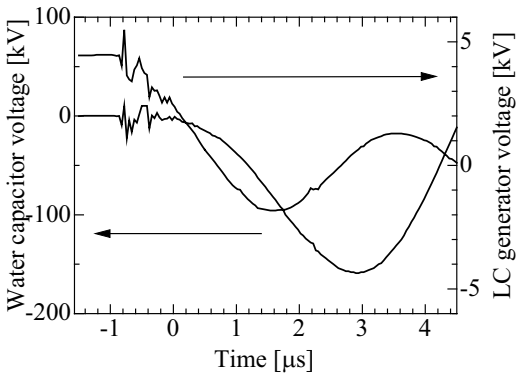

Fig.3 Step-up ratio of a water capacitor voltage to the LC generator.

Moreover, owing to 2:54 pulse transformer, required out-put voltage of the primary LC generator becomes lower to several tens of kirovolts. This moderately low out-put voltage can avoid core saturation of the pulse transformer. Additionally, it makes initial charging system of LC generator and transmission line from the LC generator to the transformer greatly compact. Furthermore, with the help of only one external trigger gap switch used for two stage LC generator, reproducibility of discharge is improved and energy loss through the gap switch is greatly reduced compared to conventional Marx generator. With this extremely compact and efficient pulsed power system consisted of a 2.2 uF LC generator and a 2:54 pulse transformer, the 3 nF water capacitor is able to be charged to approaching 1 MV by only a few tens of initial charging voltage in a capacitor of LC generator.

III. Results and discussion

Out put characteristics of water capacitor voltage and capillary discharge current were conducted. Step-up ratio of water capacitor voltage to initial charging voltage of the LC generator was measured by using capacitive divider as shown in Fig. 3. Initially, a capacitor of LC generator was charged to 4.5 kV and the gap switch of the generator was switched on, then charging of the water capacitor was started. Obtained water capacitor voltage was reached to 160 kV and energy stored in LC generator was transferred to a water capacitor within 3 μs. This rapid charging of water capacitor minimize energy loss of water capacitor and avoid saturation of the core used for pulse transformer. Taking advantage of two stage LC generator with one triggered gap switch and low leakage inductance transformer, 45 % of energy stored in a LC generator initially was transferred to water capacitor. Owing to the high efficiency water capacitor charging system, step-up ratio respect to a LC generator is reaches to 40 times approximately.

To examine the possibility of charging of a water capacitor to 1 MV, in order to generate capillary discharge current of about 100 kA through the long capillary, capillary discharge experiment was performed at moderately high voltage. Initially, a capacitor of LC generator was charged to 12.5 kV and a externally trigger gap switch was closed to start charging of the water capacitor. After that, when the water capacitor voltage was reached to near the peak voltage, a self-breakdown gap switch, connecting the water capacitor and the capillary load, was closed and capillary discharge starts. In this experiment, self-breakdown gap switch was closed when charging voltage reaches 450 kV as shown in Fig.4. Subsequently, obtained capillary

discharge wave

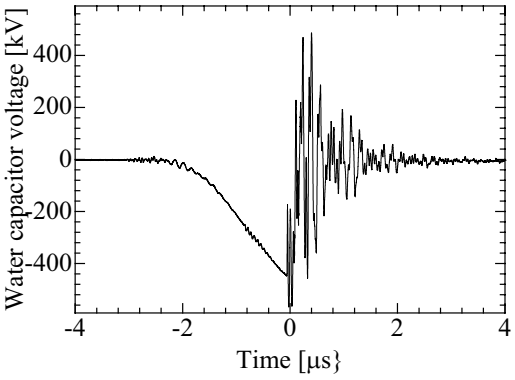

Fig.4 Water capacitor voltage with self-breakdown gap switch closed.

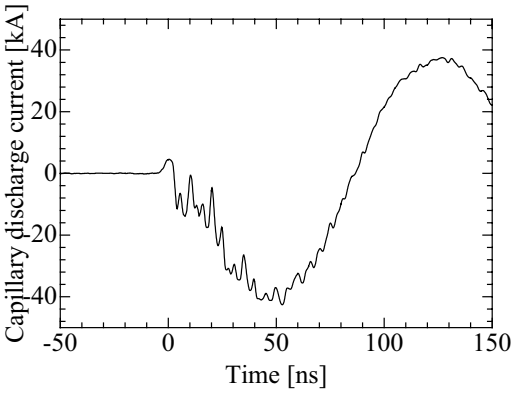

Fig.5 Capillary discharge current when a water capacitor was charged to 450 kV

form is shown in Fig. 5. Peak amplitude of discharge current was nearly 40 kA with half cycle duration of about 100 ns. Accordingly, with careful modification of entire system, to increase dielectric strength, which is tolerable to such a high voltage, if initial voltage of LC generator was increased twice, water capacitor voltage could be able to reach 1 MV. As a consequent, discharge current would approach to nearly 100 kA, which lead to generation of high density and high temperature long plasma column in order to realize EUV laser.

IV. Summary

Development of high power capillary discharge pulsed power system for realizing EUV laser is reported. The pulsed power system consists of 2.2 μF LC generator, 2:54 step-up transformer and 3 nF water capacitor. Step-up ratio of water capacitor voltage to LC generator voltage was measured to about 40 times with this high efficiency charge transfer system of about 45 %. Further, when LC generator was charged to 12.5 kV, obtained water capacitor voltage reached 450 kV and subsequent capillary discharge current was nearly 40 kA. As a result, the possibility of charging of water capacitor voltage to 1 MV in order to increase discharge current up to 100 kV, which is required to realize EUV laser, is demonstrated.

V. References

(1) R. Smith, G. J. Tallents, J. Zhang, G. Eker, S. McCabe, G. J.Pert, and E. Wolfrum : “Saturation behavior of two x-ray lasing transitions in Ni-like Dy”, Phys. Rev. A, Vol.59, R47 (1999)

(2) Wang, M. A. Larotonda, B. M. Luther, D. Alessi, M. Berrill, V. N. Shlyaptsev, and J. J. Rocca : “Demonstration of high-repetition-rate tabletop soft-x-ray lasers with saturated output at wavelengths down to 13.9 nm and gain down to 10.9 nm”, Phys. Rev. A, Vol.72, No.5, pp 053807 (2005)

(3) J. J. Rocca, V. Shlyaptsev, F. G. Tomasel, O. D. Cortazar, D. Hartshorn and J. L. A. Chilla : “Demonstration of a Discharge Pumped Table-Top Soft X-ray Laser”, Phys. Rev. Lett., Vol.73, pp. 2192-2195 (1994)

(4) G. Niimi, Y. Hayashi, N. Sakamoto, M. Nakajima, A. Okino, M. Watanabe, K. Horioka, and E. Hotta : “Development and Characterization of a Low Current Capillary Discharge for X-ray Laser Studies”, IEEE Trans. Plasma Sci., Vol.30, pp. 616-621 (2001)

(5) S. Heinbuch, M. Grisham, D. Marts, and J.J. Rocca : “Demonstration of a desk-top size repetition rate soft x-ray laser”, Optics express, Vol.13, No. 11 (2005)

(6) J.J. Rocca, J.L.A Chilla, S. Sakadzic, A. Rahman, J. Filevich, E. Jankowska, E.C. Hammarsten and B. Luther : “Advances in capillary discharge soft x-ray laser research”, Proceedings of SPIE, Vol. 4505 pp. 1-13 (2001)

(7) Hyun-Joon Shin, Dong-Eon Kim and Tong-Nyong Lee : “Soft-x-ray amplification in a capillary discharge”, Phys. Rev. Lett. E, Vol.50, pp. 1376-1384 (1994)

(8) S S Ellwi, L Juschkin, S Ferri, H-J Kunze, K Koshelev and E Louis : “X-ray lasimg as a result of an induced instability in an ablative capillary discharge”, J.Phys.D:Appl.Phys., Vol.34, pp. 336-339 (2001)

(9) Pavel Vrba, Miroslava Vrbova, Nadezhda A. Bobrova and Pavel V. Sasorov : “Modeling of a nitrogen x-ray laser pumped by capillary discharge”, Central European Journal of Physics, Vol.3, pp. 564-580 (2005)

Plasma Control for Efficient Extreme Ultra-Violet Source

Kensaku Takahashi, Mitsuo Nakajima, Tohru Kawamura, Makoto Shiho, Eiki Hotta, and Kazuhiko Horioka
Department of Energy Sciences, Interdisciplinary Graduate School of Science and Engineering, Tokyo Institute of Technology, 4259 Nagatsuta, Midori-ku, Yokohama 226-8502, Japan

To generate a high efficiency extreme-ultraviolet (EUV) source, effects of plasma shape for controlling radiative plasmas based on xenon capillary discharge are experimentally investigated. The radiation characteristics observed via tapered capillary discharge are compared with those of straight one. From the comparison, the long emission period and different plasma behaviors of tapered capillary discharge are confirmed. This means that control of the plasma geometry is effective for prolonging the EUV emission period. This result also indicates that the plasma shape control seems to have a potential for enhancing the conversion efficiency.

Keywords: EUV source, Z-pinch, tapered capillary, high energy density plasma, conversion efficiency, XUV, spectroscopy

I. INTRODUCTION

Development of photolithographic technology for high performance semiconductor devices depends strongly on wavelength of a light source. The extreme-ultraviolet (EUV) light source at around 13.5 nm is expected to be the most promising candidate for the next generation lithography[1]. An effective wavelength region to EUV lithography system is in $\pm 1\%$ bandwidth centered at 13.5 nm, called in-band, due to the reflection characteristic of optics, which is created based on Mo/Si multilayer-coated mirrors. For the requirements such as at extremely short wavelength and within narrow bandwidth, radiation emitted from specific ions in a high energy density plasma generated with a compact device is likely to be the most effective source for semiconductor industry.

Three ionic systems (Xe, Sn, and Li) are of great interest as the efficient EUV emitter because of their potential for holding intense spectra within the effective bandwidth[2–7]. Xe is an inert gas and thus has significant advantages with respect to easy-to-use as a target material, free from macro-particle debris and simple setup in comparison with other two solid-targets at room temperature, which need complicated equipments such as target supply and removal systems.

Thus far, two major technologies for generating a plasma EUV source, gas discharge-pumped-plasma (DPP) and laser-pumped-plasma (LPP), have been widely investigated[2–7]. In DPP, the electrical energy stored in a capacitor bank is directly converted into the energy of emitting plasma. Therefore, DPP has several advantages; high conversion efficiency (CE) from primary electrical energy to EUV, compact design and low cost compared with LPP.

Due to above-described points, we are investigating EUV emitting plasmas based on a Xe capillary discharge. The capillary discharge is probably one of the easiest configurations for generating EUV radiation in DPP. However, source components are inherently close to the hot plasma and are thereby exposed to a large heat load.

Furthermore, typical CE obtained in DPP are relatively low, and this means that an enormous input power, at least over several tens of kilowatts, is required[11]. From these points of view, the most crucial issue for development of EUV sources based on discharge is to meet the required high output power in combination with the long lifetimes of source components[10]. Therefore, to meet these antithetical demands together, plasma conversion efficiency (PCE) defined as ratio of EUV in-band radiation to energy of emitting plasma[11, 12], which is quite low and dominates the total CE, has to be improved. It appears that the reason of low PCE is attributed mainly to short emission duration of Z-pinch based plasmas, which transiently fulfill the condition of plasma such as electron temperature (T_e) and electron density (n_e) suitable for emitting in-band radiation.

To improve the low CE, the radiative plasma has to be maintained as an EUV in-band source much longer[8, 9]. The photon energy of the emitted radiation depends on target material, ionization stage, and electron transition. The ionization stage is basically determined by the plasma parameters, T_e and n_e.

In Xe plasma, the transitions responsible for in-band radiation occur only in ten-times-ionized Xe (Xe XI). For the radiation based on Xe XI, the plasma parameters have to be increased up to appropriate values, for instance $T_e \sim 30 - 40$ eV and $n_e \sim 10^{18} - 10^{19}$ cm^{-3}[11, 13]. For the generation of a long emission EUV source, the radiative plasma must be maintained at appropriate condition in a quasi-steady state. However, plasma parameters in pinching phase are dynamically controlled by the main discharge parameters such as discharge current, initial gas density, and the capillary shape. Then, in Z-discharge, the plasma transiently evolves through the optimum condition for in-band radiation during the pinching process. The plasma-dynamics in radial direction is principally controlled by the self magnetic field in the capillary. Therefore, the capillary shape has a significant potential for controlling and maintaining the high energy density plasma as a radation source at a quasi-steady state.

This paper reports the effects of capillary shape for controlling radiative plasmas based on Xe capillary dis-

charge experiments. A tapered capillary was selected for confining a hot plasma for long time. In this study, the main purpose is to obtain a long emission from the hot plasma with controlling the capillary shape. Therefore, the radiation characteristics observed via tapered capillary discharge were compared with the results of straight one. To understand the Xe hot plasma behaviors, EUV-signals were detected by a photodiode and spectral images were taken by a time-resolved EUV spectrometer.

II. EXPERIMENT

A. Plasma-dynamics in tapered capillary

The capillary design, and pinching process in a conventional straight capillary and a tapered one are shown in Fig.1 and Fig.2. Xe gas is used as the working medium and supplied with supersonic injection through the capillary from up-side to down-side in the figure. In the figure, the solid lines connecting both electrodes indicate current sheets and the objects wedged between the lines are transient plasmas. As shown, at first a pulse generator drives a high-current in Xe gas inside the capillary. After that, a discharge plasma in the capillary is compressed by selfmagnetic field; so-called by pinch effect. In straight capillary, the plasma is pinched on Z-axis, and radiative hot plasma is generated. However, the confinement time of radiative plasma is generally short, because of a momentary expansion.

In contrast, heating process in the tapered capillary is different from that in the conventional straight one. Note that, there exists a gradient of capillary-radius in the gas flow direction. The magnetic pressure of plasma (P_B) at the boundary is expressed simply

$$P_B \propto \frac{I^2}{r^2} \tag{1}$$

where I is the discharge current and r is the plasma-radius. As shown in the above equation, P_B varies along the discharge axis depending on the location with different r inside the tapered capillary. Therefore, pressure difference is induced not only in the radial direction but in the axial direction(Fig.2). Consequently, a hot pinch plasma moves axially in tapered capillary. Due to control of the plasma-dynamics along Z-axis with tapered capillary, the hot plasma can be maintained for long time by the tapered pinch effect and heated by Joule effect. From these effects, we expect to obtain the long EUV emission period.

B. Photodiode measurement

A schematic diagram of the experimental arrangement using photodiodes (IRD company : AXUV20HS1[14]) diagnostics is shown in Fig.3. Two photodiodes are used

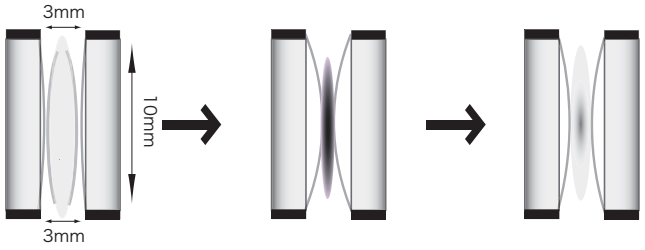

FIG. 1: Pinching-process in straight capillary.

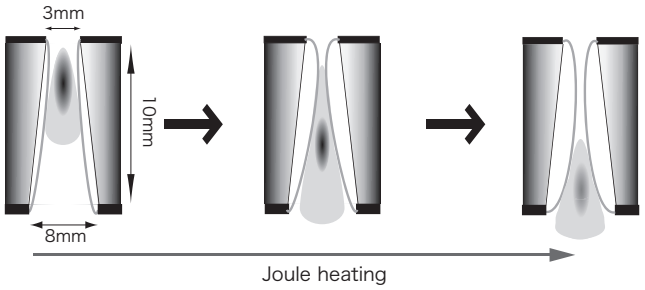

FIG. 2: Pinching-process in tapered capillary.

to measure the emission period and radiation intensity of the pinching plasma. Timing of the discharge can be controlled by delayed trigger signals because Xe gas is supplied with an electrically controlled valve(ECV) for puled flow. A discharge current has an ordinary LCR damped oscillation waveform. The current is controlled by the voltage of a capacitor (0.4μF). The discharge current is measured by a Rogowski coil. As shown in the figure, the phodiode detecting EUV region is located on the capillary axis. This photodiode can measure the time evolustions of EUV-signals from generation to extinction of hot plasma. In addition, visible light from a relatively cool plasma is measured by a photodiode through optical fiber to understand plasma behavior varing from high temperature to low one.

Although it is necessary to use semiconductor switches for highly repetitive discharges in commercial application, discharges are initiated by triggered spark gaps in this series of experiments, because the main purpose of this study is to comfirm the principle; i.e., the effect of plasma shape controlled by capillary geometry. Discharge parameters in this experiment are initial gas pressure at the reserver tank, discharge current and the capillary shape (taper and straight).

C. EUV spectroscopy

In photodiode measurement described above, the photodiode sensitibity in EUV-region has a 4nm bandwidth (FWHM) centered at 13.5nm. For further details of plasma diagnostics, we carried out the EUV spectroscopy

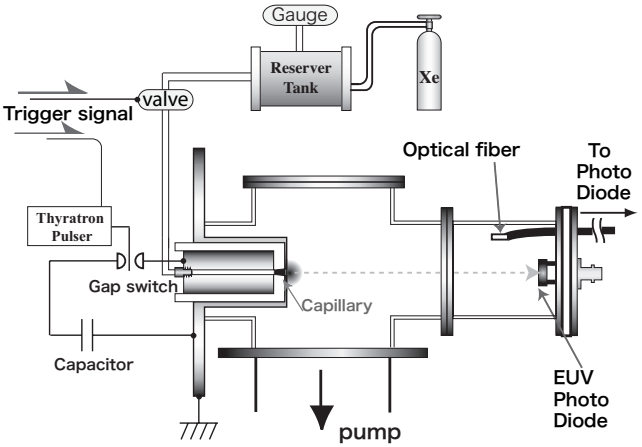

FIG. 3: Schematic of capillary discharge system.

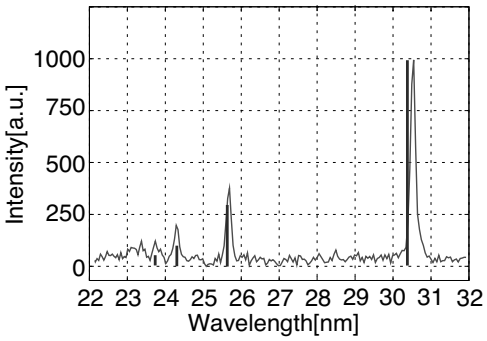

FIG. 5: Comparison of observed spectra with He II lines

using a diffraction grating of flat-field type(HITACHI : No.001-0437) and a micro-channel plate(MCP) (HAMAHATSU : F2223-21P) as a photomultiplier. A schematic diagram of the spectroscopic arrangement is shown in Fig.4. A 1200 l/mm grating was used at a 3° grazing angle of incidence for recording the EUV spectrum in the 10-20nm wavelength range, a pinhole, a slit and the grating are mounted on the capillary axis. This spectrometer can measure the time evolution of spectrum in EUV region and has spacial resolution. Then it can compare the plasma size.

The EUV radiation is measured by a gated MCP with 200ns temporal resolution. EUV light passes a 100μm slit, is deffracted by the grating, imaged on the MCP surface. Finally, visible light from the phosphors attached on the MCP is recorded by a framing camera (HADLAND PHOTONICS : Imacon468).

A 0.8mm pinhole was mounted between the capillary and the slit to obtain spatially resolved plasma size. A vertical length of observed images roughly corresponds to the plasma size in the capillary. Although the spatical resolution is low in this system, relative comparison of plasma size in the capillary of varied shape is possible.

A wavelength calibration was carried out by comparing He II spectrum of He discharge. Fig.5 shows the observed He spectrum (solid line) and expected He II spectrum (bar graph). As shown in Fig.5, the wavalength position and intensity are approximately overlapped. The spectral resolution is determined to be about 0.1nm by FWHM of 30.3nm HeII(Lα) spectrum.

With above-described system, we compared the hot plasma behaviors in the straight capillary with that in the tapered one by measuring the time evolution of spectra in EUV region and the plasma size.

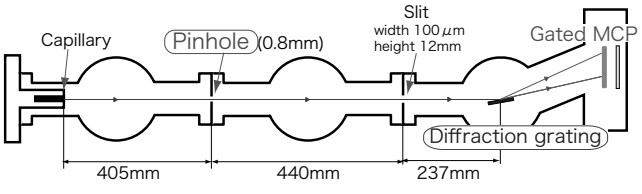

FIG. 4: Top view of spectroscoic system

III. RESULTS AND DISCUSSIONS

In the photodiode measurement, we varied discharge parameters such as capillary shape, initial gas pressure and discharge current. Fig.6 shows the most characteristic results to show capillary shape dependence of photodiode signals, under equal conditions of initial gas pressure and discharge current. In the figure, evolutions of the discharge current, EUV-signals and visible light signals obtained by photodiode are shown. From the comparison of Fig.6(a) and (b), the long EUV-emission period of tapered capillary discharge is confirmed. The integrated EUV-singal of tapered capillary discharge is increased more than that of straight one. This result suggests that the tapered capillary discharge is effective for improvement of the CE. In addition, this also shows that the tapered capillary discharge delays a peak of the visible light signal. From these results, we understand that the plasma condition in the tapered capillary shifts from hot to cool more slowly than that in the straight capillary due to long comfinement of Xe hot plasma.

In spectroscopic measurement, typical time evolution of spectra images obtained by the straight capillary discharge are shown in Fig.7. The horizontal position and the vertical length of observed images correspond to wavelength and the hot plasma size respectively. Some wavelength and MCP position are shown on the images. The time length of caption expresses gating time of the MCP and 0ns corresponds to start of dicharge current. We find that EUV emission from about 11nm to 26nm is maximum at 240-440ns and disappears after that. We also find that in the case of straight capillary, vertical length of the emission distributions is approximately con-

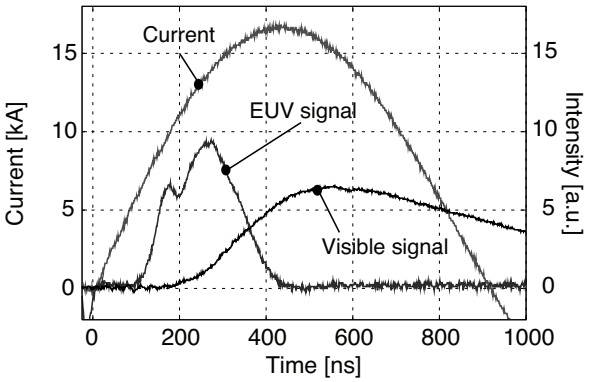

(a) Straight capillary discharge

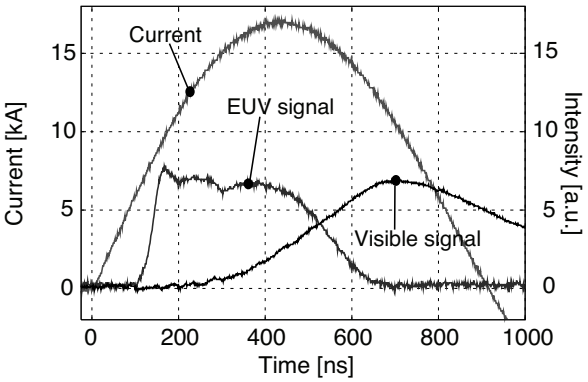

(b) Tapered capillary discharge

FIG. 6: Comparison of EUV and visible radiation using photodiodes

stant during the observation time.

In contrast, the time evolution of spectral image obtained by the tapered capillary discharge are shown in Fig.8. We observed that EUV emission behaviors in tapered capillary is different from that in straight one. In the case of tapered capillary discharge, EUV emission continues beyond 750ns, according with that in photodiode measurement. The spectral images of tapered capillary discharge vertically extend and are different from those of straight one. We can find the time evolution of plasma emitting a certain wavelength because the vertical length of these image corresponds to plasma size. Therefore, behaviors of the Xe hot plasma can be observed, by picking up 13-13.5nm wavelength region in the images. Fig.9 is a comparison of time evolution of plasma behaviors in straight capillary with that in tapered one. Regions indicated by the light quadrangle in the image correspond to 13-13.5nm wavelength. Time length shown in the image expresses exposure period, dot lines correspond to diameter of capillary outlet and right graphs are integrated profile of intensity in the indicated region. From these results, in the case of straight capillary, thin Xe hot plasma is generated in center of the capillary and bacomes intense after that. In contrast, in the tapered capillary, the plasma behavior is more dynamic; the initial emission are generated at three positions. After that, the plasma emission converges at the center of the capillary. Consequently, we can understand that capillary shape has a possible way for control of hot plasma behaviors.

Fig.10 shows time-integrated spectra with the tapered capillary during 750-950ns. At this period, a number of spectra were observed by tapered capillary discharge. Although in the capillary discharge, EUV spectra extends in a broad region not only from hot Xe plasma but also ablated material, we can see only Xe hot plasma behaviors by focusing attention on the spectral image at 13.5nm region from Xe XI (4d-5p). As shown in Fig.10, at 750-950ns 13.5nm emission from Xe hot plasma was comfirmed in the tapered capillary discharge, in contrast to the fact that 13.5nm region was not observed in the case of straight one.

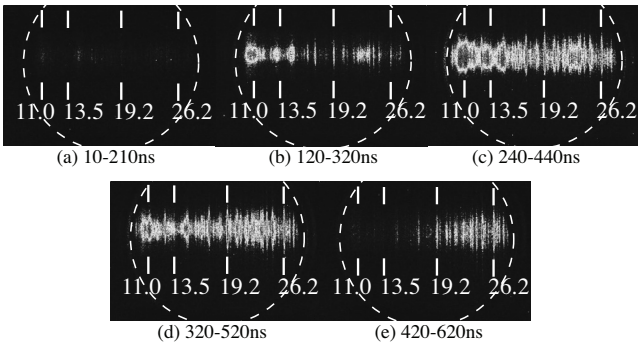

FIG. 7: Evolution of spectral images of discharge plasma in straight capillary

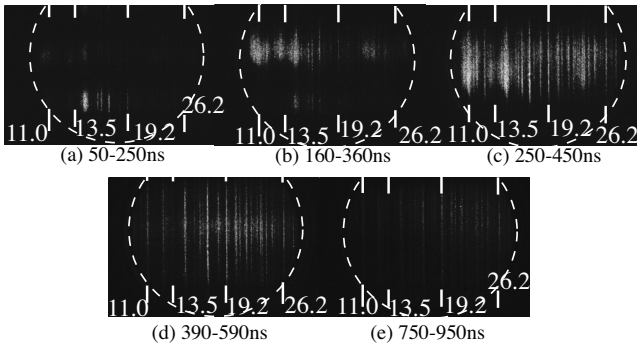

FIG. 8: Evolution of spectral images of discharge plasma in tapered capillary

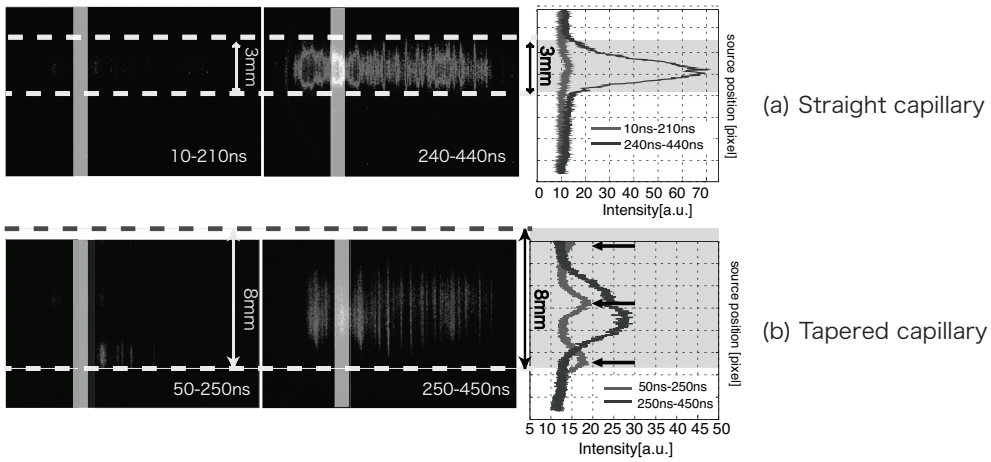

FIG. 9: Time evolution of plasma behaviors

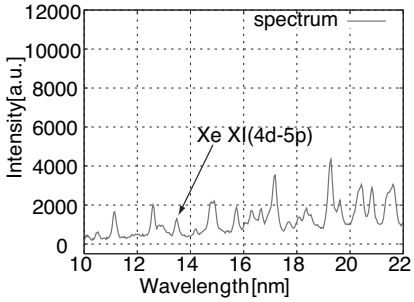

FIG. 10: Observed spectrum with tapered capillary during 750-950ns

IV. SUMMARY

We have investigated the effects of capillary shape on EUV emission for controlling radiative plasmas. In photodiode measurement, increase of period and enhaced integrated EUV radiation were observed with tapered capillary. By EUV spectroscopy, long 13.5nm emission and different plasma behaviors in the tapered capillary discharge were also confirmed. The experimental results indicate that Xe plasma maintained hot condition for longer period by the tapered capillary and the condition clearly depends on the capillary shape. From the results reported here, plasma shape control has a significant potential for enhancing the plasma conversion efficiency of the discharge-pumped EUV source. Although we understood that the tapered capillary is effective for development of EUV source, optimizations of capillary shape were not subsequently implemented. We are planing to optimize the profile of plasma shape for efficient EUV plasma.

Acknowledgments

This work was partly supported by NEDO (New Energy and Industrial Technology Development Organization) and EUVA (Extreme Ultraviolet Lithography System Development Association).

[1] D. Attwood, *SOFT X-RAYS AND EXTREME ULTRAVIOLET RADIATION: Principles and Applications* (Cambridge, New York, 1999)

[2] M. A. Klosner and W. T. Silfvast, Opt. Lett. **23**, 1609 (1998)

[3] E. R. Kieft, J. J. A. M. van der Mullen, G. M. W. Kroesen and V. Banine, Phys. Rev. E **68**, 056403 (2003)

[4] U. Stamm, J. Phys. D **37**, 3244 (2004)

[5] E. R. Kieft, J. J. A. M. van der Mullen, G. M. W. Kroesen, V. Banine and K. N. Koshelev, Phys. Rev. E **71**, 026409 (2005)

[6] M. A. Klosner and W. T. Silfvast, Appl. Opt. **39**, 3678 (2000)

[7] M. A. Klosner, H. A. Bender, W. T. Silfvast and J. J. Rocca, Opt. Lett. **22**, 34 (1997)

[8] M. Masnavi, M. Nakajima, A.Sasaki, E.Hotta, K. Horioka, Appl. Phys. Lett. **89**, 031503(2006)

[9] M. Masnavi, M. Nakajima, A.Sasaki, E.Hotta, K. Horioka, Appl. Phys. Lett. **87**, 111502(2005)

[10] A.Kikuchi, T.Takahashi, M.Masnavi, M.Nakajima, T.Kawamura, M.Shiho, E.Hotta and K.Horioka, NIFS-PROC-**64**, pp.1-5,(2006)

[11] T. Krüchken, K. Bargmann, L. Juschkin and R. Lebert, J. Phys. D **37**, 3213 (2004)

[12] M. Masnavi, M. Nakajima, E.Hotta, K. Horioka, G.Niimi and A.Sasaki, J.Appl. Phys. vol.101, No.3, 033306(2007)

[13] Rainer Lebert, Klaus Bergmann, Larissa Juschkin, Oliver Posier , Willi Neff, AIXUV GmbH, Fraunhofer Institut Fur Lasrtechnik, Proc.SPIE 4343

[14] http://www.ird-inc.com/

EXPERIMENTAL STUDY OF Z-PINCH XENON PLASMA DYNAMICS FOR EXTREME ULTRAVIOLET SOURCE

S. Katsuki, N. Tomimaru, H. Imamura, T. Namihira, T. Sakugawa, H. Akiyama,

Department of Electrical and Computer Engineering, Kumamoto University
Kurokami 2-39-1, Kumamoto City, Kumamoto 860-8555, Japan

ABSTRACT

This paper describes the characteristic of EUV emission from the pulsed power driven Z-pinch xenon plasmas and the EUV emission volume associated with the plasma dynamics. A high speed visible camera placed in the direction of the angle of 30 degrees to the Z axis was employed to observe the three dimensional dynamics of the plasma. The experiment shows that the plasma is dynamic not only in the radial direction but also in the axial direction, suggesting that the axial plasma dynamics influences the EUV emissive volume.

Keywords : EUV source, Z-pinch, plasma dynamics, spectrum, high speed imaging, emissive volume

1. INTRODUCTION

Z-pinch discharge plasmas are presently the most powerful extreme ultraviolet (EUV, 13.5 nm, 2% bandwidth) source for the 32 nm or less rule photolithography process. The in-band EUV power required for the practical lithography tool is 115 W on the basis of the photoresist sensitivity of 5 mJ/cm^2 and the process throughput of a hundred 12-inch wafers per hour. Figure 1 shows the recent progress and the future target of the development of the EUV sources based on gas discharge produced plasmas (GDPP) [1,2,3,4]. The major developers of GDPP EUV source including Xtreme technologies, Philips Extreme UV, Cymer, Plex LLC and EUVA have competitively progressed in their devices in past 6 years and some of them have achieved the huge power in the range of 50 W so far. Their progress with respect to output EUV power has been brought about by the high repetition rate operation and the tin target technologies [2,3,4]. However, the break-through technologies are indispensable to obtain 115 W EUV power under its long term and high rep-rate operation.

Figure 2 shows the typical configuration of GDPP EUV source. The plasma emits the various kinds of debris including high energy ions and neutrals in addition to dust delivered both from the electrodes and insulator wall. The debri shield eliminates the dust but not high energy particles. A collector mirror collects and directs the EUV power to the intermediate focus point (IF), which is the gate to the main room for lithography optics. One of the main difficulties in the development of the high volume manufacturing (HVM) device is the shortage of the component lifetime, which is attributed to the thermal load to the discharge components. Electrical

power into the discharge is estimated to be 100 kW based on the practical assumptions that the conversion efficiency from electrical to EUV (CE) is 2%, the collection efficiency at the source is 25% and the transmission efficiency from the source to the IF is 20 %. This huge power dissipation in the chamber shortens the lifetime of the components including electrodes, insulator wall as well as the condenser mirror. Therefore, it is quite important to improve the CE and the collection efficiency and to use the recoverable electrode system.

A pulsed power driven Z-pinch device for EUV light source has been developed at Kumamoto University to find key technologies to increase the CE and to minimize the emission volume. In this study, we used xenon gas as a EUV emitter though it is low emission efficiency in 13.5 nm. This paper describes the characteristic of the EUV emission from the pulsed power driven Z-pinch plasmas and the plasma dynamics from the viewpoint of the emissive volume.

2. EXPERIMENTAL SETUP

2.1 Z-pinch discharge head

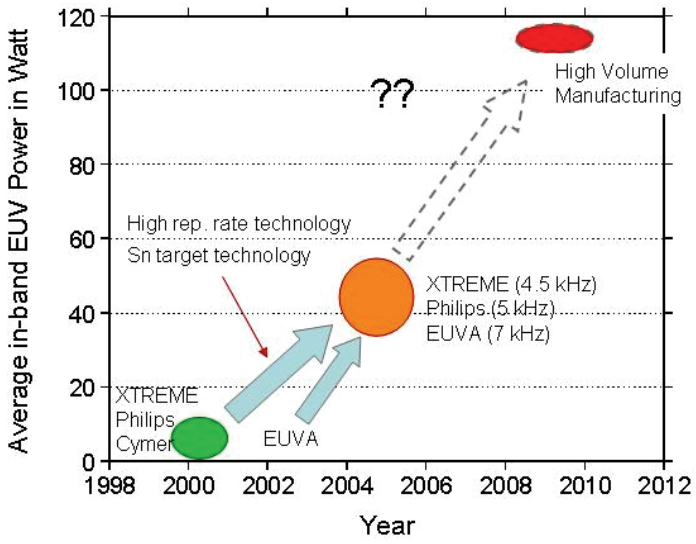

Figure 1. Effect of an external magnetic field on the pinch process of Z-pinch system.

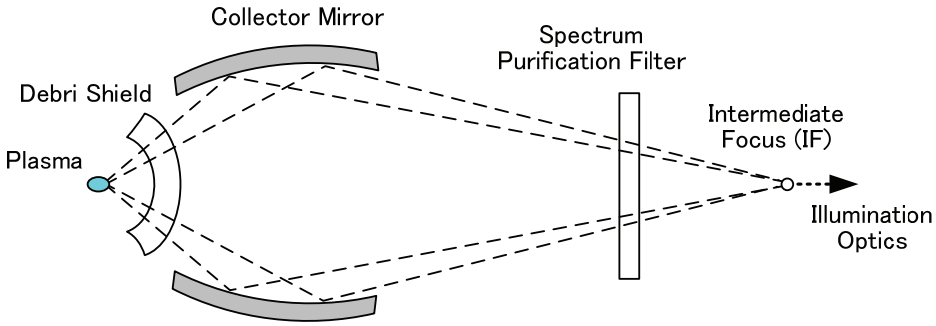

Figure 2. Typical configuration of EUV source based on gas discharge produced plasma.

Figure 3 shows the Z-pinch discharge head, which consists of a 42 nF capacitor bank, a toroidal ferromagnetic core, and a z-pinch chamber. They are sandwiched with two circular aluminum plates, one is directly bolted on the vacuum chamber evacuated to 10^{-3} torr, the other is provided with negative high voltages. The z-pinch discharge chamber, which consists of a hollow copper-tungsten alloy cathode, a stainless steel ring anode and a rounded alumina ceramic tube with the minimum diameter of 5 mm and the length of 5 mm, is located in the center of the coaxial structure. A flow rate of xenon gas fed into the discharge chamber is fixed to be 50 cc/min. FINEMET^{TM} FT-1H (Hitachi Metals) was chosen as the material for the ferromagnetic core as a high speed switch, which enables the repetitive operation. The 42 nF capacitor bank is rapidly charged up to the voltage of 27 kV by a magnetic pulse compressor

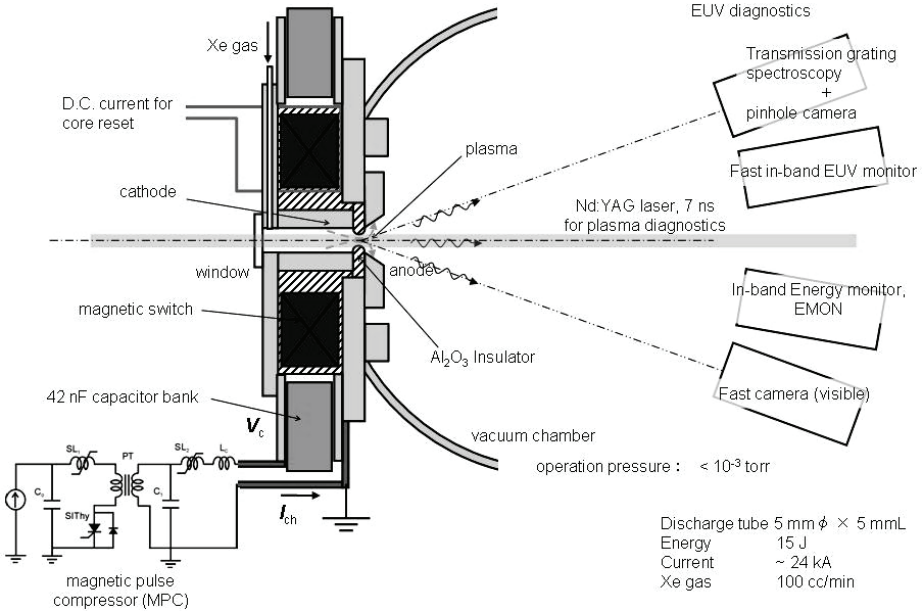

Figure 3 Overview of the experimental setup including the discharge head, magnetic pulse compressor and diagnostics.

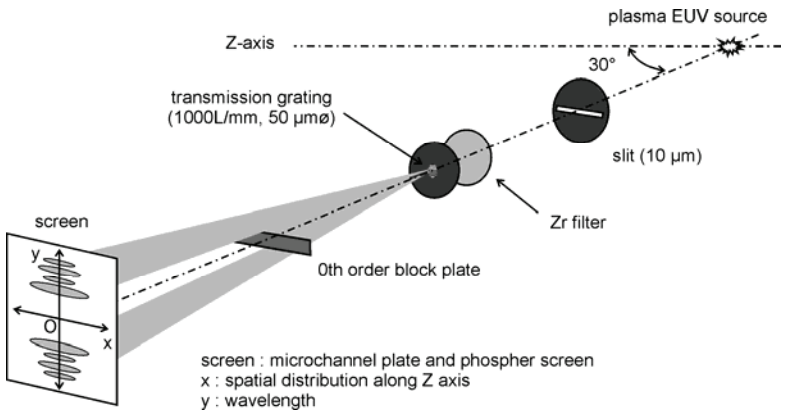

Figure 4 Spatially resolved EUV spectrometer using a transmission grating. .

(MPC). This circuit delivers the current with amplitude of 34 kA and pulse duration of 110 ns to a short circuit load.

2.2 Diagnostics

The in-band EUV emission is monitored using a fast silicon photodiode (IRD, AXUV5) filtered by two silicon/molybdenum multilayer mirrors and a 150 nm thick zirconium window. A transmission diffraction grating spectrometer (TGS) as shown in Fig. 4 was used to observe EUV emission spectra of Z-pinch plasmas. Since a grating lattice (1000 lines/mm) is fixed on a 50 μm diameter pinhole, the spectrometer works also as a one dimensional pinhole camera in the perpendicular direction of the diffraction, which corresponds to the Z axis of the discharge. Wavelength and spatial resolutions of the spectrograph are 0.3 nm and 100 μm, respectively. The 1st order diffraction light is visualized by a double layer micro channel plate (MCP) with a phosphor screen. Obtained spectra are calibrated by several sharp line spectra of oxygen ions in the CO_2 discharges. A visible high speed camera placed in the direction of angle of 30 degree to the Z-axis enables us to take a three dimensional time-resolved image of the plasma dynamics. The voltage of the capacitor and the plasma current were measured with a voltage divider (EP100K Pulse Electronic Engineering) and a calibrated pick-up coil, respectively.

3. EUV EMISSION FROM THE PLASMAS

Figure 5 shows the waveforms of the plasma current and the in-band EUV emission. The peak current is suppressed owing to the increase in the plasma impedance, which indicates the energy conversion to the kinetic energy of the plasma. The conversion efficiency from the electrical to the plasma is approximately 30% in this case. The EUV emission starts increasing gradually at the current peak, and become the maximum intensity at the decay phase of the current. The current drops quickly after the EUV emission peak, which indicates the occurrence of the maximum implosion. The emission ends together with the plasma current.

Figure 6 shows the spatially resolved spectrum of the Z-pinch xenon plasmas. Strong emissions near 11 nm associated with the 4d-5p transition of adjacent ion stages (Xe^{7+}-Xe^{12+}). 12.5, 13.5 and 14.9 nm are associated with 4d-4f transitions of Xe^{11+},

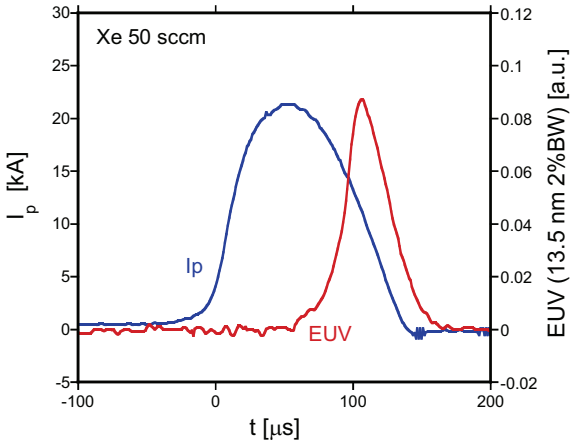

Figure 5 Waveforms of plasma current and in-band EUV emission for the xenon flow rate of 50 cc per minute.

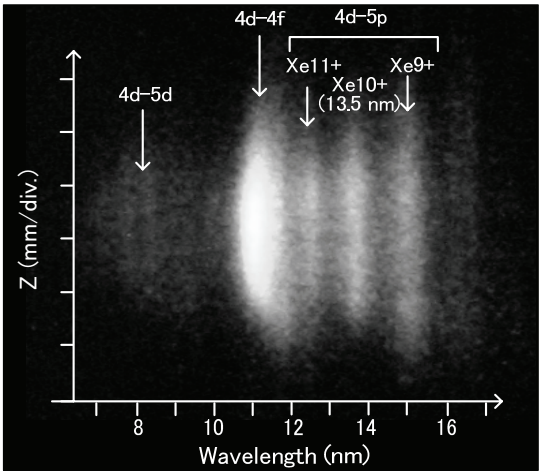

Figure 6. Spatially resolved EUV spectrum of Z-pinch xenon plasma for the flow rate of 50 cc/min.

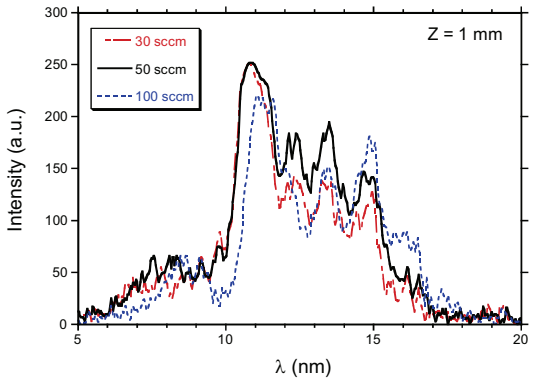

Figure 7. EUV spectra of Z-pinch xenon plasma for the flow rate of 30, 50 and 100 cc/min.

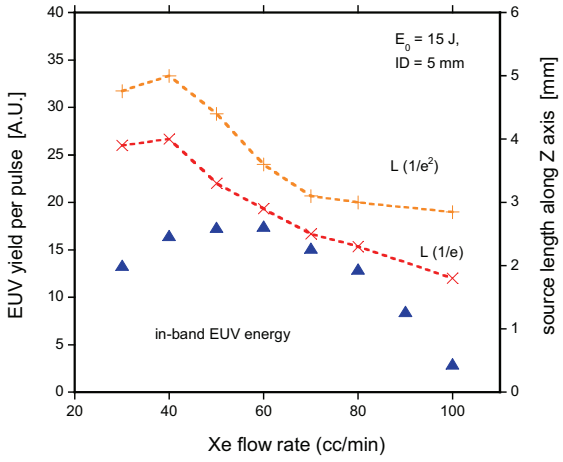

Figure 8. Radial profile of electron density when the strong pinch occurs (t = 80 ns)..

Xe^{10+} and Xe^{9+} ions, respectively. Usually the 11 nm mission is strong for xenon plasmas, while the 13.5 nm emission is only a small fraction. The emissive region of 13.5 nm, which determines the source size, is distributed in approximately 4 mm along the Z-axis. Figure 7 shows the EUV spectrum obtained form Fig. 6, together with those of different xenon flow rate of 30 and 100 cc/min. The larger flow rate tends to strengthen the line emissions of longer wavelength, indicating the lower temperature [5]. The emission of 13.5 nm is most intense in the case of the flow rate of 50 cc/min. Figure 8 shows the in-band EUV yield per shot and the length of the emissive region along the Z-axis as a function of the xenon gas flow rare. Though the flow rate of 50 cc/min is the best with respect to the EUV yield, the emissive region is not sufficiently small. At the lower flow rate, which is supposed to be low pressure, the emissive region tends to be enlarged in the Z direction. In order to investigate what determines the size of emissive region, we observe the plasma dynamics using a high speed camera.

4. DYNAMICS OF Z-PINCH PLASMAS

A high-speed single frame camera with the exposure time of 1.5 ns was used to observe temporal behavior of the plasma. Since the camera is placed in the direction of the angle of 30 degree to the Z axis, the axial plasma dynamics in addition to the radial direction can be observed. Figure 9 shows the still photograph of the pinched plasma, showing the 10 mm long filamentary plasma. Figure 10 shows the plasma dynamics based on the time-resolved photographs of the plasma at different times from the beginning of the current. Each photograph was obtained in different shot. This indicates that the plasma is dynamic not only in the radial direction but also in the axial direction. An annular plasma was initially formed near the insulator wall, and then the plasma moves toward the center. The first compression occurred at approximately t = 100 ns and the plasma stagnates at the center for tens of ns. The plasma length along the Z axis is 1.5 mm at 100 ns that is much smaller than the filamentary plasma as shown in Fig.9. After the first compression, the plasma splits into two parts. One moves forward and the other moves backward. According to Fig. 5, the EUV emission lasts until t = 150 ns. This fact indicates the moving plasmas still emit EUV photons.

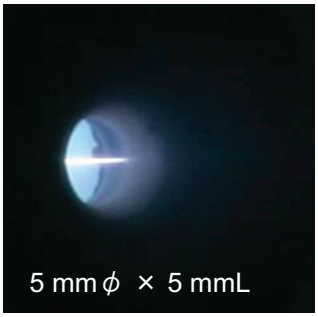

Figure 9. Still photograph of the Z-pinch plasma. Viewing angle is 30°.

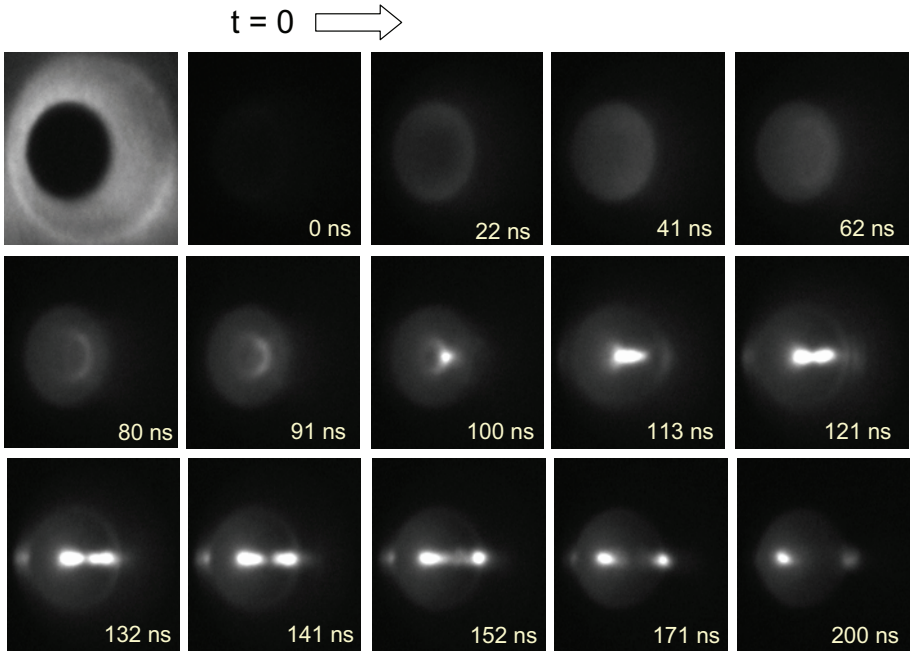

Figure 10. Temporal development of the visible emission of the plasma, consisting of time-resolved photographs at different time after the current start flowing. Viewing angle is 30°.

This dynamics especially in the axial direction enlarges the emissive region in the time integrated view. The axial plasma dynamics needs to be suppressed to reduce the EUV source size

5. SUMMARY

We have characterized the EUV emission from the pulsed power driven Z-pinch plasmas and discuss the mechanism to determine the EUV emissive volume based on the plasma dynamics. The EUV yield, emission spectrum and the emissive volume depend on the xenon gas flow rate. Especially, the emissive volume is indicated to be influenced by the plasma dynamics along the Z-axis.

6. ACKNOWLEDGEMENTS

This project is supported by NEDO, EUVA and the 21 Century COE Program on “Pulsed Power Science” selected by MEXT.

7. REFERENCES

[1] R. Lebert et al., Emerging Lithographic Technologies V, Proc. SPIE 4343, 215 (2001).

[2] J. Pankert, “Philips’s EUV Source:Update and Issues,” 3rd EUVL Symposium, Miyazaki, November 1-4, 2004, unpublished.

[3] J. Ringling, “Development Status of High Power Tin Gas Discharge Produced Plasma Sources For Next Generation EUV Lithography,” 3rd EUVL Symposium, Miyazaki, November 1-4, 2004, unpublished.

[4] Y. Teramoto, et al, “High power capillary EUV source development,” 3rd EUVL Symposium, Miyazaki, November 1-4, 2004, unpublished.

[5] N. Bouering, M. Martins, W.N. Prtlo, I.V. Fomonkov, “Extreme ultraviolet emission spectra of highly ionized xenon and their comparison with model calculations,” J. Appl. Phys. Vol. 95, No. 1, pp.16-23 (2004)

FORMATION OF X-RAY POINT SOURCE IN THE GAS-PUFF PLASMA FOCUS EXPERIMENT

Keiichi Takasugi and Ena Kiuchi[+]

Institute of Quantum Science, Nihon University, Tokyo 101-8308, Japan

[+] *College of Science and Technology, Nihon University, Tokyo 101-8308, Japan*

ABSTRACT

The experiment on a new type of plasma focus with divergent gas-puff was conducted for the realization of the point radiation source with high efficiency. The input energy increased by about 40 % with the divergent gas-puff, and the hot spots were concentrated on the vicinity of the anode. -ray radiation of energy 150 - 200 keV that far exceeded the power-supply voltage was observed. It is thought that the particle acceleration occurred.

1 Introduction

The energy transfer to gas-puff z-pinch is efficient [1, 2], and high temperature and high density plasma is achieved easily in this system. So it has been used as a soft x-ray and EUV light source. The produced high temperature plasma points (hot spots) are distributed on the center axis between the electrodes.

On the other hand, the plasma is converged to a single point in plasma focus, and the point radiation source is formed. As the plasma after the conversion flows axially, dispersing to surroundings like z-pinch is little. However, past plasma focus has a disadvantage not to obtain a strong pinch easily. Because the device is filled with operating gas and initiated with surface discharge of the insulator, the energy input is limited by the insulating material [3].

The essence of the plasma focus is that the structure of electrodes is coaxial, not in plane symmetry. So the produced plasma is not axially uniform. The experiment on the plasma focus with divergent gas-puff was started to realize the point radiation source with good efficiency with the advantage of both devices. It was understood in the process of experiment that not only the soft x-ray but also high energy x-ray were radiated from the plasma. In this research, the energy, the intensity and the source of the x-ray were examined in the new type of plasma focus.

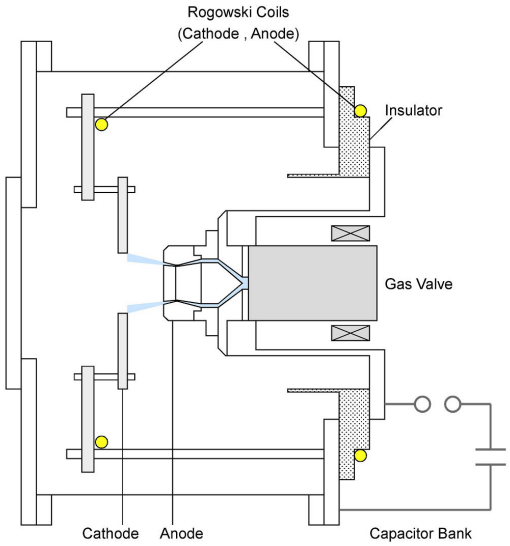

Fig. 1: Schematic diagram of the SHOTGUN z-pinch device with a divergent gas nozzle.

2 Experimental Setup

The experiment was conducted on the SHOTGUN z-pinch device at Nihon University (Fig. 1). The energy storage section of the device consists of 30 kV 24 μF capacitor bank, and the maximum discharge current is 300 kA. The charged voltage of the bank was 25 kV (7.5 k) in this experiment.

The isolated gas distribution can be formed between the electrodes with a high-speed gas valve and an annular Laval nozzle mounted on the anode [4]. Figure 2 shows the arrangements of electrodes in the usual z-pinch and the divergent gas-puff experiment. The gas was ejected

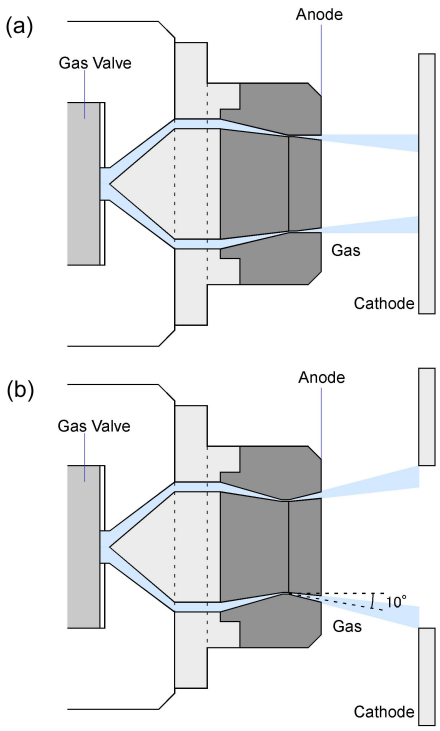

Fig. 2: (a) Straight gas nozzle for the usual z-pinch and (b) 10° radially divergent gas nozzle.

straight in the usual z-pinch, and a uniform gas distribution is formed between the electrodes. A flat cathode with many small holes was used to form a symmetric electrode arrangement. In the divergent gas-puff experiment a gas nozzle with the ejection angle of 10° outward was used, and the radially divergent gas distribution was formed from the anode to the cathode. In order to form asymmetric plasma, a big hole was opened to the cathode. The distance between the electrodes was 3 cm. Ar gas was used in this experiment, and the plenum pressure of the gas valve was 5 atm.

Total discharge current was measured by the anode Rogowski coil located outside the chamber, and the current in the cathode plate was measured by the cathode Rogowski coil. Soft x-ray was detected by x-ray diodes (RDs) with Au, Ni and Al photocathodes. The RDs are more sensitive to high energy photons in this order. -ray signal was detected by a scintillation probe (SCI) with a 10 μm Be filter. An x-ray pinhole camera was used for taking x-ray image of the pinch plasma. A 10 μm Be filter was installed in the pinhole camera to prevent visible and ultraviolet lights. Moreover, in order to detect high energy x-ray around the device, an x-ray film cassette was prepared. Kodak BioMax MS film was used for recording soft x-rays, and Fuji GRENE G-8 intensifying screen was attached on the film specially for recording hard x-rays. A survey meter of ionization chamber type was used for the measurement of dose of x-ray radiation.

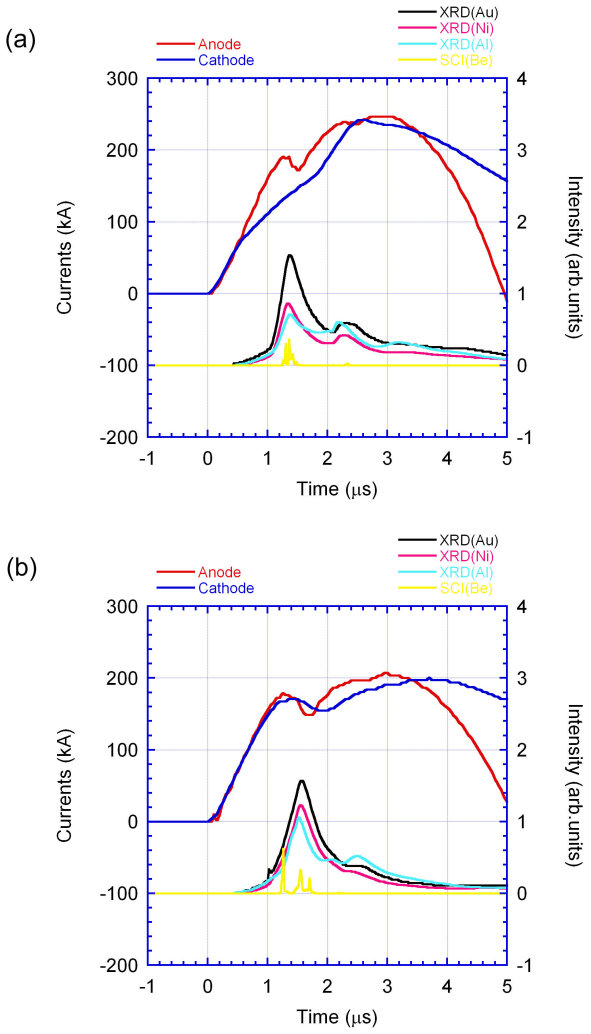

Fig. 3: Discharge currents, RD signals and SCI signal of (a) the usual z-pinch and (b) the divergent gas-puff experiment.

3 Experimental Results

Discharge currents, RD and SCI signals of the usual gas-puff z-pinch and the divergent gas-puff experiment are shown in Fig. 3. The discharge currents just before the pinch for both discharges are about 200 kA. Both currents begin to decrease at the time 1.2 μs and form dips. This means that the circuit inductance increases for a moment with the shrinkage of the plasma. The current dip of the divergent

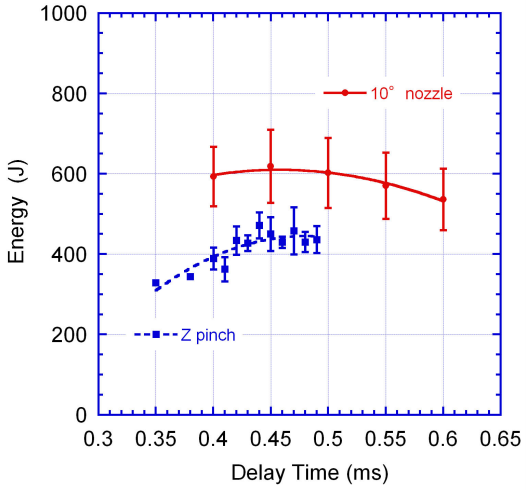

Fig. 4: Input energies to the plasmas as a function of the delay time comparing the divergent gas-puff experiment with the usual z-pinch.

gas-puff experiment is deeper than that observed in the usual z-pinch. The observation shows that the input energy of the divergent gas-puff experiment is larger than that of the usual z-pinch. Three RD signals increase at the current dip, indicating the increment of plasma temperature. -ray emission is seen pulsing in the divergent gas-puff experiment.

Figure 4 compares the input energies to the usual z-pinch and the divergent gas-puff experiment. The energies were obtained by the analysis of current waveforms [2]. Horizontal axis is the delay time of discharge from the gas-puff, which corresponds to the amount of gas at the discharge. The energy is 550 - 600 in the divergent gas-puff experiment, while it is 350 - 450 in the usual z-pinch.

The soft x-ray image of the plasma was observed by an x-ray pinhole camera. All the photographs were exposed over 10 shots. Figure 5(a) shows the photograph of the usual gas-puff z-pinch plasma. The hot spots line up on the center axis between the electrodes. In order to examine the effect of the asymmetry of the electrode, the z-pinch discharge with the cathode with big hole was performed (Fig. 5(b)). The hot spots line up similar to the usual z-pinch, and it was understood that the gas distribution accomplishes the key role to the pinch formation. Figure 5(c) shows the photograph of the divergent gas-puff experiment, in which the hot spots were concentrated on the vicinity of the anode as expected. Soft x-ray radiation around 4 Å emitted from Ar ion has been

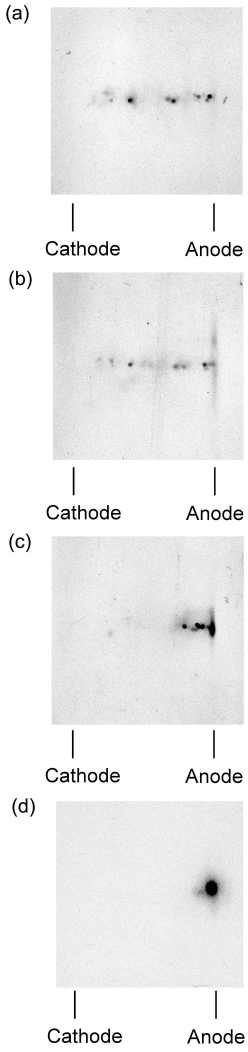

Fig. 5: -ray pinhole photograph of the plasma exposed over 10 shots. (a) usual z-pinch, (b) z-pinch with the cathode with big hole, (c) divergent gas-puff experiment and (d) hard x-ray photograph of the divergent gas-puff experiment.

observed in the usual z-pinch [5], but x-ray exceeding 10 keV has not been observed [2]. As it had been understood in the process of the experiment that high energy x-ray was radiated from the device, the obserbation for specifying the radiation source was performed. The x-ray film was covered by a 0.5 mm Cu plate to prevent soft x-ray, and the intensifying screen was attached to improve sensitivity (Fig. 5(d)). As a result, the radiation of hard x-ray was observed from the center of the anode surface.

Figure 6 shows an x-ray radiograph taken by the film cassette located 60 cm axially away from the device center. The film was exposed over 20 shots to take the picture. Evidently

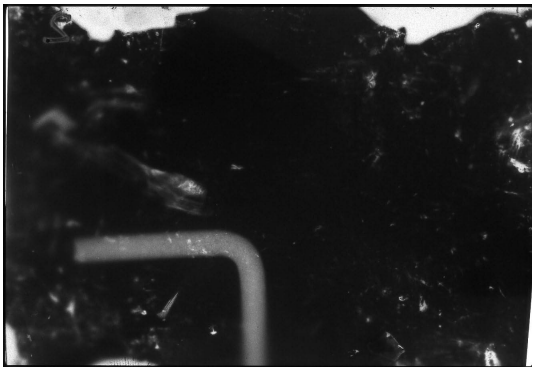

Fig. 6: -ray radiograph located axially away from the device center. The x-ray penetrates a 4 mm hex-head steel wrench.

hard x-ray is radiated from the z-pinch device. It has been understood for the x-ray to pass both a 2 cm aluminum flange and a 0.2 mm stainless steel shading plate, because the film was pitch-blackness. The top white part in the film is a part where intensifying screen is lacked. The x-ray penetrates 50 % in the part of the shadow, when a hex-head steel wrench of 4 mm corner was put on the cassette. The energy of the x-ray is estimated to 150 - 200 keV from the transmission of materials. The lead plate of 1 mm thickness is necessary to protect from the x-ray. Dose of x-rays was about 1 μSv on the shot average according to the surveymeter placed at the same position.

4 Summary and Discussion

In summarizing the new type of plasma focus experiment was conducted with 10° divergent gas-puff. The hot spots concentrated in front of the anode in the divergent gas-puff experiment, while the hot spots lined up on the center axis between the electrodes in the usual z-pinch. It has been understood that the cause of the concentration of hot spots depends on not the asymmetry of the electrode arrangement but the asymmetry of the gas distribution. The input energy of about 40% has increased with the divergent gas-puff compared with a usual z-pinch.

It was understood that hard x-ray with the energy of 150 - 200 keV was emitted in the divergent gas-puff experiment, while such x-ray has not been observed in the usual z-pinch. The dose of x-rays at the position 60 cm away from the device was about 1 μSv for each shot.

-ray was radiated from the center of the anode surface, and the point radiation source was formed.

The observation of high energy x-ray may be owing to high energy electrons hitting on the anode. The generation of high energy particles that far exceeded the power-supply voltage has been reported in conventional plasma focus device [6], and the observation is thought to be the appearance of the similar phenomenon.

References

[1] . Shiloh, A. Fisher and N. Rostoker, Phys. Rev. Lett. **40**, 515 (1978).

[2] K. Takasugi, H. Suzuki, K. Moriyama and T. Miyamoto, pn. . Appl. Phys. **35**, 4051 (1996).

[3] W. Kies, Plasma Phys. Cont. Fusion **28**, 1645 (1986).

[4] K. Takasugi, A. Takeuchi, H. Takada and T. Miyamoto, pn. . Appl. Phys. **31**, 1874 (1992).

[5] P. G. Burkhalter, . Shiloh, A. Fisher and R. D. Cowan, . Appl. Phys. **50**, 4532 (1979).

[6] T. Yamamoto, K. Shimoda,K. Kobayashi and K. Hirano, pn. . Appl. Phys. **23**, 242 (1984).

DEVELOPEMENT OF HIGH REPETITION RATE MARX GENERATOR

K. Igawa, H. Ontachi, I. Kitamura, H. Ito and K. Masugata
Faculty of Engineering, University of Toyama
3190 Gofuku, Toyama, 930-8555, Japan

Abstract

This paper reports the development and evaluation of a repetitively pulsed high-voltage generator that consists of a Marx generator with a new configuration and a pulse forming line for achieving high repetition rate operation. The generator consists of basically an inductor for current limiter, a transformer with winding ratio 1:500, a rectifier(diode), and 3-stage Marx generator using inductors instead of charging resistors. Experimental results show that the developed Marx generator can operate with repetition rate of around 0.7 Hz. As a result, it is possible to make simple and low-cost repetitively pulsed power generator with high voltage($\geq$ 100 kV) and high energy($\sim$ kJ).

1 Introduction

In the last decade, high-voltage pulsed power generators have been extensively developed for various applications such as intense pulsed charged particle beam, discharge light source(EUV source), gas laser, pulsed ozonizer and exhaust gases cleaning. The critical issue to be overcome for those industrial applications is the capacity of repetitive pulsed power techniques. Gap switches and thyratrons have been widely used as the switch of the pulsed power generator. Recently, semiconductor power device technology has improved the performance of fast high power switching devices. Therefore, the high repetition rate, long life time, and high reliability pulsed power generators have been developed using semiconductor switches such as static induction thyristors[1,2]. However, the semiconductor switch is still not sufficient to develop short pulse (100 ns or less) high voltage (of order of 100 kV) generators. In addition, in most of the pulsed power generator using semiconductor switches it is necessary to be connected in parallel and in series in order to handle high voltage and large current, since the rated voltage of thyristor is limite to several kVs per device. In this case, care must be taken that voltage and current is equally divided to each device. Hence, the semiconductor switch is used in practical systems with the assistance of a magnetic switch and a gate driving technique. The practical generators consist of semiconductor switches, step-up pulse transformers and magnetic switches. This also makes the system costly and complicated.

Marx generators have been used to drive the intense pulsed charged particle beam, since it is easy for them to produce the high-voltage pulse with pulse duration of order of 100 ns. The generator is also a simpler design and lower cost than that using semiconductor switches. However, the charging time is determined by the capacitor and charging resistor, since the conventional Marx generator is charged through the charging resistors. If a constant voltage is used as the charging source, the energy dissipated in the charging resistors is equal to the stored energy in the capacitors. Therefore, Marx generators are not suitable for high repetition rate operation.

We propose a new circuit configuration of Marx generator to develop the high repetition rate pulsed power generator. The generator consists of the Marx generator and a pulse forming line. The following some modifications to the conventional Marx generator were made for high repetition rate operation. The charging resistors were replaced by inductors in order to achieve the fast

energy store and to eliminate the energy loss in the resistors. In addition, an inductor for current limiter was used to control the charging current. In this paper, we present the development and evaluation of the high repetition rate Marx generator.

2 Design of the System

The repetitively pulsed power generator was developed to operate the ion diode at a repetition rate of 1 Hz. The main components of the pulsed power generator are an input source, a Marx generator and a pulse forming line(PFL). A block diagram of pulse power system is illustrated in Fig.1.

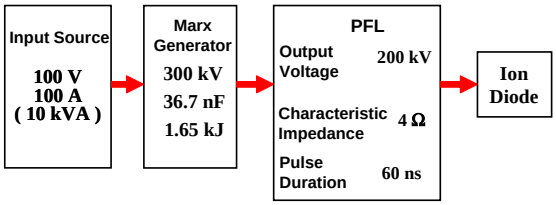

Fig.1 Block diagram of pulse power system.

The PFL consists of a single coaxial transmission line and is filled with the deionized water as a dielectric. The capacitance and inductance of the PFL are 7.4 nF and 122 nH, respectively. The designed characteristic impedance Z and the electrical length T_0 of the PFL are 4 Ω and 60 ns, respectively. The PFL is charged positively by the developed high repetition rate Marx generator with the output voltage 300 kV and the stored energy 1.65 kJ at a charging voltage of 50 kV. The output of the designed PFL is the positive pulse of voltage 200 kV with pulse duration of 60 ns.

Figure 2 shows a circuit diagram of the high repetition rate Marx generator. The generator consists of basically an inductor for current limiter, a transformer with winding ratio 1:500, a rectifier(diode), and 3-stage Marx generator using inductors instead of charging resistors. The Marx generator is charged to the charging voltage of 50 kV through the transformer. The trigatron spark gap switch and the field distortion spark gap switch were used as the switch of the Marx generator. The capacitor of Marx generator is resonantly charged by replacing the charging resistors with the inductors of 0.67 mH. This enables us to reduce the charging time and, consequently, to operate the Marx generator in the repetitive mode. For overcurrent protection of the circuit elements including the transformer and the rectifier, the inductor(L_1) of 5 mH for the current limiter is connected in series with the low voltage side of the transformer.

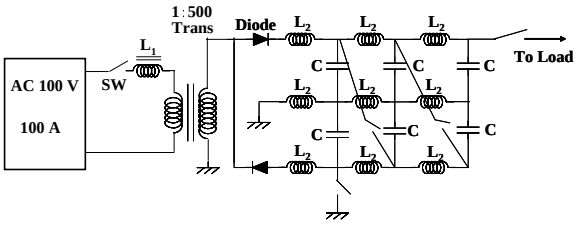

Fig.2 Circuit diagram of repetitive Marx generator.

Next, let us explain the sequence of operation of the high repetition rate Marx generator. Figure 3 illustrates the rough waveform of the charging voltage. The capacitors of the Marx generator is charged up to the setting value after the input power turns on((1) in Fig.3). When the charging voltage reaches the setting voltage, the input power is switched off and, subsequently, the Marx generator is discharged by applying the trigger pulse to the switch((2), (3) in Fig.3). After discharging is finished, charging of the Marx generator is started again((4) in Fig.3).

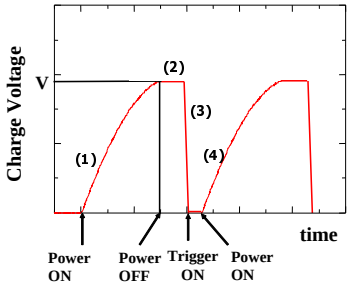

Fig.3 Sequence of operation of repetitive Marx generator.

3 Experimental Results

Figure 4 shows typical waveforms of the input voltage (V_{in}), input voltage of transformer (V_{Tr}) and current of transformer (I) during the charging process. In the initial stage of the charging

process(Fig.4(a)), the phase difference between $V_{\rm in}$ and I is caused by the influence of the inductor(L_1) and is around $\pi/2$. On the other hand, $V_{\rm in}$ and I are in phase at the end of the charging process as seen in Fig.4(b). It is evident from Fig.4 that the current is lower than the rated current 100 A of the transformer and that the inductor L_1 functions as the current limiter.

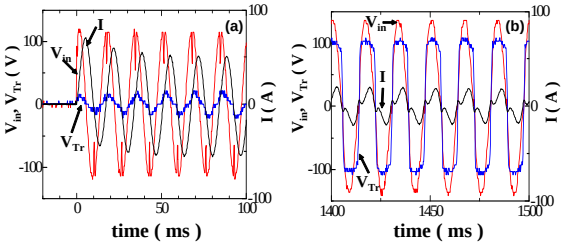

Fig.4 Typical waveforms of $V_{\rm in}$, $V_{\rm Tr}$ and I (a) in the initial stage of and (b) at the end of the charging process.

In order to evaluate the repetition rate of the developed Marx generator, the time history of the charging voltage during the charging process was measured and is shown in Fig.5. The repetition rate of the system is defined as the inverse number of the charging period, i.e., the time Marx generator is charged up to the rated output voltage(50 kV) of the transformer when the rated input voltage is applied. We see from Fig.5 that the charging period is around 1500 ms, hence the repetition rate of this system is evaluated to be 0.67 Hz.

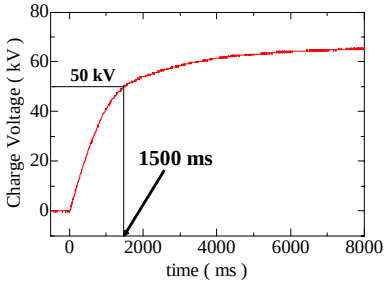

Fig.5 Typical time history of the charge voltage.

Figure 6 shows the time history of the input energy($E_{\rm in}$) and the energy stored in the Marx generator($E_{\rm ch}$). $E_{\rm in}$ and $E_{\rm ch}$ were calculated by the following equations:

$$E_{\rm in} = \int (V_{\rm in} \cdot I) dt, \quad E_{\rm ch} = \frac{1}{2} C {V_{\rm ch}}^2$$

where C and $V_{\rm ch}$ are the capacitance 36.7 nF and the charging voltage of the Marx generator, respectively. The energy efficiency of the system is defined as $\xi = E_{\rm ch}/E_{\rm in}$. The dependence of the energy efficiency on the input voltage is summarized in Table I. The obtained energy efficiency is $\xi \simeq 95$ %. From Table I it is found that the energy efficiency tends to decrease with the increase of the input voltage. The energy loss is considered to be due to the resistance of the inductor L_1 for the current limiter.

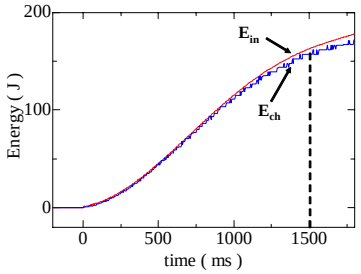

Fig.6 Time history of the input energy($E_{\rm in}$) and the charging energy($E_{\rm ch}$).

Table.1 Dependence of the energy efficiency on the input voltage.

Input voltage (V)	Energy efficiency (%)
30	95.8
40	95
50	94

Figure 7 shows typical output voltage waveform of the developed Marx Generator. The pulse voltage was measured by the resistive voltage divider placed in the PFL. From Fig.7, it is found that the peak voltage and the FWHM of the pulse are ~120 kV and 200 ns, respectively. Considering that the charging voltage per stage is 40 V, the measured voltage is in good agreement with the theoretical calculation.

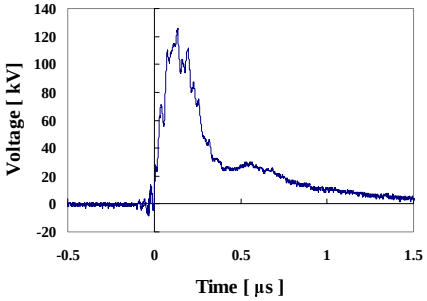

Fig.7 Typical output voltage waveform of Marx generator.

4 Summary

The repetitively pulsed power generator, which consists of a Marx generator with a new configuration and a pulse forming line, have been designed and developed to operate the ion diode at a repetition rate of 1 Hz. From the evaluation of the developed Marx generator, the pulsed power generator can operate with repetition rate of around 0.7 Hz. To improve the repetition rate the charging time of the Marx generator should be reduced. After the improvement of the developed generator, it will be applied for an ion diode.

Acknowledgement

This work is supported in part by the Grant-in-Aid for Scientific Research from the Ministry of Education, Science, Sports and Culture, Japan.

References

[1] W. Partlo, R. Sandstrom and I. Fomenkov, Proc. SPIE, **2440**, 90 (1995).

[2] H. Mizoguti, O. Wakabayasi, T. Aruga, T. Sakugawa and T. Koganezawa, Proc. SPIE, **2726**, 831 (1996).

Evaluation of switching characteristics of SiC-JFET for pulsed power application

Kazumasa Narita, Hirokazu Honma, Tomoyuki Yokoo, Weihua Jiang

Extrem Energy-Density Reserch Institute, Nagaoka University of Technology,

1603-1, Kamitomiokacho, Nagaoka, Niigata, 940-2188, Japan

ABSTRACT

SiC power devices are predicted greatly exceeding performance of existing semiconductor devices, and can expect the applications of MHz level repetitive high voltage modulator. This paper reports an initial experiment on evaluation of the switching characteristics of SiC-JFETs. The measurement was carried out by outputting pulse high voltage of 1kV with 200 ns pulse width. With load resistance of 223 Ω, turn-on time of 17.7 ns, turn-off time of 34.9 ns and switching loss of 60 μJ were obtained respectively. And these characteristics were also measured at the element temperature of 200 degrees. In addition, 2 kV switching operation was obtained by 2 series connection of SiC-JFET.

1. Introduction

In generally, Si semiconductor devices has been used for pulsed power generators. Especially, Si-MOSFET is used for the high repetitive pulsed power generator which needs a several hundred kHz repetitive operation. The switching capability of a one Si device is lower than the demand of pulsed power generator. Therefore, increasing the switching capability by multistage series connection of device is necessary to satisfy the demand. However, this method leads to increasing of switching loss and hugeness of the system by switching device. To solve these problems fundamentally, improving allowable power of the device is necessary. But it is difficult to hope the capability improvement of Si device. Because these are restricted by the physical property of Si semiconductor.

Recently, silicon carbide (SiC) which is one of the wide band gap semiconductor is attracts attention, since the material property values of the SiC semiconductor greatly exceed the Si semiconductor's one. When SiC is applied to power device, it is possible to make the high power device which is low on-time resistance and is stable in the high temperature. As a result, it can be expected drastic miniaturization and performance improvement of the above pulsed power generator systems.

In this paper, the characteristics of SiC-JFET which is one of the SiC power device is studied. We have paid special attention on switching speed, on-time resistance, switching loss and high temperature characteristics. These characteristics are important for utilizing in the pulsed power. In addition, the switching characteristic of 2 series connection is reported.

2. SiC-JFET

Figure 1 shows the photograph of the SiC power device used in this experiment. It is a SiC-JFET made by SiCED Electronics Development GmbH & Co.KG. As shown in the photograph, general TO-220 type package is used with this SiC-JFET. The withstand voltage and maximum current (DC) are 1500 V and 5A, respectively.

Junction FET is normaly-on device. In the experiment, it is necessary to know the threshold voltage which makes SiC-JFET off-state. Therefore, static behavior of SiC-JFET was measured in preliminary experiments. As a result, changing off-state from on-state of this JFET was confirmed at the gate voltage between -22 V and -23 V.

Fig. 1 Phograph of the SiC-JFET used in this experiment.

3. Switching characteristics of SiC-JFET

3.1 Measuring circuit The schematic circuit diagram for measurement of switching characteristics is shown in Figure 2. From the result of static behavior, rectangle wave below -24 volts was used as the gate-source voltage to make SiC-JFET off-state. Then, each experiments were carried out at room temperature of 20 degrees, except for the measurement of high temperature characteristics.

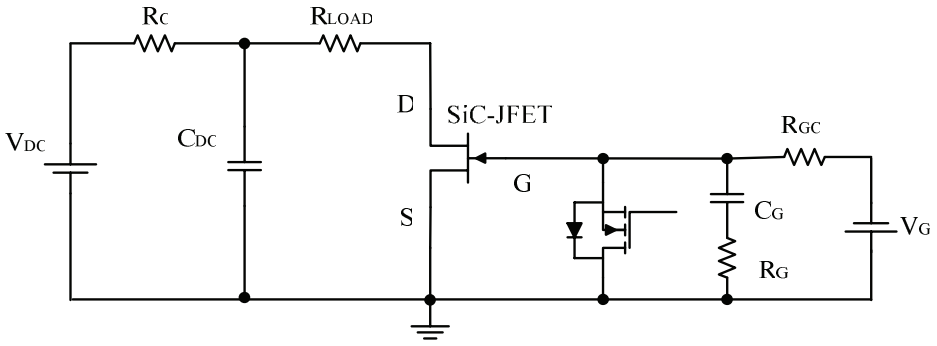

Fig. 2 Circuit for measurement of SiC-JFET switching characteristics.

3.2 Measurement of on-time resistance

The experimental conditions for measurement of the on-time resistance are shown in Table 1. The capacitor C was charged up to 1 kV by the DC power supply, the drain-source voltage V_{DC} and the load resistance voltage V_{RL} were measured. The drain current I_D was calculated from the V_{RL}, and the on-time resistance was obtained from the V_{DS} and I_D. For calculating the on-time resistance, it is important to measure V_{DS} exactly.

Table 1 Experimental conditions of measurement of on-time resistance.

V_{DC}	1 kV	R_G	2.5 Ω
C_{DC}	10μF	C_G	300 μF
R_C	15 kΩ	V_G	-24 V
R_{LOAD}	223 Ω	Pulse Width	20 μs

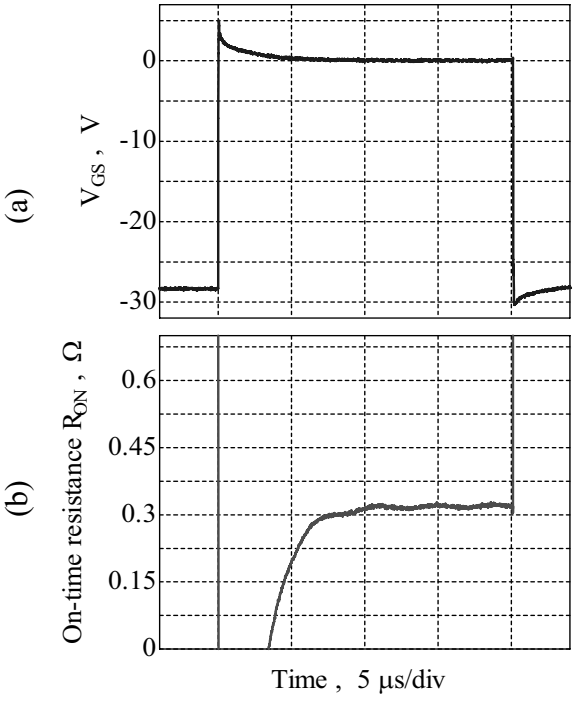

Fig. 3 Waveform of calculated gate-source voltage (a) and on-time resistance (b).

Then, the measurement circuit which consist of series connection of 10 V zener diode and 125 kΩ current limitation resistance was parallelly connected with SiC-JFET. Therefore, since V_{DS} is clamped in the Zener voltage, it is possible to measure V_{DS} by the low voltage probe which is good frequency characteristics.

The waveform of the gate–source voltage and calculated on-time resistance R_{ON} at the 20 μs pulse width are shown in Figure 3. Due to the stray capacitance of the circuit and frequency characteristics of the probe, waveform of on-time resistance has not been stabilized shortly after turn-on. But the minimum value 0.32 Ω of on-resistance was obtained after 10 μs from turn-on.

3.3 Single and repetitive operation The experimental conditions at the single and repetitive operation are shown in Table 2.

Table 2 Experimental conditions of single and repetitive operation.

V_{DC}	1 kV	R_G	2.5 Ω
C_{DC}	10μF	C_G	300 μF
R_C	15 kΩ	V_G	-30 V
R_{LOAD}	223 Ω	Pulse Width	
Repetition Rate	4 MHz (Burst)	single	200ns
		repetitive	100ns

The waveform of gate-source voltage V_{GS} and drain-source voltage V_{DS} at the single operation are shown in Figure 4. Turn-on time and turn-off time were 17.7 ns and 34.9 ns, respectively.

The waveforme of V_{GS} and V_{DS} at the repetitive operation are shown in Figure 5. This is the same as the shape of waves at the single shot operation excluding 100 ns the Pulse time width.. In Figure 5, one period of V_{DS} waveform was 250 ns. Therefore, 4 MHz repetitive operation can be confirmed.

3.4 The calculation of switching loss The switching loss was calculated by integrating power which was calculated by the multiplication of V_{DS} and I_D which were measured by the single-operation described in the previous section. The waveform of calculated switching loss is shown in Figure 6. From this result, the switching loss of about 60 μJ was obtained. This value is almost equal compared to switching loss of nearly same rating Si-MOSFET like a 2SK2611.

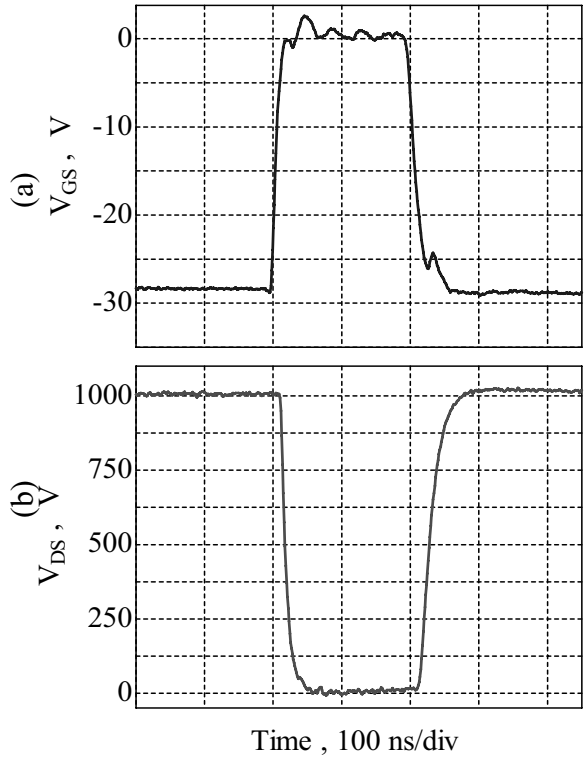

Fig. 4 Waveforms of drain-source voltage (a) and gate-source voltage (b) at single operation.

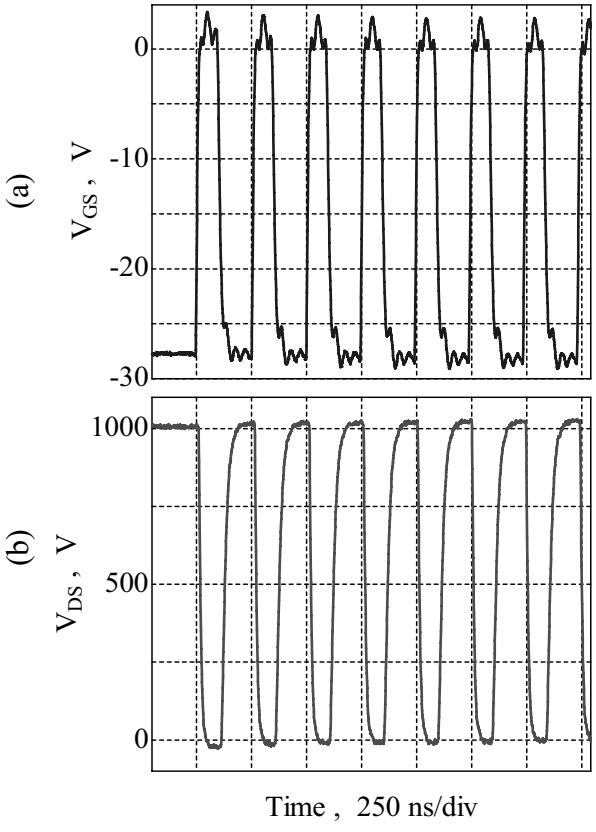

Fig. 5 Waveforms of drain-source voltage (a) and gate-source voltage (b) at repititive operation.

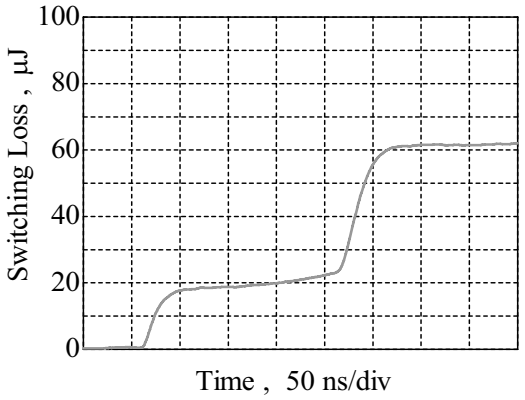

Fig. 6 Waveform of calculated switching loss of SiC-JFET

3.5 High temperature characteristics In this experiment, high temperature characteristics of SiC-JFET were measured with heating back plate of the element up to 200 degrees by electric heater. The experimental conditions for measurement of high temperature characteristics are shown in Table 3.

First of all, the on-time resistance was measured, and the minimum value 1.1 Ω was obtained.

Table 3 Experimental conditions of measurement of high temperture characteristics.

V_{DC}	1 kV	R_G	2.5 Ω
C_{DC}	10μF	C_G	300 μF
R_C	15 kΩ	V_G	-30 V
Pulse Width	200 ns	R_{LOAD}	223 Ω
Element Temperature	200℃		

The waveform of V_{DS}, V_{GS} and the calculated switching loss are shown in Figure 7.

Turn-on time and turn-off time of V_{DS} were 27.2 ns and 59.8 ns, respectively. The V_{GS} waveform is only that the ringing amplitude changes a little in comparison with Figure5, switching speed is almost same. But turn-on and turn-off time of V_{DS} slowed down about 10-25 ns. This cause is thought that the resistance of the channel seems to increase due to the rise in the element temperature. The switching loss was increased about 25 μJ. However, the MHz-level switching is practicable even in the above characteristics. It is considered that the above characteristics deterioration dosen't become a hardly probrem in the operation .

3.6 2 series connection The switching characteristics of 2 series connection SiC-JFET was measured. The experimental conditions are shown in Table 4.

At first, the problem of the voltage unbalance was occurred. However, it was solved by adjusting the turn-on and turn-off time of the V_{GS} to equalize the V_{DS} switching speed of each SiC-JFET.

2 kV switching waveform by 2 series connection SiC-JFET is shown in Figure 8. Turn-on time and turn-off time were 49 ns and 76 ns, respectively.

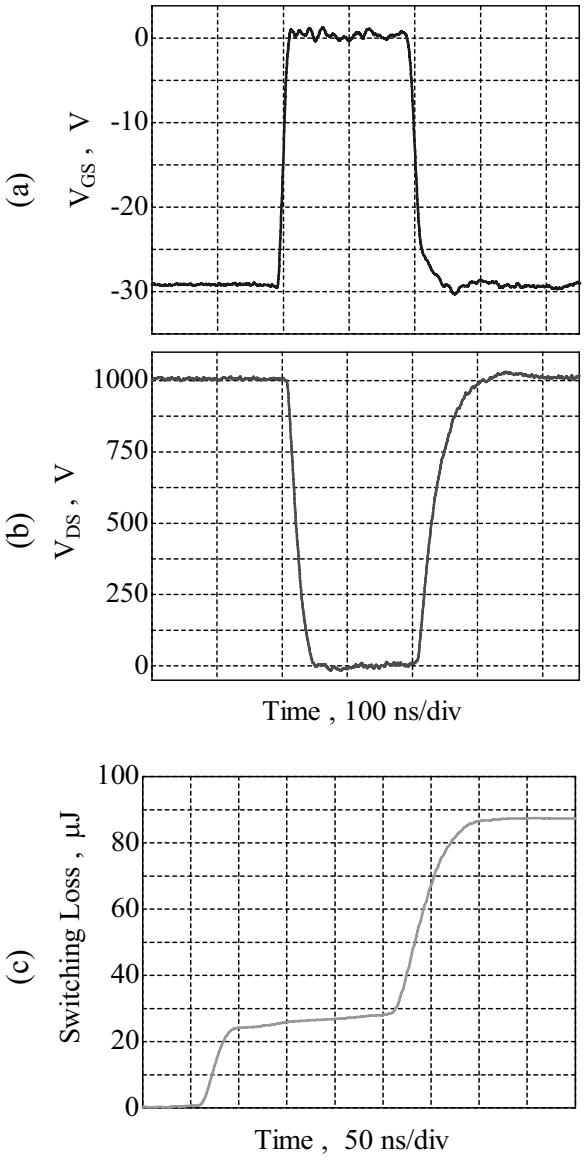

Fig. 7 Waveforms of drain-source voltage (a), gate-source voltage (b) and calculated switching loss (c).

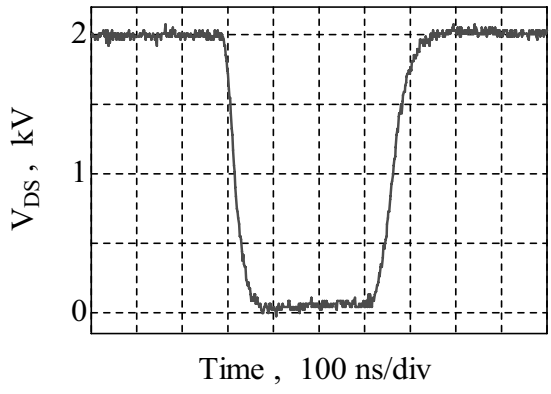

Fig. 8 Waveform of 2 kV switching by 2 series connection SiC-JFET.

Table 4 Experimental conditions of measurement of the switching characteristics of 2 series connection SiC-JFET

V_{DC}	2 kV	R_G	2.5 Ω
C_{DC}	10μF	C_G	300 μF
R_C	15 kΩ	V_G	-24 V
R_{LOAD}	450 Ω	Pulse Width	300 ns

4. Summery

The switching characteristics of SiC power device was studied for application to high repetitive pulsed power generator.

The drain-source on-time resistance of about 0.32 Ω was obtained. Repetitive operation at 4 MHz was confirmed. With operating at 1 kV and load resistance of 223 Ω, the turn-on time of 17.7 ns, and turn-off time of 34.9 ns were obtained, respectively. Then, the switching loss of about 60 μJ was obtained.

High temperature characteristics of 200 degrees were measured. The drain-source on-time resistance of about 1.1 Ω was obtained. Turn-on time and turn-off time of V_{DS} were 27.2 ns and 59.8 ns, respectively. Therefore, the switching loss of about 85 μJ was obtained. Each characteristics was deteriorated in comparison with the result of the measurement at 20 degrees. However, it seems to not large problem, because the MHz-level repetitive operation is practicable even in these characteristics.

Finally, 2 kV switching characteristic by 2 series connection of SiC-JFET was measured. Turn-on time and turn-off time were 49 ns and 76 ns, respectively.

5. References

(1) K. Arai and S. Yoshida : “SiC 素子の基礎と応用”, オーム社 (2003)
(2) Y. Sugawara : “SiC パワーデバイスの開発状況”, IEEJ Journal, Vol.118, No.5, p.282-285 (1998)
(3) Y. Sugawara : “進展著しい SiC パワーデバイスと適用装置の開発”, IEEJ Journal, Vol.125, No.1, p.25-28 (2005)

Repetitive Pulsed Power Generation using Semiconductor Opening Switch

Kunihiko Saiki, Tomoyuki Yokoo, Kazuaki Hotta, and Weihua Jiang

Extreme Energy-Density Research Institute, Nagaoka University of Technology, 1603-1 Kamitomiokacho, Nagaoka, Niigata, 940-2111, Japan

ABSTRACT

The Pulsed power generator using SOS (Semiconductor Opening Switch) is one way to generate high voltage short pulse. In general, the repetitive rate of the pulsed power generator using SOS was restricted up to 100 [kHz] by frequency characteristics of magnetic cores. For further improvement of repetition rate, we developed a pulsed power generator that all switching devices are semiconductor device. In this circuit, forward current of SOS is supplied by DC to shorten its operation duration. Initial test was carried out and ~9.8 [kV] of output voltage is obtained at 1 [kΩ] of resistive load. Repetitive rate of this circuit achieved 500 [kHz].

I. Introduction

Pulsed power generator, which has several decades kV of output voltage and several decades – 100 ns of pulse duration, is often used to generate nonequilibrium plasma in electric discharge at atmospheric pressure. It has attractive futures for sterilization, surface treatment, treatment of toxic substance, and new method of material engineering, and so on. Therefore, development of pulsed power supply which generates high voltage short pulse has been required.

Pulsed power supply which is based on the inductive energy storage system is part of high voltage short pulse generator. In this system, the current of inductor is rapidly cut off by an opening switch, and the induction voltage is generated by current interruption of inductor. If the characteristics of opening switch is superior (e.g. rapidly current interruption, high withstand voltage, and large current capacity), the high voltage short pulse is obtained. So the high voltage short pulse is output to the load at inductive energy storage system. And, the pulse width of high voltage short pulse is very short, so high repetitive rate of generator is desirable for obtaining continuous output.

The diodes have characteristics of current interruption if reverse current flows after flowing of forward current. The diodes are able to be used as opening switch by using this characteristic. Semiconductor opening switch (SOS) which is developed in Russia in recent years is suitable for opening switch of pulse power supply. SOS is Semiconductor device, so its life and ability of high-repetitive operation is favorable compared with traditional opening switch.

The traditional pulse power supply using SOS use magnetic switch, so the period of time which reset magnetic core to initial condition is required every operation[1]. Therefore, repetitive rate of SOS is

limited to about 100 kHz[2]. The circuit where all switching devices are constructed by semiconductor device is designed for enhancement of repetitive rate. Furthermore, the forward current which is generally supplied by half-sine wave is supplied as direct current for improvement of repetitive rate.

In this paper, details of this circuit and initial test results are described.

II. Operation method of SOS

Repetitive pulsed power generators which use SOS usually employ magnetic switches. The magnetic core of magnetic switch is saturated by operation. For use magnetic switches again, it is necessary to reset magnetic core to initial condition. Heretofore, the reset operation is done by direct current or pulse current. The repetitive operation is limited by such a period of time of reset.

To lift restriction due to frequency characteristics of magnetic core against repetitive rate, it is thought that replacement of magnetic switches by semiconductor switching device which is able to operate high-speed operation (e.g. MOSFET). Switching capability of these semiconductor devices is lower than the magnetic switch. Therefore, the output power of every shot is also low. However, the average power is able to increase by increasing repetitive rate.

The following process is necessary for operation of SOS. At first, the forward current flows through the SOS. After that, the reverse current flows through the SOS. After that, the SOS operates as an opening switch. In general, the forward current is supplied as half-sine current pulse at every operation. However, the forward current is supplied as DC current at this time. From this change, the enhancement of repetition rate becomes available.

Figure 1 shows the proposed circuit.

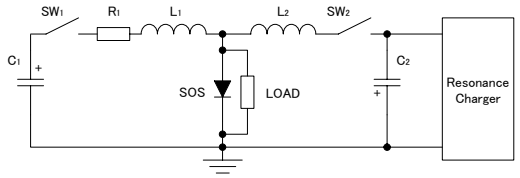

Fig. 1 Proposed circuit

This circuit consists of forward current supplying unit on the left side of SOS, reverse current supplying unit on the right side of SOS, and the resonance charger.

In the proposed circuit of Fig. 1, the forward current is always supplied as DC current. So the operation of forward current supplying is not necessary every shot and SOS can operate by only operation of reverse current supplying. Therefore, the period of time that is required for obtaining high voltage short pulse is able to become shorter, and repetition rate can be higher.

Ⅲ. Experimental circuit and circuit operation

The actual experimental circuit is shown in figure 2.

The forward current supplying unit consists of C_0,

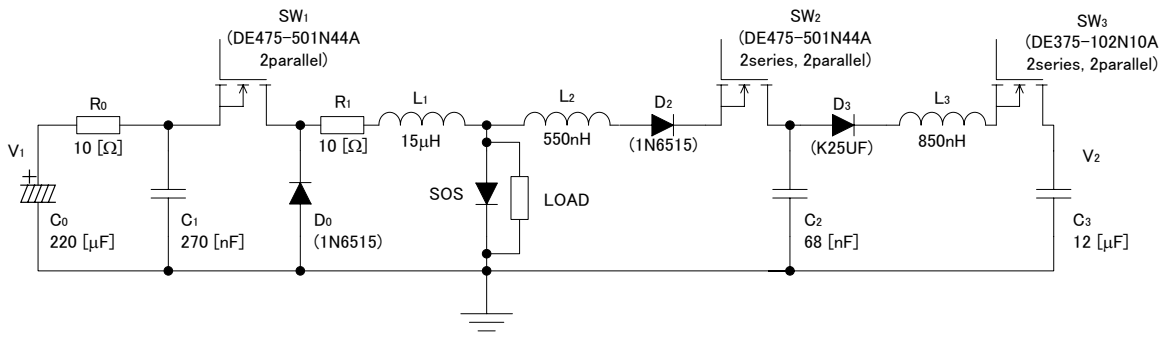

Fig. 2 Experimental circuit

R_0, C_1, SW_1, D_0, R_1, and L_1. SW_1 consists of 2 parallel MOSFETs of type DE475-501N44A (IXYS). D_0 is diode of type 1N6515 (Voltage Multiplier INC.). This section supplies rectangle current pulse by CR discharge of R_0, R_1, C_0, and C_1. SW_1 and D_0 are added for burst mode operation.

The reverse current supplying unit consists of C_2, SW_2, D_2, and L_2. SW_2 consists of 2 parallel and 2 series MOSFETs of type DE475-501N44A (IXYS). D_2 is diode of type 1N6515 (Voltage Multiplier INC.). The resonance charger consists of C_3, SW_3, D_3, and L_3. SW_3 consists of 2 parallel and 2 series MOSFETs of type DE375-102N10A (IXYS). D_3 is diode of type K25UF (Voltage Multiplier INC.). The SOS consists of 6 elements of SOS-60-4 (High Current Energy Institute, Russian Academy of Science).

The circuit operation is described as follows with circuit operation. Table 1 shows experimental conditions.

Figure 3 shows initial operation waveform of I_{SOS} and V_{SOS} obtained at 100 [Ω] of resistive load. Figure 4 shows part steady operation waveforms at 100 [Ω] of resistive load.

Table 1 Experimental conditions

V_1 (charging voltage of C_0)	300 [V]
V_2 (charging voltage of C_3)	-750 [V]
Period of resonance charging	750 [ns]
The pulse width of reverse current	600 [ns]
Repetitive frequency	500 [kHz], (30 shot burst mode)

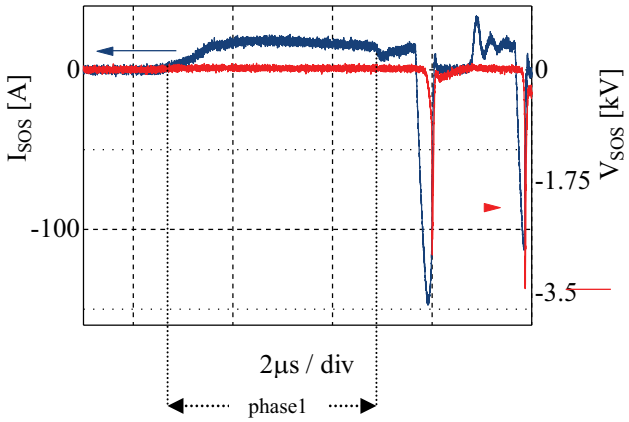

Fig. 3 Initial operation waveform obtained at 100 [Ω] of resistive load

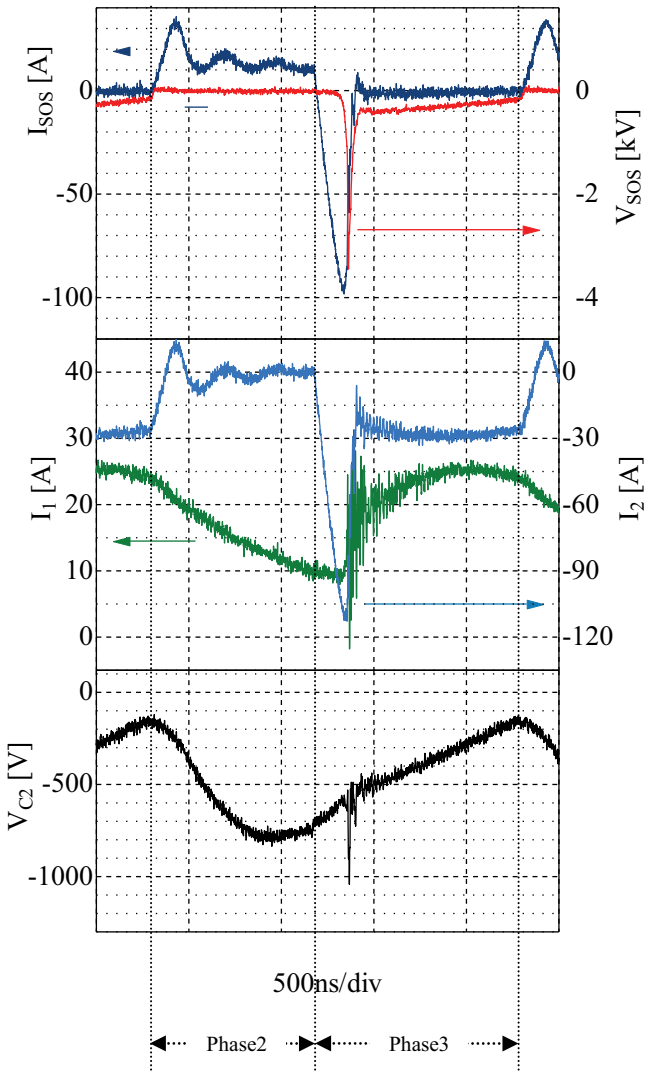

Fig. 4 Part steady operation waveforms obtained at 100 [Ω] of resistive load

Initially, the C_0 and C_3 are charged up to V_1 and V_2 respectively by DC power supplies.

The circuit operation can be described by following 3 phases.

1. The initial phase of operation

SW_1 is turned off, SW_2 is turned on, and SW_3 is turned off before operation.

At first, SW_1 is turned on. Then the forward current flows through the SOS shown in Fig. 3. Hereafter, SW_1 is kept on until the burst operation finishes.

2. When SW_2 is turned off and SW_3 is turned on

In this phase, C_2 which is source of reverse current is charged by resonance charger. After charging, the phase makes the transition to phase 3. At the same time, this phase is period of forward current flowing through the SOS at continuous operation.

3. When SW_2 is turned on and SW_3 is turned off

In this phase, C_2 had been charged in initial. So this phase differs from phase 1. Therefore, the current due to the LC resonance of C_2 and L_2 flows to the SOS when switching of SW_2. The current supplied from C_2 is higher than the forward current. Therefore, the forward current of SOS is canceled and the reverse current flows to the SOS.

As results of these phases, reverse current follows trapezoidal forward current flows through the SOS. And then, this reverse current is interrupted and high voltage pulse arises to the load. The output voltage is mostly applied to the LOAD, L_1, and L_2. So the output voltage does not destroy the circuit element (e.g. MOSFETs, Diodes).

After the current interruption of SOS, the stored energy of C_2 and L_2 is discharged to the load. And the phase makes transition to phase 2 by switching of SW_2 and SW_3. Then, the stored energy of C_2 is kept; on the other hand, the storage energy of L_2 is absorbed by snubber of SW_2.

The high voltage short pulse can generate repetitively by repeat of the phase 2 and 3.

Ⅳ. Experimental result and discussion

Figure 5 shows waveforms of V_{SOS} obtained at 100 [Ω] of resistive load.

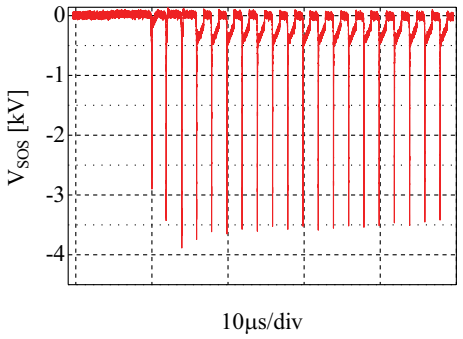

Fig. 5 Waveform of V_{SOS} obtained at 100 [Ω] of resistive load

In fig. 5, there is a difference of peak value of output voltage at initial operation. These differences blow over after few shots. So it is confirmed that stable output is available at 500 [kHz].

The pulse width of forward current is different at primary stage of operation. It causes that the forward current pulse width which longer than the following shots the difference of peak voltage. The forward current become stable after few shot, so the peak value of output voltage becomes stable too.

Figure 6 shows waveform of V_{SOS} obtained at 1 [kΩ] of resistive load.

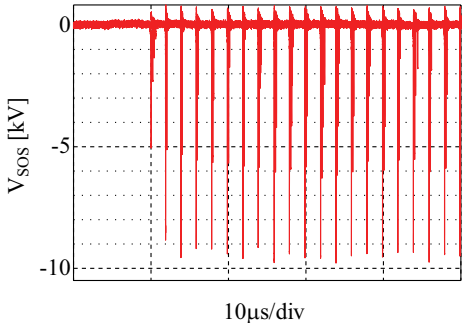

Fig. 6 Waveform of V_{SOS} obtained at 1[kΩ] of resistive load

From fig. 6, the peak value of output voltage is higher than that is at 100 [Ω] of resistive load. The output voltage becomes stable after few shot alike. It is shown that the 500 [kHz] operation is available at varied resistance of load.

Figure 7 shows extended view of the waveforms of I_{SOS} and V_{SOS} at current interruption of SOS at 1 [kΩ] of resistive load.

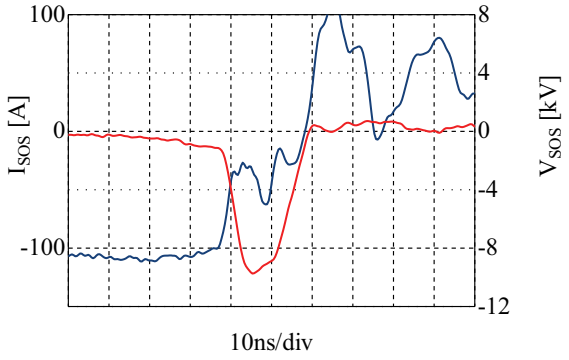

Fig. 7 Expanded operation waveform of I_{SOS} and V_{SOS} obtained at 1 [kΩ] of resistive load

From fig. 7, the rise time, FWHM, and peak voltage are 14 [ns], 14.4 [ns], and 9.78 [kV], respectively.

Next, the repetition rate is discussed. The phases 2 and 3 are necessary for repetitive operation.

The phase 2 is the period of time of resonance charging. The phase 3 is the period of time of reverse current pumping and discharging of storage energy to the load. The repetitive rate is able to be improved by decrease of these three phases.

The period of time of resonance charging and reverse current pumping depends on circuit constants. To make the period of time short, it is necessary to change the circuit constants.

The discharging duration of storage energy to the load is able to make short by shorten on-time of SW_2. But many storage energy stay in the circuit if this period of time is become short. So the snubber capacity had to be increased for protection of SW_2.

The experimental result at 100 [Ω] of resistive load is used for evaluation of energy transfer efficiency of this circuit. The released energy of C_2 every time is used as normal for calculation of efficiency.

The released energy from C_2 is 19.6 [mJ], and the discharged energy for load is 2.75 [mJ]. Therefore, energy transfer efficiency of output is calculated at about 14%. The rest of energy that is about 86% is consumed as a heat in the circuit.

The factors of dissipation of this circuit are SOS, SW_2, and R_1. At the current interruption of SOS, a part of current through the SOS is transferred to the L_1. The transferred current of L_1 is used for forward current and consumed in the R_1. So R1 is defined as factor of dissipation. The loss SOS, SW_2, and R_1 are, respectively, 6.75 [mJ], 2.19 [mJ], 4.79 [mJ]. These losses depend on circuit parameters. So the loss is able to be decreased as far as it goes by adjustment of circuit parameters.

If the loss is too much, the idle period is needed to cool circuit while operation. So the circuit can operates burst operation only. Therefore, it is necessary to discuss of improvement of efficiency.

Ⅴ. Conclusion

A new operation method of SOS, which is characterized by full semiconductor switching and DC supply of forward current, has been proposed. High repetition has been demonstrated by experimental results.

The circuit is successfully operated at 500 [kHz] of repetition rate in burst mode. The stable operation is available for different load resistance. However, improvement of energy efficiency and adjustment of circuit parameters are necessary as future development.

From these results, the proposed operation method is proved to be effective for enhancement of repetition rate of SOS based pulsed power generator.

REFERRENCES

1) T. Yokoo, K. Saiki and W. Jiang : ”Development of SOS Generator for Atmospheric Pressure Discharge”, The paper of Joint Technical Meeting on Plasma Science and Technology and Pulsed Power Technology, IEE JAPAN,PPT-06-47

2) A.V. Ponomarev, S.V. Lozhkin, S.N. Rukin, S.N. Tsyranov, and P.V. Vasiliev, “SOS-Based Generator with 100-kHz Pulse Repetition Frequency”, 27th Power Modulator Symposium And 2006 High Voltage Workshop, May 14-18 2006, P2-SS-2

CONTROLL OF ATMOSPHERIC PRESSURE TRANSIENT GLOW DISCHARGE IN MICROGAP ELETCTODES UTILIZING HIGH VOLTAGE PULSE GENERATOR

S.Ibuka*, F.Furuya, K.Ogura, K.Yasuoka, and S.Ishii

Department of Electrical and Electronic Engineering, Tokyo Institute of Technology
2-12-1-S3-9 O-okayama, Meguro-ku, Tokyo, Japan

Abstract

Stabilization of transient glow discharge in microgap electrodes with miniature helium gas flow was discussed experimentally. Various types of the cathode electrodes including a needle, sphere and flat plate were examined from the viewpoint of extending the sustaining duration of the transient glow discharges. The flat plate cathode with a smooth surface was the most advantageous for obtaining the long duration transient glow discharge. The effect of the waveform of driving pulsed voltage was also investigated utilizing a newly designed burst pulse generator with a nonlinear transmission line. We proposed a novel technique of driving with a fast high-voltage pulse train and successfully confirmed its effect of suppressing a glow-to-arc transition.

I. Introduction

An atmospheric pressure glow discharge (APGD) attracts significant interests of many researchers in the field of plasma applications, because of its special features appropriate for industrial applications [1]. To obtain stable APGDs, a key issue is the suppression of a glow-to-arc transition. A number of attempts have so far been made to realize effective suppression of the glow-to-arc transition, such as forced cooling of electrodes, utilization of high frequency voltage, dielectric barrier discharges, and external electron sources [2-4]. However, the stabilization mechanism of APGD has not been fully investigated.

In recent years, utilization of microplasmas, which were produced in the microgaps of 10-1000μm in electrode separation, was proposed as a promising candidate to obtain stable APGDs. The small size of the microplasma obstructs the growth of spatial instability. In addition, the microplasmas have a very large specific surface area. This enhances the energy losses to the wall or ambient gases, consequently the microplasmas are usually in a non-equilibrium state. The non-equilibrium plasmas with the small scale have advantages for the applications of plasma chemistry and plasma processing, such as maskless etching of silicon, surface modifications of polymeric film substrates, plasma sterilization and so on [5-8].

Schoenbach et al. proposed a micro hollow cathode configuration to generate the high density APGD [9]. T. Yokoyama et al. reported the utilization of a miniature gas flow to obtain direct current APGDs with helium and argon [10]. Their method is advantageous for applications such as thin-film deposition and plasma fine processing because the microplasma is generated without a confining wall. Although a simple apparatus of the direct current driving method is preferable for the industrial applications, the difficulty in controlling the injection energy to the microplasma narrows the application area.

To obtain the high power APGD, we propose to utilize a transient glow micro discharge with short pulsed voltage [11]. The transient glow discharge is one of the most well-known techniques to obtain the high pressure glow plasma in which the pulsed voltage is made zero before the glow-to-arc transition. It is possible to generate the high power density glow plasma. In the previous study, we reported the preliminary experiments for the generation of transient glow microplasmas and illustrated the possibility to obtain high power transient glow APGDs [11]. In the

case of the atmospheric pressure discharge in microgaps, the transient glow discharge is sustained for the duration of the order of typically 100ns [11]. However, it is not easy to obtain such an extremely short pulse with the conventional power semiconductor devices. The repetition frequency of the driving circuit limits the average injection power below few watts. In this paper, we propose a novel driving technique using burst pulse generator with a nonlinear transmission line to realize high average power operation of the transient glow microplasma. The stabilization of the transient glow discharge in the microgaps with various shapes of cathode was also investigated to obtain the transient glow discharge with the long sustaining duration.

II. Experimental Setup

The miniature electrode system was assembled in con-junction of a stainless steel nozzle anode and several kinds of metal cathodes, which include a sphere and a needle of tungsten carbide and plane plate made of stainless steel or molybdenum as shown in Fig.1. The diameter of the sphere was 2mm or 1mm. The radius of curvature of the needle was 50μm. The inner and the outer diameter of the nozzle electrode were 190μm and 350μm respectively. Helium flowing out of the nozzle was fed between the electrodes in air. A mass flow controller adjusted the helium flow rate ranging from 30 to 200sccm. The electrodes were placed on the micro positioning stages to control the electrode separation in the range of micron order. The applied voltage to the electrodes was monitored using a high voltage probe. A current monitor was used to measure the discharge current. The voltage and the current waveforms were recorded by a digital storage oscilloscope. The macroscopic behavior of the discharge was monitored using a CCD camera with a microscope lens because the size of microplasmas was below 1mm, which is difficult for naked eyes to recognize. An image intensified CCD (ICCD) camera was used to observe temporal and spatial behavior of the discharges. To investigate detailed characteristics of the microplasma, a spectrometer was also used.

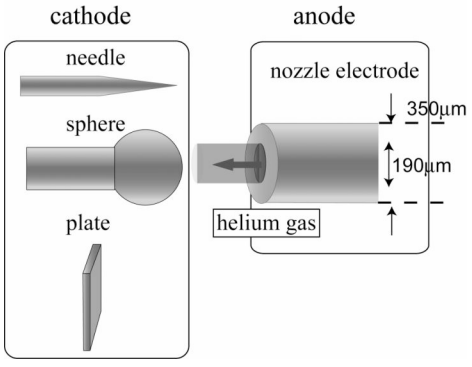

Fig.1 Configuration of the microgap electrodes.

III. Pulse Generator with Nonlinear Transmission Line

In the previous study, we used a pulse forming line (PFL) scheme using 3C-2V coaxial cables to obtain high-voltage short pulses [11]. Although the PFL is superior configuration to produce the fast rectangular high-voltage pulses, the size of the pulse generator becomes large because of the utilization of the coaxial cables. The size of the generator is an important factor to realize the industrial applications of the microplasma in various fields. In this study, we developed a pulse generator that consists of a pulse forming network (PFN) and a nonlinear transmission line (NLTL). The PFN, which consists of a linear LC ladder circuit and high-voltage switching devices, is favorably compact and can be utilized to generate high voltage pulses having 90 to 1000ns of the pulse width. To realize repetitive operation of up to 1kHz and the output voltage, which is high enough to drive discharges in the microgaps, three fast high-voltage power semiconductors of IGBT (SIEMENS BUP313) are connected in series as the switching devices. The rated voltage of the IGBT is 1.2kV and the stacked switching device is safely operated up to 3kV.

The NLTL is composed of a ladder circuit with air-core inductors and nonlinear capacitors of which characteristics are depending on the voltage as shown in Fig.2. The nonlinear capacitors are not commercially available because capacitors are usually specified to use in the region of constant capacitance. We used chip monolithic

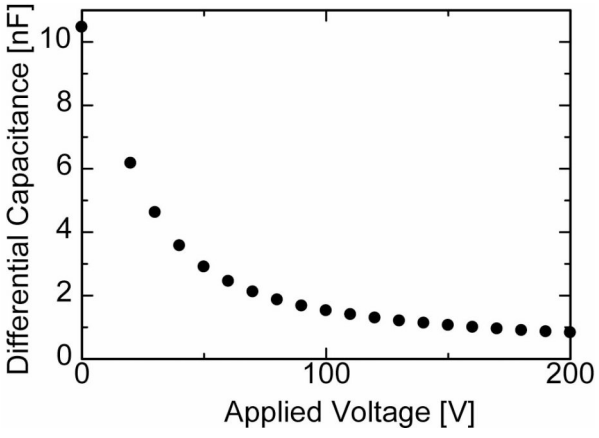

Fig.2 C-V characteristics of the ceramic capacitor.

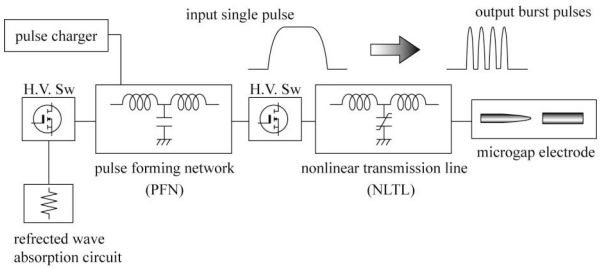

Fig.3 Block diagram of the pulse generator.

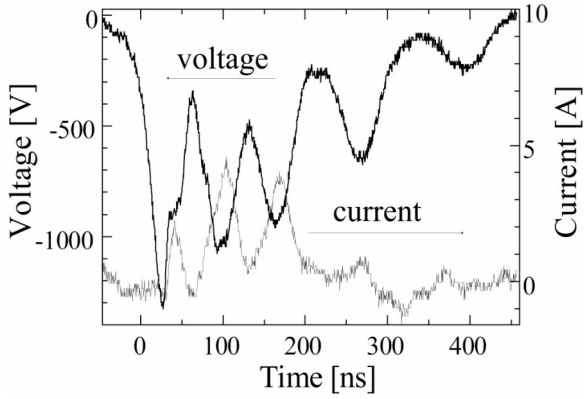

Fig.4 Typical voltage and current waveform of the pulse generator.

ceramic capacitors as nonlinear elements. The laminating structure of thin ferroelectric ceramics layers makes dielectric breakdown voltages high enough to establish strong nonlinear characteristics. Fig.3 shows a block diagram of the pulse generator. A rectangular high voltage pulse generated by the PFN is fed into the NLTL, in which the input voltage pulse propagates as a nonlinear wave and changes its temporal shape and finally it breaks up into several burst pulses with short duration [12].

Generally, it is difficult to obtain impedance matching completely between the generator and the load. Therefore, we added a reflected wave absorption circuit to eliminate the unwanted wave that was originated from the impedance mismatching as show in Fig.3. Fig.4 shows a typical voltage and current waveform of the pulse generator. The initial rectangular pulse with 300 ns duration generated by the PFN becomes the pulse train of three large solitary waves having 40ns pulse width in FWHM and followed by two small amplitude ripples. The interval of each solitary wave is 80ns. It is noted that the circuit parameters of the NLTL and the PFN should be adjusted as appropriate value to minimize the energy loss caused by the ripple generation.

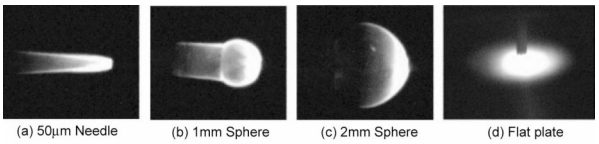

Fig.5 ICCD photographs of the transient glow discharge for various cathode shapes.

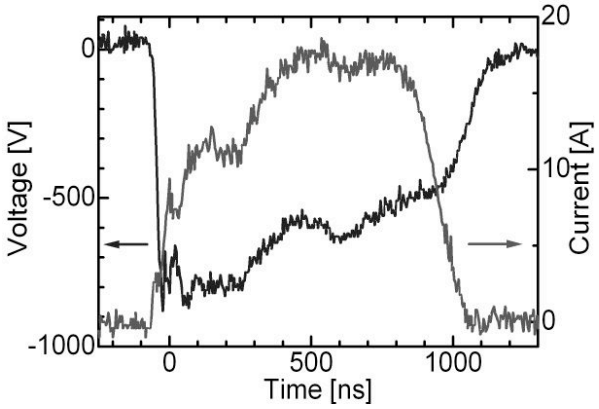

Fig.6 Voltage and current waveform of transient glow discharge with the plain shape stainless steel cathode.

IV. Effect of The Cathode Shape

We examined transient glow discharges using the four kinds of cathode as shown in Fig.1. Stable glow discharges are characterized as the appearance of non-zero sustaining voltages and negative glow emission covering the cathode surface uniformly. Fig.5 shows the CCD photographs of the transient glow discharges for each cathode, which is covered with uniform emission light. However, the duration of the transient glow discharge varied with the cathode shape. Although the applied voltages were the rectangular pulses with a pulse width of 1μs, which were the output from the PFN in the circuit shown in Fig.3, the duration of the transient glow was approximately 70ns for the needle cathode, 100ns for the sphere one. On the other hand, it was 1μs for the flat plate cathode. We can conclude that the glow discharge with longer duration is obtained using the cathode with a flat surface. Fig.6 shows the gap voltage and the discharge current waveforms for the discharge with the flat plate stainless steel cathode. The injected energy into the discharge calculated by integrating the products of the voltage and the current is 20mJ. The average power reaches 20W for the repetitive operation of 1kHz, while the direct current operation of the atmospheric pressure glow discharge with similar electrode configuration is operated below the injection power of a few watts [10].

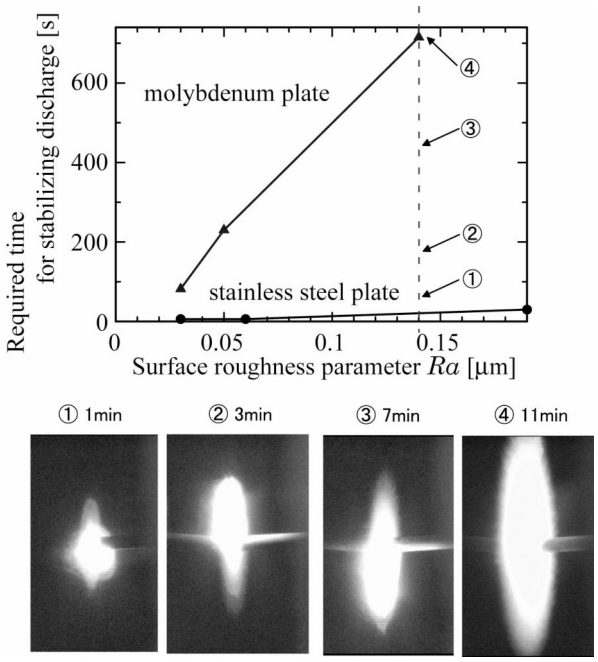

Fig.7 Operation time required for stabilizing discharge.

The surface roughness of the flat panel cathode also affects the stability of the transient glow discharge. When a flat plate cathode has the rough surface, the glow discharge transits easily to arc at the beginning of the discharge. The discharge is gradually stabilized as a certain time has elapsed from the beginning. Finally, the stable transient glow discharge is established. Fig.7 shows the required elapsed time on the surface roughness parameter R_a for the discharge with the cathodes made of molybdenum or stainless steel. R_a is calculated by averaging roughness-height from a mean centerline of surface profile. The temporal change in the discharge using the molybdenum cathode during the stabilization process is shown as a set of the CCD photographs. The exposure timing is indicated in the figure. The discharge with the stainless steel cathode develops into stable glow in shorter time than that with molybdenum one owing to the difference of the melting point. The rough cathode surface has melted because it is heated by the unstable discharges before the glow-to-arc transition. Consequently, it becomes smooth surface and the stable glow discharge is formed. It takes longer time for molybdenum cathode having high-melting point material to melt and to become smooth surface.

V. Effect of The Driving Voltage Waveform

As described in the former section, the use of the flat plate cathode makes it possible to sustain the long duration transient glow discharge and to establish high average injection power. From the viewpoint of the industrial applications, however, the cathodes with a variety of shapes are required according to their aims. To obtain transient APGD keeping the injection energy high regardless of the electrode shape, we proposed a high voltage pulse train driving technique, in which successive pulses with short duration are applied between the electrodes.

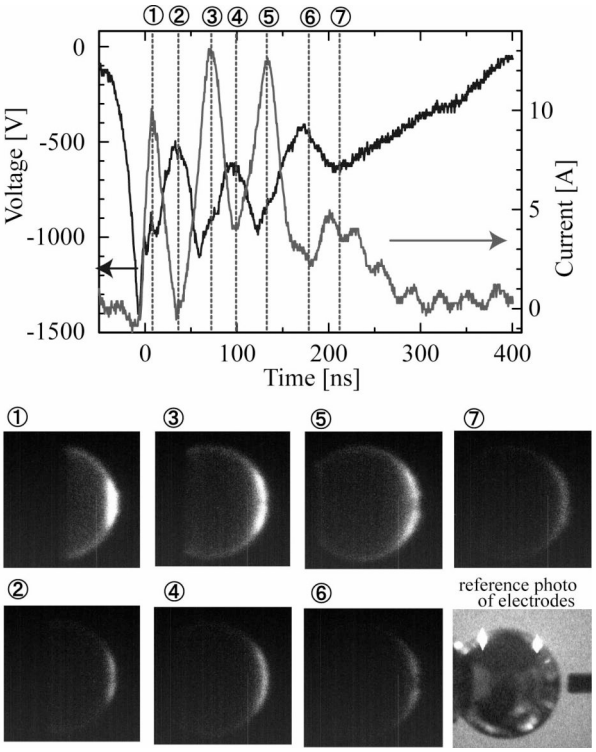

Fig.8 ICCD photographs and the voltage and the current waveforms of the transient glow discharge powered by the pulse train.

The stability of the glow discharge powered by the pulsed applied voltages is improved utilizing highly repetitive operation because of the effect of residual charged particles and/or excited state atoms and molecules in discharge space. When the microdischarges with the fast miniature gas flow, however, the residential time of the gas between the electrodes is so short that no effect to stabilize the discharge is expected with the repetition rate of 1-5kHz. In this study, the residential time of the helium is estimated to be 1.2-6.0μs for the flow rate of 100sccm, and the repetition frequency of over 1MHz is required. It is difficult to realize such a high-repetitive operation using conventional semiconductor power devices as switching

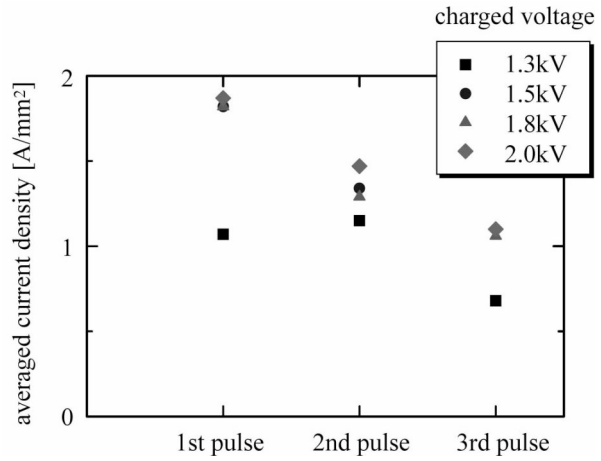

Fig.9 The average current density of the transient glow discharge.

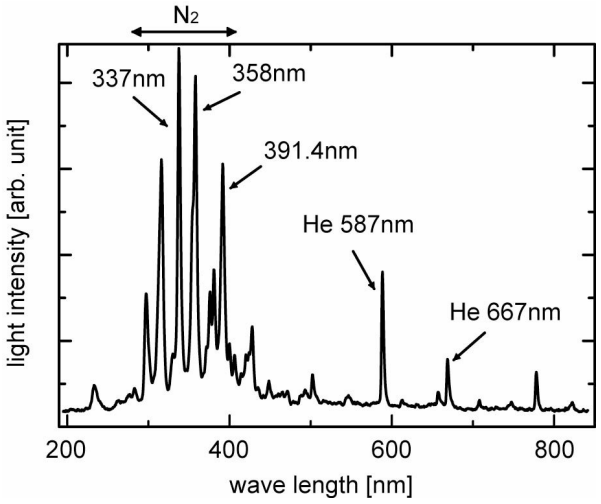

Fig.10 Time-integrated spectra of the transient glow microplasma.

devices. In addition, thermal instability may be induced for the continuous operation because of excess average input power.

Utilizing the newly designed pulse generator with the NLTL, the high voltage pulse train is easily obtained from the single rectangular input pulse. The equivalent frequency of the pulse train is calculated as 12.5MHz from the interval of each pulse. The regulation of the average injection power is made by simply adjusting the repetition frequency of generating the rectangular input pulse.

Fig.8 is a set of the ICCD photographs and the gap voltage and the current waveforms for the transient glow discharge powered by the high voltage pulse train. The exposure time of the ICCD is 10ns and the timing of the each frame is indicated as the frame number in the

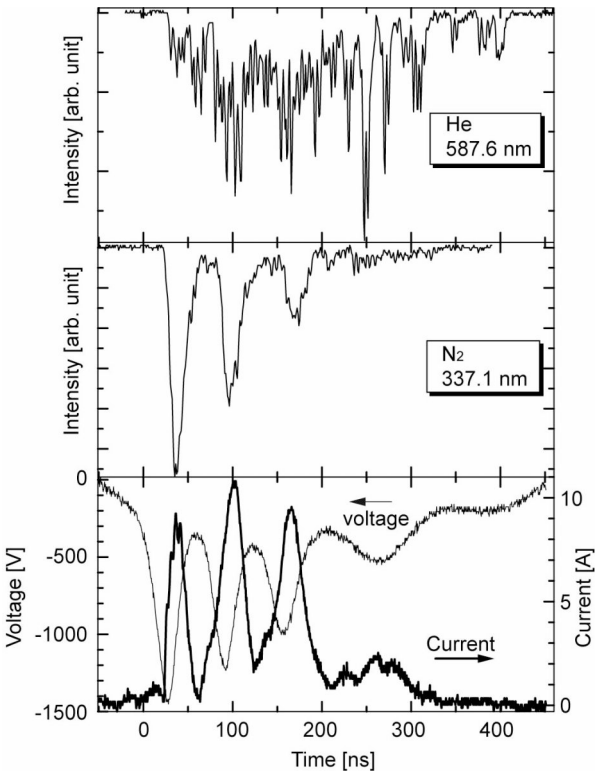

Fig.11 Temporal behavior of the helium atomic spectrum of 587.6nm and the second positive system (SPS) of nitrogen molecule (337.1nm).

waveforms. The successive four transient glow discharges are appeared during the period of the pulse train. The emission intensity of the negative glow region of later phase decreases while the emission area expands. Assuming the axisymmetric discharge structure, the current density of the first, the second and the third pulse is characterized by the discharge current and the area of the emission. The calculated current density is plotted in Fig.9. The current density decreases with the order of the pulses. This indicates that the effect of highly repetitive operation is successfully obtained by driving with the fast pulse train although the residential time of the gas in the discharge gap is less than several micro seconds.

To investigate the discharge development process, optical emission spectroscopy was carried out. Fig.10 shows the time-integrated spectra of the transient glow microplasma. Although the pure helium was fed into the microgap electrodes, strong emission spectra of the nitrogen molecule appeared and showed that the nitrogen contributed significantly to the discharge process. Fig.11 is a set of temporal behavior of the helium atomic spectrum of 587.6nm and the second positive system (SPS) of nitrogen molecule (337.1nm). The change in intensity of

Table 1 Probability of the glow-to-arc transition.

	Probability of glow-to-arc transition			
Rep. Rate	150Hz	250Hz	500Hz	650Hz
without NLTL	100%	100%	100%	100%
with NLTL	12.9%	3.2%	12.9%	3.2%

the SPS spectrum is synchronized with that of the discharge current oscillation. On the other hand, the helium line intensity gradually increases with the time. These results suggested that the helium in the excited state has enough long lifetime to enhance the discharge stability with highly repetitive operation. In order to confirm the advantage of generation of the transient APGDs powered by the high-voltage pulse train, the probability of the glow-to-arc transition was characterized by extracting random sample of thirty pulses from repetitive discharges. The results are summarized in Table 1. The burst pulses generated by the NLTL remarkably suppressed the glow-to-arc transition.

VI. Summary

The stability of the transient glow discharge in the microgap electrodes with the miniature helium gas flow was investigated experimentally. The cathode shapes highly affected the duration of the transient glow discharge. The flat plate cathode with a smooth surface was suitable to extend the sustaining duration of the transient glow discharge and to establish high injection energy. The novel driving technique with high voltage pulse train was also examined. The burst pulse generator with the NLTL was developed utilizing chip monolithic ceramic capacitors as nonlinear capacitive elements. The pulse train driving technique suppressed the glow-to-arc transition successfully.

Acknowledgements

This work was supported by a Grant-in-Aid for Scientific Research from the Ministry of Education, Culture, Sports, Science and Technology: Scientific Research on Priority Areas.

References

[1] M. Kogoma, T. Nozaki, K. Okazaki and Y. Sawada: “Applications of Atmospheric Pressure Glow Plasma,” J. Plasma Fusion Res., 79 (2003) 1009-1028 (in Japanese)

[2] S Kanazawa, M Kogoma, T Moriwaki and S Okazaki: ”Stable glow plasma at atmospheric pressure,"”J. Phys. D: Appl. Phys., 21 (1988) 838--840

[3] K. Takaki, M. Hosokawa, T. Sasaki, S. Mukaigawa and T. Fujiwara: “Production of atmospheric-pressure glow discharge in nitrogen using needle-array electrode,” Appl. Phys. Lett., 86 (2005)

[4] J. J. Shi and M. G. Kong: “Large-volume and low-frequency atmospheric glow discharges without dielectric barrier,” Appl. Phys. Lett., 86 (2005)

[5] T. Ichiki, R. Taura and Y. Horiike: “Localized and ultrahigh-rate etching of silicon wafers using atmospheric-pressure microplasma jets,” J. Appl. Phys., 95 (2004) 35-39

[6] E. Stoffels, A. J. Flikweert, W. W. Stoffels and G. M. W. Kroesen: “Plasma needle: a non-destructive atmospheric plasma source for fine surface treatment of (bio)materials,” Plasma Sources Sci. Technol., 11 (2002) 383--388

[7] C. Schrader, P. Sichler, L. Baars-Hibbe, N. Lucas, A. Schenk, S. Draeger, K. H. Gericke and S. Buttgenbach: “Micro-structured electrode arrays: Plasma based sterilization and coating over a wide pressure range,” Surface & Coatings Technol., 200 (2005) 655-659

[8] K. H. Becker, K. H. Schoenbach and J. G. Eden: “Microplasmas and applications,” J. Phys. D: Appl. Phys., 39 (2006) R55-R70

[9] K. H. Schoenbach, A. E. Habachi, W. Shi & M. Ciocca: “High-pressure hollow cathode discharges,” Plasma Sources Sci. Technol., 6 (1997) 468-477

[10] T. Yokoyama, S. Hamada, S. Ibuka, K. Yasuoka, and S. Ishii: “Atmospheric dc discharges with miniature gas flow as microplasma generation method”, J. Phys. D: Appl. Phys., 38 (2005) 1684-1689.

[11] S. Ibuka, R. Mikami, F. Furuya, K. Ogura, K. Yasuoka, and S. Ishii: “Generation of Atmospheric Pressure Transient Glow Discharge in Microgap Electrode with Nanosecond Pulsed Voltage”, IEEJ Trans. on Fundamental Materials, 127 (2007) (in print)

[12] S. Ibuka, K. Abe, T. Miyazawa, A. Ishii and S. Ishii: “Fast High-Voltage Pulse Generator with Nonlinear Transmission Line for High Repetition Rate Operation,” IEEE Trans. on Plasma Science, 25 (1997) 266-271

GENERATION OF MICROPLASMAS USING ELECTROLYTE CATHODE AT ATMOSPHERIC PRESSURE

N.Shirai*, K.Matsui, S.Ibuka, K.Yasuoka, and S.Ishii

Department of Electrical and Electronic Engineering
Tokyo Institute of Technology
2-12-1-S3-9 O-okayama, Meguro-ku, Tokyo, Japan

Abstract

We discuss two schemes to generate microplasmas using electrolyte cathodes in air. One is atmospheric glow discharge by direct current operation in air with the combination of an electrolyte cathode and a miniature gas flow system. Electrical discharges are operated in a nozzle-to-electrolyte electrode system where a gas with a small volume is placed in open space. Using miniature gas flow, stable glow discharges are generated with the electrolyte cathode. The other is negative corona discharge generated at the tip of Taylor cone. The Taylor cone is formed at the surface of liquid having viscosity, electrical conductivity, and moderated surface tension. Negative corona discharges develop in air at the tip of the Taylor cone or at the filament growing from there.

I. Introduction

Microplasmas are generated by electrical discharges between electrodes in which a material with a small volume is placed. Gases are commonly used as a material to generate the microplasmas. However, dense microplasmas are useful for practical applications. They are generated easily using liquid, whose density is higher than that of gases. We reported previously to use a droplet [1] or a liquid filament [2] as the initial material of microplasmas. We observed that the discharge process developing from droplet to plasma is more complicated than that from gases. Plasmas are widely used in chemistry where chemical reactions often progress in the liquid phase. The additional energy can be supplied to the reactions in the liquid phase by electrical discharges. Non-thermal reactions assisted by high-energy electrons are also expected. Consequently, one needs more deep understandings of electrical discharges in the mixed phase of gases and liquid. The discharge with liquid specimens is often used to analytical techniques. Liquid is used as not only initial matter of plasmas but also discharge electrodes. Atmospheric dc glow discharges with electrolyte cathodes were reported fifty years ago[3]. The electrolyte cathode atmospheric discharges are used for the analytical techniques and the surface treatment to obtain functional materials[4][5].

In this paper, we discuss two new schemes of generating microplasma using liquid cathodes. One is an electrolyte cathode atmospheric dc discharge using miniature gas flow. We already reported microplasmas generated by dc discharges with a miniature gas flow in a stainless-steel nozzle-to-mesh electrode system[6]. When the liquid electrolyte cathode replaced the mesh cathode, we can generate the microplasmas similar to those using the mesh cathode. Physics of microplasmas with electrolyte cathode has not been clearly understood yet. However, they are suitable for the application of microfabrication processes, because a variety of electrolyte solution will be used as liquid cathode. Therefore their applications extend further in the field of plasma processing and plasma chemistry. The other is microdischarge using the liquid cone, which is called Taylor cone and is formed by electro static force from the surface of liquid with a small volume. When the electro static force is increased, liquid filament grows from

the tip of the cone toward a counter electrode. Pulsed discharges of ethanol filament was operated to generate microplasmas[2]. When we used electrolyte ethanol solution to obtain Taylor cone having electrical conductivity, negative coronas appeared at the tip of the cone. The corona develops only when the solution is used as cathode. In this case, the Taylor cone is similar to a needle cathode. Although the deposited energy to the corona is small, the corona with the liquid needle cathode is advantageous to plasma processes because the atoms and molecules evaporating from the liquid surface flow into the corona region, in which non-thermal electron collisions are frequent. Therefore, the corona discharge at the tip of the liquid cone is a candidate for achieving highly functional microplasma reactors.

II. Experimental

Fig.1 is a schematic of the experimental setup with an electrode system for electrolyte cathode glow discharges. A working gas, helium or argon, was fed in open air through the stainless steel nozzle with an inner diameter of 200μm and an outer diameter of 350μm. A gas flow rate was varied in the range from 50 to 140sccm using a mass flow controller. The stainless steel nozzle is used as anode and is located above the liquid surface that is cathode. The liquid used is sodium sulfate solution or distilled water. The conductivity of the liquid electrode is 1-4000μS. We mainly used electrolyte cathode with the conductivity of approximately 1700μS/cm.

The gas flow makes the liquid surface being hollow curve inwards. A steel plate was also used as cathode to examine the dependence of the discharge on gas flow pattern, which varied according to the shape of surface. The electrode separation was varied from 100 to 1000μm. The liquid electrolyte electrode was connected to the ground potential via a 100Ω resistor. The discharge was powered by a regulated dc power supply. A ballast resistor 1MΩ was connected in series to the nozzle anode. The discharge current was measured by recording the voltage across the 100Ω resistor. The gap voltage was measured using a high voltage probe. The visible light images of the discharge were obtained from a charge coupled device (CCD) camera with an exposure time of 30ms.

Fig2 is an experimental setup for negative corona discharges with an electrolyte cone cathode, which is formed at the end of the stainless steel nozzle with an inner diameter of 1mm and an outer diameter of 1.5mm.

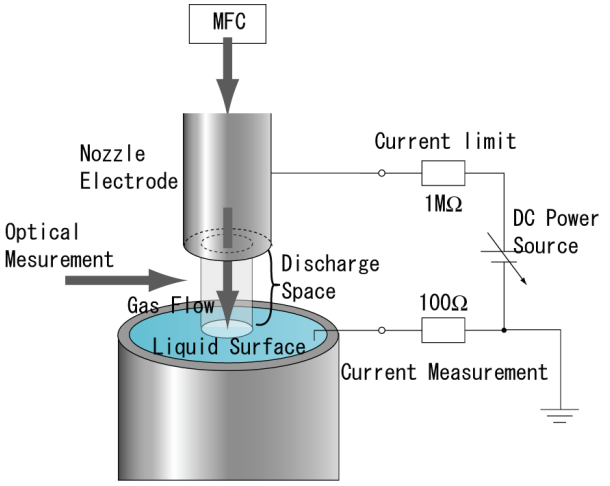

Fig.1. Experimental setup for electrolyte cathode glow discharge using miniature gas flow.

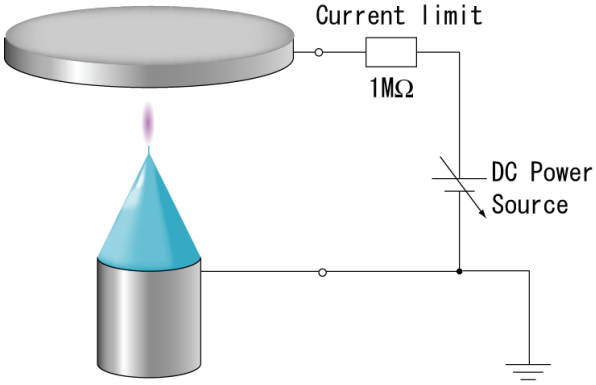

Fig.2. Experimental setup for negative corona at the tip of the Taylor cone.

The anode is a flat plate made of stainless steel. PVA solution or electrolyte ethanol solution was used to form Taylor cone. PVA solution has conductivity and higher viscosity than pure ethanol. The electrode separation was varied from 5 to 10mm. When the applied dc voltage was ncreased, Taylor cone was formed and then corona discharges appeared.

III. Results and Discussion

Glow discharge using electrolyte cathode

Fig.3 is a set of photographs of stable glow discharges in air using the sodium sulfate solution cathode and the miniature helium gas flow. The feature of glow discharge, namely, cathode glow, Faraday dark space, and positive column is clearly observed. When the electrode separation was varied from 100 to 700μm, the length of the positive column increased linearly. This is a specific characteristic

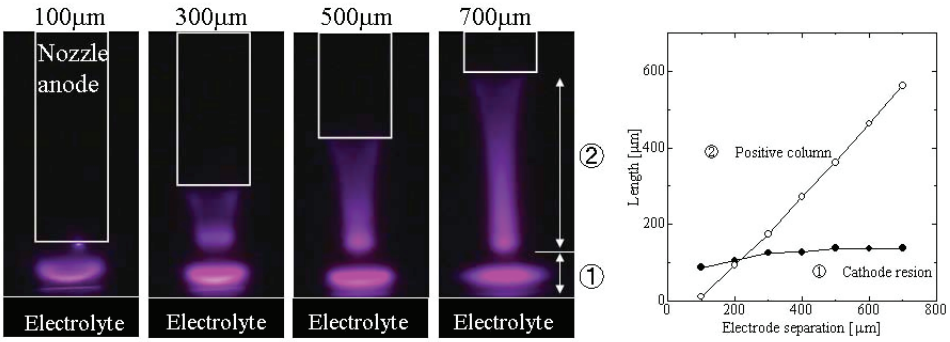

Fig.3.Photograph of the electrolyte cathode glow discharge using miniature gas flow at various electrode separation.

of the low-pressure glow discharges. The electrolyte cathode discharges are generated even if there is no gas flow. They, however, were less stable and the feature of glow discharge was not observed clearly.

We observed two discharge modes in the dc discharges with the miniature gas flow and the electrolyte cathode. They are a pulsed mode and a continuous mode, whose typical temporal changes in gap voltage and discharge current are shown in Fig.4. The temporal changes are affected also by the kind of liquid. These modes were observed in the previous results in atmospheric dc discharge with the miniature helium flow [6].

Fig.5 is the current-voltage characteristics for the discharges with the electrode separation ranging from 200 to 700μm. The discharge current was 0.5-10mA. The gap voltages for the electrolyte cathode discharge are higher than those for the metal cathode one. Fig.6 shows the gap voltage dependence on the electrode separation. It increased with increasing the electrode separation. Fig.7 is the cathode fall voltages obtained from the results in Fig.6. They increase with increasing the discharge current in the range of less than 4mA and become constant when the current exceeds 4mA. The cathode fall voltages for the electrolyte cathode are higher than those for the metal cathode, because the phenomena at the plasma-electrolyte interface in ELCAD are more complex than those at the plasma-metal interface.

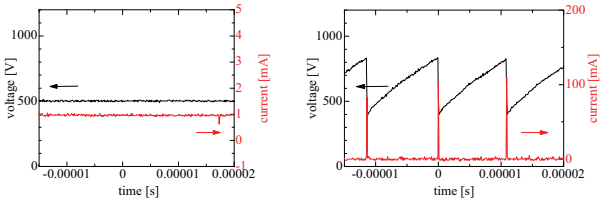

(a) (b)

Fig.4. Two mode of dc discharge (a) continuous mode (b) pulsed mode

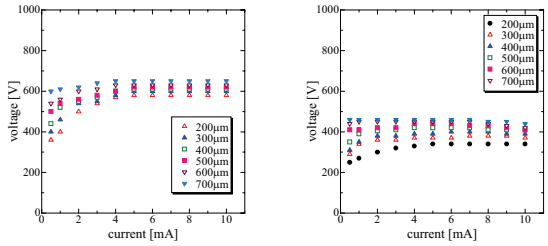

(a) electrolyte cathode (b) metal cathode

Fig.5. Current-voltage characteristics at different electrodes

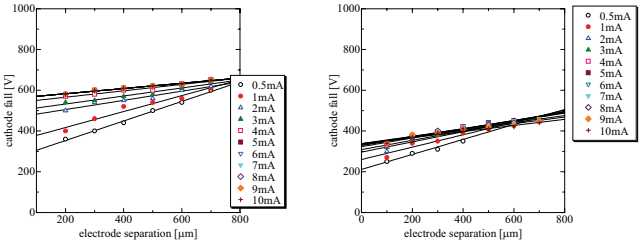

(a) electrolyte cathode (b) metal cathode

Fig.6. Gap voltages as a function of electrode distance

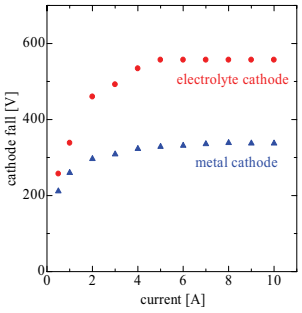

Fig.7. Cathode fall voltage

To clarify the cathode fall physics in ELCAD, we used an AC power supply to generate electrolyte cathode discharges, in which the polarity of the electrolyte electrode was changed alternately. When a positive voltage was applied during a half-cycle of the sinusoidal wave, the

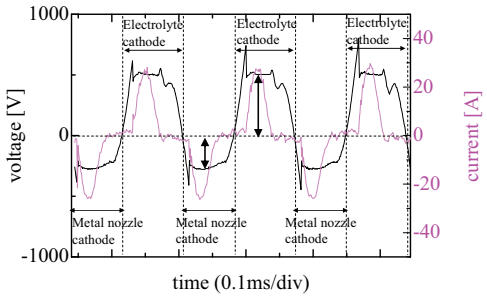

(a) metal nozzle to electrolyte electrode system

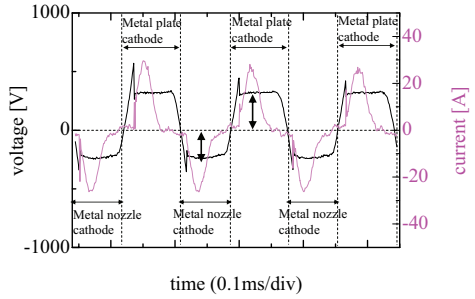

(b) metal nozzle to metal plate electrode system

Fig.8. Temporal changes in voltage using AC power supply

electrolyte electrode acted as cathode. It acted as anode during the next half-cycle. Fig.8 is the temporal change in the gap voltage and the discharge current for the discharges using the electrolyte and the metal electrodes. A significant difference is the gap voltages for the electrolyte electrode discharge, which shows the asymmetry of them for positive and negative applied voltages. The voltage for the electrolyte cathode is higher than that for the metal cathode. These differences are attributed to both the electron and vapor emission from the cathode surface. The equivalent resistance of the electrolyte is negligible in the circuit. These results show that the discharges with electrolyte cathode are affected by the surface phenomena such as sputtering, secondary emission, and evaporation of electrolyte

Negative corona discharge at the tip of the Taylor cone

Corona discharges develop in the vicinity of the tip of Taylor cone. It is easily formed at the surface of ethanol of which surface tension is low. Conductivity of ethanol, however, is also so low that the corona discharge does not

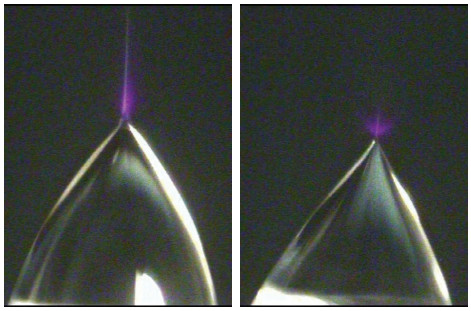

(a) jet mode (b) spray mode

Fig.9. Negative corona at the tip of Taylor cone of ethanol-electrolyte solution

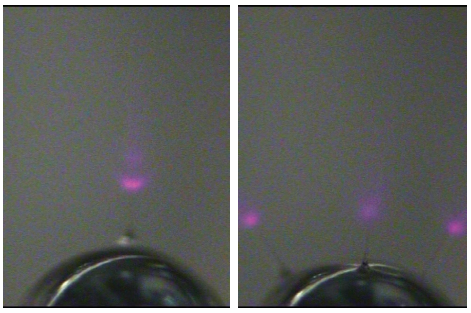

(a) single mode (b) multi mode

Fig.10. Negative corona at the tip of Taylor cone of PVA solution

appears. Taylor cone is hardly formed using water or electrolyte, which has high surface tension. Therefore liquids having conductivity, moderate viscosity, and low surface tension are applicable to generate both Taylor cone and corona discharges. To realize this, we used ethanol with low concentration sodium sulfate solution.

Fig.9. shows the negative corona discharges at the tip of Taylor cone using the ethanol with sodium sulfate solution of which conductivity is 180μS/cm, where the electrode separation is 7mm and the applied voltage is 5kV. The corona discharge appears only when the ethanol is operated as a cathode. When the ethanol is operated as an anode, the corona does not develop and the breakdown easily progresses to spark discharge. The visible light intensity of negative corona increased with increasing the conductivity of liquid. This is because the operating mechanism of coronas at the tip of Taylor cone is different from that of coronas using metal electrode. As seen in ELCADs, the effect of liquid electrode appeared when liquid is used as cathode. We observed two modes of the

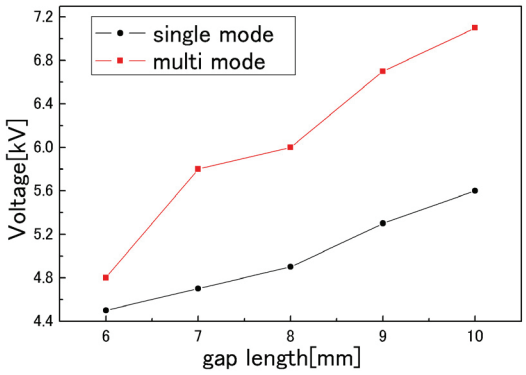

Fig.11. the lowest voltages which need for generating single and multi mode.

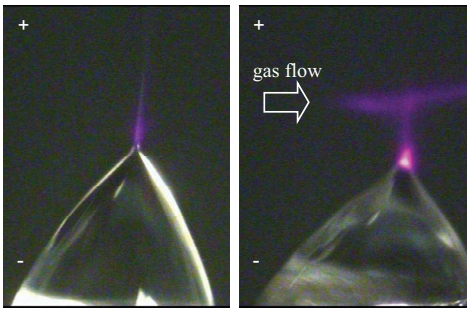

Fig.12. Corona discharge at the tip of Taylor cone applying helium in cross-flow

negative corona discharge, namely, a jet mode and a spray one, which appeared alternately. The height of the cone having the negative corona increased with time in the spray mode, which had brush-like emission. It suddenly switched to become the jet mode, of which emission extended along the filament protruding from the tip of the cone. After then, the height of the cone gradually decreased. These processes repeated with the period of approximately 1-2seconds.

The corona discharges with jet and spray modes are unstable because the vapor generated in the spray mode diffuses out. To avoid the diffusion, we use PVA solution, which has higher viscosity. The surface of it became to be hemisphere as shown in Fig.10. In (a), a single filament was formed on the surface of the PVA solution and the corona discharge appeared at the position of 0.7-1.0mm apart from the tip of the cone along the filament. When the applied voltage was increased, the number of filaments increased as shown in (b). The multi filaments repelled each other and showed random motion on the surface of the solution. Although multi mode is unstable, we may enable to drive in parallel. Fig.11. is the minimum voltages for the appearance of the single and multi modes. Although deposited energy to the corona discharges is small, the corona at the tip of the cone is advantageous to plasma processes because the atoms and molecules evaporating from the liquid surface flow into the discharge and are collided with radicals and charged particles. Therefore, the corona with the conductive liquid is a candidate of highly functional micro plasma reactors.

When a miniature helium flow was fed vertically to the corona that developed along the ethanol solution, light emission along the gas flow, of which position was at 50-500μm from the tip of cone, was observed as shown in fig.12. Although the mechanism of light emission is not explained yet, the scheme has a possibility as a new plasma reactor for micro plasma-processing because the combination of gas and liquid makes a variety of chemical reactions possible.

IV. Conclusion

We reported two schemes of generating microplasmas using liquid cathodes.

One is atmospheric glow discharge powered by direct current in open air with the combination of an electrolyte cathode and the miniature gas flow system. Stable glow discharges are generated on the electrolyte cathode surface by using miniature helium flow. The cathode fall voltage is substantially higher than that for metal cathodes. This is because the operating mechanism of ELCAD plasma-solution interface is different from that of the plasma using metal cathode.

The other is negative corona discharge generated at the tip of Taylor cone. Moderate viscosity and low surface tension of liquid are necessary for Taylor cone to be formed. Using the ethanol with sodium sulfate solution or PVA solution which has conductivity, corona discharge develops at the tip of the cone. The corona appears only when the solution is operated as cathode. Feeding helium as a cross-flow into the corona, light emission along the gas flow, of which position is at 50-500μm apart from the tip of cone, is observed.

Microplasma using liquid and miniature gas flow is a candidate for highly functional micro plasma reactors because a variety of chemical reactions progress in the combination of gas and liquid.

Acknowledgements

This work was supported by a Grant-in-Aid for Scientific Research from the Ministry of Education, Culture, Sports,

Science and Technology: Scientific Research on Priority Areas.

References

[1] N. Shirai, Y. Onaka, S. Ibuka, K. Yasuoka & S. Ishii: “Generation of microplasma using pulsed discharge of ethanol droplet in air”, Jpn.J.Appl.Phys. 46 (2007) 370-374.

[2] Y. Onaka, N. Shirai, N. Nakagawara, S. Ibuka, K. Yasuoka, S. Ihsii: The paper of Technical Meeting on Plasma Science and Technology, IEEE Japan PST-05-99 (2005) (in Japanese)

[3] R. Davies & A. Hickling: “Glow-discharge electrolysis. Part I. The anodic formation of hydrogen peroxide in inert electrolytes”, J.Chem.Soc. (1952) 3595-3602.

[4] T. Cserfalvi, P. Mezei & P. Apai: “Emission studies on glow discharge in atmospheric pressure air using water as a cathode”, J. Phys. D: Appl. Phys., 26 (1993) 2184-2188

[5] V. Titov, V. Rybkin, T. Shikova, T. Ageeva, O. Golubchikov & H. Choi: “Study on the application possibilities of an atmospheric pressure glow discharge with liquid electrolyte cathode for the modification of polymer”, Sur. Coat. Tech. 199 (2005) 231-236

[6] T. Yokoyama, S. Hamada, S. Ibuka, K. Yasuoka, & S. Ishii: “Atmospheric dc discharges with miniature gas flow as microplasma generation method”, J. Phys. D: Appl. Phys., 38 (2005) 1684-1689.

A Study on external magnetic field and power export for high-power magnetron with ETIGO IV

H. Yamazaki , K. Hashimoto, M. Daimon and Weihua Jiang

Extreme Energy-Density Research Institute Nagaoka University of Technology, Nagaoka, Niigata 940-2188, Japan

ABSTRACT

The Magnetron is one of the efficiency high-power microwave source, although the energy conversion efficiency decreases with pulsed-power relativistic electron beam. We study the capability to increase energy conversion efficiency of Relativistic Magnetron. Some recipes become a candidate to enhance efficiency, among them the *Transparent-Cathode* is concise and hopeful procedure. The *Transparent-Cathode* consists of independent cathode strips. It's hope that shorter start-up times and improve operation efficiency. In this work, we head to the target of discovering availability by *Transparent-Cathode*, and make the prototype experimental apparatus with ETIGO IV that is 400kV class repetitive pulsed-power generator. This prototype clarifies some matter and perspective.

1. Introduction

The high-power magnetrons with relativistic electron beam have been studied as one of high-power microwave source [1-2]. The relativistic magnetron has been extrapolated with great success to high-power microwave generator, although the relativistic magnetrons operate within the lower microwave region by comparison other high-frequency generator (e.g. gyrotron). The features of magnetron are high oscillation efficiency and comparatively low demand for external magnetic field. And this means reduction of the device scale and weight are expected. Additionally, the operation frequencies of conventional Magnetrons are in S-band (2-4 GHz) region, in which the attenuation of microwave is a little in atmosphere. It can do efficient transmission. Consequently the Magnetron devices are expected for the electrical power transmission and radar and so on. Especially the electrical power transmission permits the development of the area can't be supplied electricity by wire: e.g. isolated village where electric wire doesn't reach and space development and earth-to-space; for Solar Power Satellite (SPS).

These developments request to enhance combined efficiency [3-4]. Some recipes become a candidate to enhance efficiency: magnetic priming and cathode priming and anode priming and the rest [5], among them the *Transparent-Cathode* is concise and hopeful procedure [6-7]. As against the conventional cathode, which consists of solid

columnar cathode, The *Transparent-Cathode* consists of independent cathode strips. Each cathode strip caused azimuthal magnetic field, and the radial drift velocity of electrons are accelerated more than that of electron emitted from general cathode. Additionally azimuthal electric field penetrates the cathode strips. The crossed field devices like Magnetron generate from the interaction between azimuthal electric motion and electromagnetic wave. So *Transparent Cathode* causes electrons rapid spreading, which means rapid start-up, and the penetrating electric field potentiates more efficiency interaction. Additionally the shorter start-up increases the interaction term in pulsed electron beam, and can enhance the combined efficiency. It's hope that shorter start-up times and improve operation efficiency.

In this work, we head to the target of discovering availability by *Transparent Cathode*, and make the prototype experimental apparatus with ETIGO IV that is 400kV class repetitive pulsed-power generator. This prototype experiment clarifies some matter and perspective. These details are as follows.

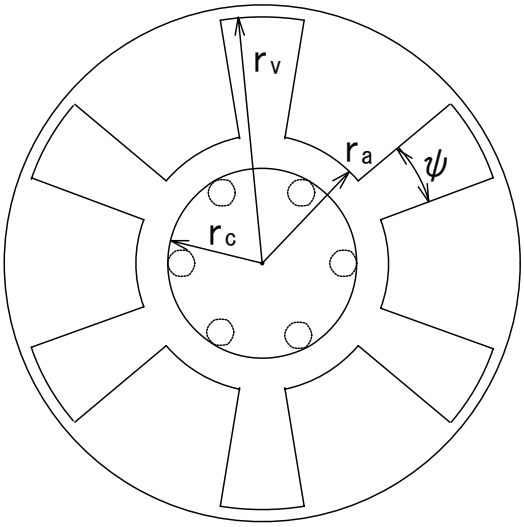

Fig.1 The schematic of magnetron

2. Design criteria

The cross section diagram of conventional magnetron is shown in Fig.1. The magnetron comprises the cylindrical anode enclosing coaxial cylindrical cathode. The anode has the spaces as resonator vans. The electrons are emitted by the central cathode are subjected axial magnetic field B_z and drift by Lorentz force. The drifting electrons interact in the space between the two electrodes with the characteristic mode from the structure of resonator vans. The characteristic dimensions are designed from type A6 Magnetron, which has studied for relativistic magnetrons. The parameter of A6 magnetron is the radius of cathode r_c=15.8 mm, radius of anode r_a=21.1 mm, the gap of resonator vanes on the side of anode $\psi = 20°$, and the depth of resonator vans r_v=41.1 mm. The number of resonator vans is M=6. The axial length of body is 72 mm, which is decided by the wave length of the operation electromagnetic wave. We assume the fundamental operation mode is π-mode

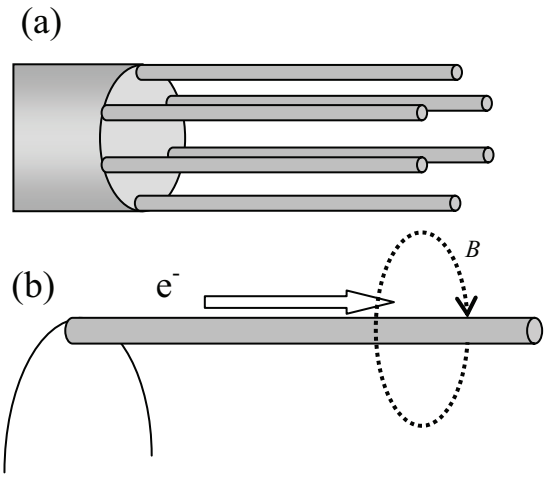

Fig.2 The models of *Transparent cathode*
(a)The transparent cathode consists of independent cathode strips. (b)The magnetic effect of transparent cathode near the strip

(2.34GHz) or 2π-mode (4.6GHz). The operation regions are within S-band to C-band (4-8GHz).

In Fig.1, the broken lines within the conventional cathode line show the *transparent cathode*. The external radius of transparent cathode is same to the radius of conventional magnetron cathode r_c. And the number of strips is same to that of resonator vans *M*. Figure 2 (a) shows The *Transparent cathode* by crosswise direction. The *Transparent cathode* consists of independent and parallel cathode strips, and each live strip caused azimuthal magnetic field shown in Fig.2 (b). The electrons emanated by cathode strips are accelerated by Lorentz force of this azimuthal magnetic field and the motion of impressed electromotive force.

The electron acceleration causes rapid expanding and early electron bunching show up electron spokes. Only the electron spokes can be effective interaction with electromagnetic wave. So the electron acceleration begets the rapid start-up. Additionally, rotation angle electric field penetrates the cathode strips. The presence of a rotating field perturbation facilitates the motion of electrons fall in anode. Magnetrons get out microwave from potential energy of electrons. The stronger fields cause effective interactions, so the new magnetron should improve combined efficiency.

We will use repetitive pulsed-power generator called ETIGOIV, which is capable of delivering, to a matched load, an output pulse of 400 kV in voltage, 13 kA in current, and 130 ns in pulse width, at the repetition rate of 1 Hz. Figure 3 shows the Hull cutoff and Buneman-Hartree resonance conditions [8] for A6 Magnetron. In general, the Hartree voltage is less than the Hall cutoff voltage magnetic insulation. The magnetic field ranges

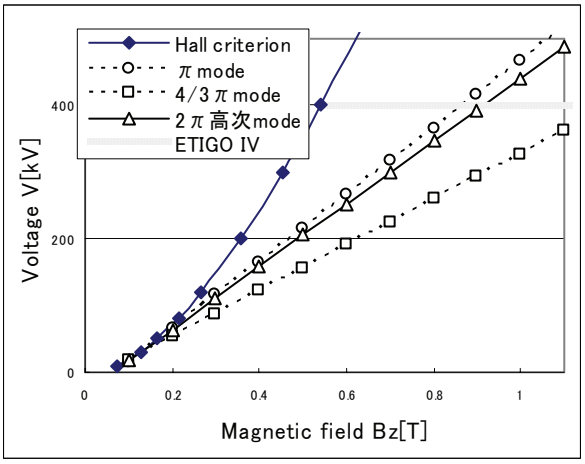

Fig.3 The features of Magnetron operations

from Hull cutoff, at about 0.5 T, where oscillations could not be established. The Hartree voltage is corresponds to the breakdown voltage of magnetron in the presence of a rotating perturbation field. The Hartree voltage, at about 0.9 T, causes the perturbation facilitates the motion of electrons across the cathode-anode gap. The potential energy of the electron efficiently interacts with and provides the electromagnetic wave. On this device, A6 magnetron requires external magnetic field in the range 0.5 T to 1.0 T.

3. Experiment and prospects

The high-power microwave sources has a problem about self-discharge. The axial section of first prototype experiment shown in Fig.4 has flexibility of output horn piping by enclosing Magnetron and output horn. The external magnetic field is caused by Helmholtz type alignment electromagnet. So the magnetic filed influencing to interaction is flat value between two electromagnets, although the peak magnetic field is decreased. In experimental the pulsed external magnetic fields may be a little shielded and delay beyond expectation. The parameters of this vacuum chamber are 3 mm at thickness of outer wall, 177.8

mm in outer wall radius, the distance between magnetron outer radius and chamber wall is 133.25 mm and the material is stainless steel (SUS304). Additionally left-hand side are narrow down and connects to ETIGO IV, as against the right-hand side is open and only covered acrylic board for maintenance and electromagnetic wave output. The delay times at cathode vicinity are about 680 to 720 μs. In proportion to left hand side, the delays are increased. In the case of one-side magnet, the delay times are 220 μs at just inside an electromagnet and 460 μs at cathode vicinity directly above an electromagnet. These points of measurement are draw by diamonds in Fig.4. So we suppose these delays are caused by eddy currents. The theoretical magnetic fields and experimental magnetic fields are shown in Fig.5. The circle dots intend prototype experiment values, and the triangles shown next experiment values. The solid lines intend calculated values, and dashed lines intend experimental value. The magnetic field of experiment in vacuum chamber is reduced about eight out of ten. In this experiment, the both ends of anode are open for reducing troubles, although operation efficiency is degraded. Nevertheless self-discharge is caused in this prototype experiment. The smoothing aluminum anode and cathode are broken down too. On the other hand,

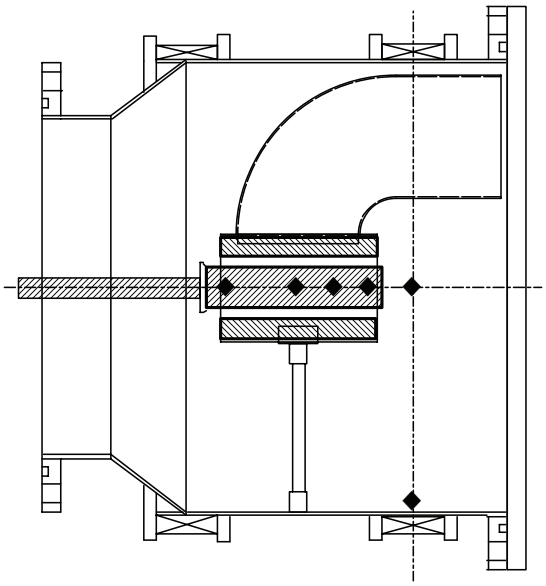

Fig. 4 The axial section of prototype experiment

The shaded area shows anodes and cathode. The output horn bends to right side windows. The external magnetic field consists of Helmholtz coil.

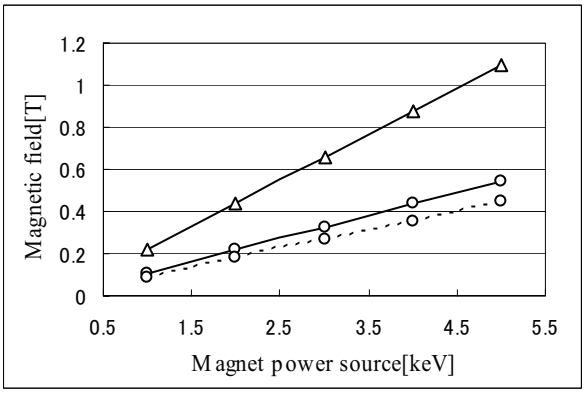

Fig.5 The external magnetic field

Solid lines show calculation values, dashed line show experimental values. The circles indicate prototype apparatus. The triangles indicate next apparatus.

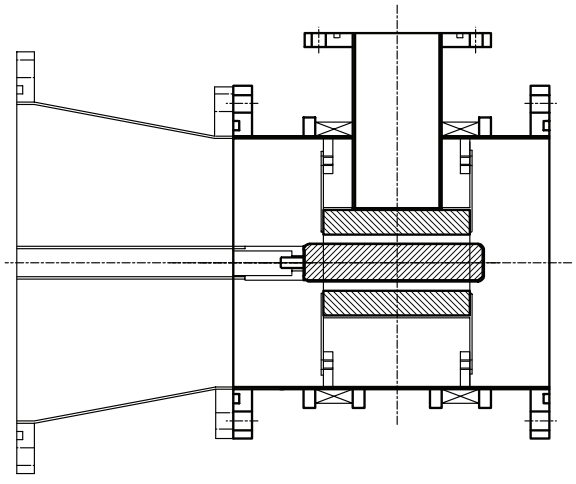

Fig. 6 The axial section of ensuing experiment

The output wave guide penetrate vacuum chamber. The external magnetic field consists of Helmholtz coil.

the large distance between anode and cathode case; expand 5 mm to 8mm, we suppressed breaking down, although this cathode emits beam to axial direction. The next new cathodes are made by graphite for suppression secondary electron emission. Additionally we enhance experimental magnetic field and make new chamber shown in Fig.6. This chamber compress electromagnet radius, although the output waveguide penetrate vacuum chamber. The magnetic field in this new chamber shows in Fig. 5 by triangle dots and solid line. The axial electron beam emissions hit to metal chamber wall in new experiment. We perceive some problems in prototype experiment. The next experiment suppresses these troubles coming into prototype. The transparent cathode can enhance magnetron efficiency with minimum change from conventional magnetron. In the immediate future, the characteristics of magnetron with transparent cathode are observed, and they will contribute to increasing efficiency of relativistic magnetron.

Reference

1) J. Benford and J. Swegle, "High-Power Microwaves", Artech House, Norwood, MA, 1992

2) S.H. Gold and G.S. Nusinovich, "Review of high power microwave source research", Rev. Sci. Instrum., Vol. 68, No. 11, pp.3945-3974, 1997

3) A. Palevsky and G. Bekefi, "Microwave emission from pulsed, relativistic *e*-beam diodes. II. The multiresonator magnetron", Phys. Fluids, Vol. 22, No. 5, pp.986-996, 1979

4) R.W. Lemke, T.C. Genoni and T.A. Spencer, "Three-dimensional particle-in-cell simulation study of a relativistic magnetron", Phys. Plasmas, Vol. 6, No. 2, pp.603-613, 1999

5) V. Bogdam, C. Jones, R.M. Gilgenbach, Y.Y. Lau, J.W. Luginsland, B.W. Hoff, M.White, N.M. Jordan, P. Pengvanich, Y. Hidaka and H.L. Bosman, "Magnetic Priming Effects on Noise, Startup, and Mode Competition in Magnetron", IEEE Trans. plasma, Vol. 33, No. 1, pp.94-102, 2005

6) Michael C. Jones, V. Bogdom Neculaes, William M. White, Y.Y. Lau, Ronald M. Gilgenbach, John W. Luginsland, P. Pengvanich, N. M. Jordan, Y. Hidaka and Herman L. Bosman, "Simulations of Magnetic Priming in a Relativistic Magnetron", IEEE transactions on electron devices **52**, pp.858-863, 2005

7) M. Fuks, A. Andreev, H. Bosman, S.Prasad, and E.Schamiloglu, "Prospective Applications of the Transparent Cathode in Crossed-Field Microwave Oscillators", Department of Electrical & Computer Engineering, University of New Mexico, USA, 2006

8) R.V. Lovelace, T.F.T. Young, "Relativistic Hartree condition for magnetrons: Theory and comparison with experiments", Phys. Fluids **28**, pp.2450-2452, 1985

Conversion of 5 GHz high power microwave to Gaussian beam with quasi optical antenna.

Tomoaki KURIHARA, Masatoshi OHBAYASHI, Ritoku ANDO
Graduate School of Natural Science & Technology, Kanazawa University

Kakuma Kanazawa-City 920-1192 , Japan
Email to kurihara@plasma.s.kanazawa-u.ac.jp

ABSTRACT

A quasi optical antenna called Vlasov antenna, is effective and it is usually utilized to gyrotron for launching microwave output power from the oscillators to free space. It can make linear polarized most simple mode, TEM_{00} in free space, Gaussian beam. Simple geometrical optics is utilized in the design. And several shapes are investigated experimentally. The best efficiency is 41 % in experiment. The conversion efficiency can be improved by increasing the step-cut length, and by increasing radius of circular waveguide.

Ⅰ. Introduction

High power microwave (HPM) is categorized into continuous wave (CW) or pulse. Some applications (fusion reactor, high power accelerator, and so on) need higher output powers; therefore, CW oscillators have been developed. Especially gyrotron achieved MW-level output power. It works well to transfer electric power to far place. And also it is effective in plasma production. On the other hand, output power of pulse operated oscillators is achieved to GW-level. The electric field is so strong that discharge in atmospheric pressure is possible. In addition, irradiating the pulse HPM to dielectric materials in vacuum, it is able to cause the surface discharge on dielectric materials. [(1)] Hence we think that it is able to cause more moderate ablation in larger area than laser. Especially for the application to space generation of ultra short pulse HPM and propagation of it. Especially we will discuss the result of conversion from output of BWO (TM_{01} mode) into Gaussian beam (TEM_{00} mode).

Ⅱ. Microwave source

2.1 Backward wave oscillator

High power microwave oscillator has been developed by us under the collaboration with N. S. Ginzburg, *et al*. The operating frequency is chosen at S-band (around 5 GHz). Because the wavelength is rather long, ～ 6 cm, the components become moderate size for handmade. We choused backward wave oscillator (BWO). BWO is composed with a corrugated circular waveguide section named by slow wave structure (SWS). SWS resonates with an electron beam. Microwave generated at SWS propagates to

upstream direction at first, and is reflected at the reflecting area. And it goes through SWS again, is radiated to free space from the end. The external magnetic field is not necessary in the operation in principle. But we must apply a magnetic field so that an electron beam goes straight. In this experiment, the applied magnetic field was 1.1 T.

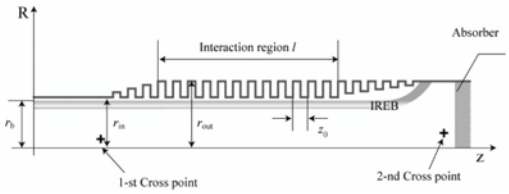

Fig.1. Structure of BWO in the simulation.

2.2 Intense relativistic electron beam

An intense relativistic electron beam (IREB) is powerful energy source of HPM. Anyhow oscillation of HPM needs high power electron beam, and IREB is better suited for it. IREB, which is a short pulse beam, has energy from several hundred keV to several MeV and current above 1 kA. However, electron density of IREB is so high that an uniformity of electron energy gets worse. What resolves this problem is superradiance. It enables us to get a single frequency without relation to beam quality. The energy converted to microwave through bunching of the beam. In the optimum condition efficiency becomes 50 % and above.

2.3 Superradiance

Pulse operation of BWO with pulse IREB enables to generate ultra short pulse microwave. Here the pulse duration, because it has a range of the most suitable value. Superradiance was made a suggestion by N. S. Ginzburg. [3] It is a transitive phenomenon, and provides us with the double output at the maximum in comparison with CW. Figure.2 shows radiation frequency obtained by simulation. It is assumed that a very sharp oscillation peak is provided around 5 GHz. In this case the peak power of microwave is approximately 35% of the max power of IREB. Being based the simulation, K. Kamada and others achieved an oscillation of 300 MW, 5GHz and TM_{01} mode. In this time, the energy efficiency is 12 %. [4]

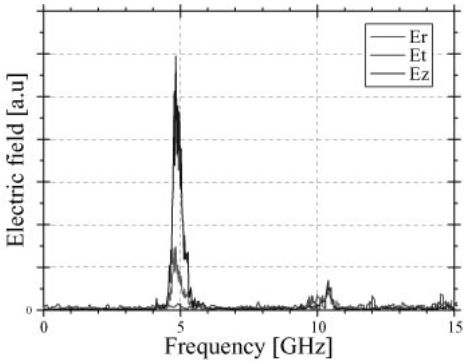

Fig.2. Frequency spectrum of BWO by the simulation.

2.4 Discharge on the acrylic window

We usually decrease power density by increasing waveguide radius before output window with horn antenna. Setting an acrylic window at the end of waveguide without horn antenna, the discharge was occurred on the vacuumed side of window. On the acrylic window, many thin electric discharge traces are observed in a radial pattern. These traces are the directions of the electric field of TM_{01} mode as seen in Figure 3.

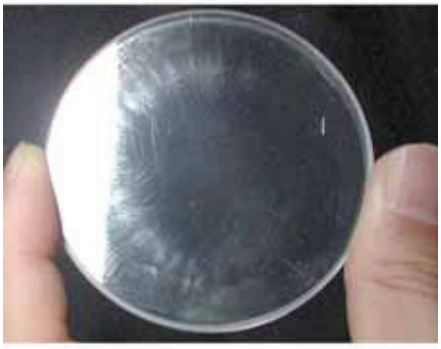

Fig.3. Damage on the surface of acrylic window.

Ⅲ. Mode converter

3.1 Quasi optical antenna

A quasi optical antenna named Vlasov antenna launches the microwave in TM_{01} mode from the oscillator to free space in Gaussian beam, TEM_{00}. The antenna which is applied to gyrotron works at much higher frequency typically, [5] and the wavelength is less than one centimeter. Also the operating mode is TE mode, which is different from BWO. The efficiency is high, 80 %. [6] The antenna can converts TM and TE mode in circular waveguide into a linearly-polarized mode. Quasi optical antenna is consisting of a step-cut waveguide and a cylindrical parabolic mirror (Fig.4). "Step-cut waveguide" is a circular waveguide for transmission of which we cut half plane at the end. The focal points of the reflector are aligned along the axis of the step-cut waveguide.

3.2 Design by geometrical optics

Now we describe how each comportments works. At the first we explain about a step-cut waveguide. Propagating microwave in a waveguide is assumed to be a plane wave. In circular waveguide, the relation between wavelength in waveguide and one in free space is given by

$$\left(\frac{2\pi}{\lambda_0}\right)^2 = \left(\frac{2\pi}{\lambda_z}\right)^2 + \left(\frac{\xi_{n,m}}{a}\right) \quad . \quad \cdots\cdots(1)$$

The λ_0 is wavelength in waveguide, and λ_z is one in free space. "*a*" is radius of waveguide. The $\zeta_{n,m}$ is the *m*th solution of Bessel function $J_{n(x)}$. In the case of TM_{01} mode, $\zeta_{0,1}$ is 2.40. In addition, eq.(1) changes to next relation given by

$$k_0^2 = k_z^2 + k_\perp^2 \quad , \quad \cdots\cdots(2)$$

where $k_\perp$ is the wave number in vertical direction $k_\perp = (\xi_{n,m} / a)$. Thus emission angle α is given by

$$\alpha = \sin^{-1}\left(\frac{k_\perp}{k_0}\right) = \frac{\lambda_0 \xi_{n,m}}{2\pi a} \quad . \quad \cdots\cdots(3)$$

Microwave mode in circular waveguide is treated as standing wave on the cross sectional plane of waveguide. Consequently two waves bouncing

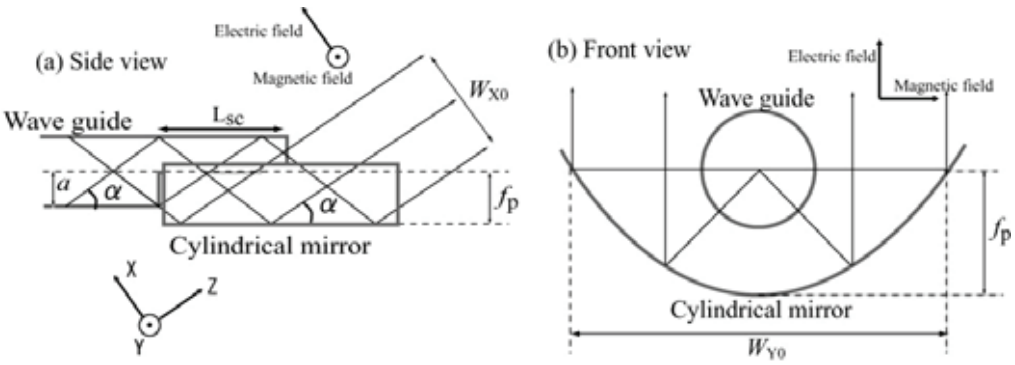

Fig.4 Quasi optical antenna.

between the two walls have negative and positive $k_{\perp}$. The two waves go across each other, which have the same amplitude, wave length and α for being satisfied in boundary condition.

When the waveguide is cut off perpendicularly, two waves go straight keeping the two angles of ± α. In the front view, microwave is emitted from the axis of the waveguide with axis symmetry. Using the step-cut waveguide, the radiation can be send to the parabolic reflector at all. After being reflected at the parabolic reflector, the wave front become to plane wave at the focus.

In the side view, one ray comes out directly and the other that is reflected at the upper side. These two rays are merged, and the width of the ray becomes twice. Figure 5 shows the phase fronts in the propagation. It is satisfied in both TE and TM mode. The electric field and magnetic field are replaced for TE and TM modes. The planes of polarization of waves launched from antenna are rotated 90 degrees between the two modes.

We take the *Z*-axis in the direction of beam propagation. The *X*-axis is taken to be perpendicular to *Z*-axis and in the normal plane of the reflector. And *Y*-axis is taken to be perpendicular to *X*-axis and *Z*-axis. For TM mode, the electric field is polarized to *X*-direction, and the magnetic field to *Y*-direction.

Thinking geodetically, an aperture of quasi-optical antenna is given by following relations.

$$W_x = 4a\cos\alpha \qquad \cdots\cdots(4)$$
$$W_y = 4f_p$$

Here f_p is a focal length of a parabolic mirror. According to eq.(4), the size of the aperture is decided only a and f_p.

The L_{sc} is the step-cut length. If L_{sc} is too short, microwave is not able to be reflected at the upper side. But if too long, output ray is interrupted by the upper side. Thus L_{sc} must have appropriate length, which is within next range,

$$\frac{2\alpha}{\tan\alpha} < L_{sc} < \frac{2f_p}{\tan\alpha} \qquad . \quad \cdots\cdots(5)$$

3.3 Gaussian beam

Microwave converted into linear polarization is able to be treated as Gaussian beam. Gaussian beam has a parameter named "spot size", which is a radius that electric field become 1/*e*, the power does $1/e^2$. Focusing ray, spot size has a minimum value at some place. The place is called "beam waist", at which wave front becomes in the flat, and microwave is converted into linear polarization completely. It is influence of diffraction; spot size varies along to propagation. Spot size is often treated as beam radius, and we

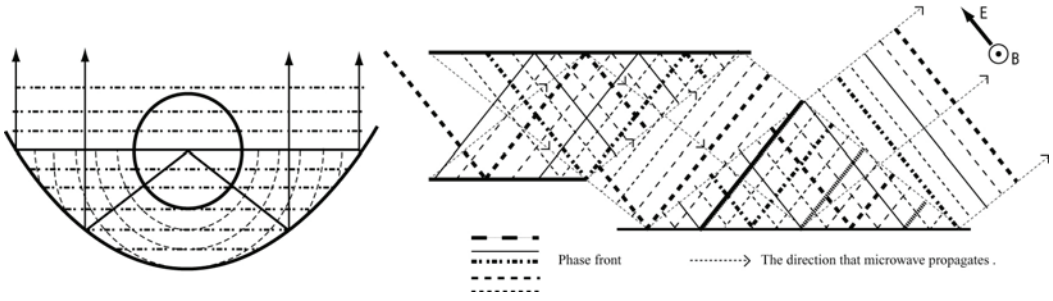

Fig.5 Propagation of microwave in the quasi-optical antenna.

can write next relation about it. [7]

$$\omega_{(z)} = \omega_0 \left[1 + \left(\frac{\lambda z}{\pi \omega_0}\right)^2\right]^{1/2} \quad \cdots\cdots(6)$$

The $\omega_{(z)}$ is spot size after z propagation, and ω_0 is a minimum size at beam waist. Using this relation, we can calculate the spot size after propagation by ω_0 easily. Additionally, when $z >> \omega_0$, we can rewrite eq.(6) to next relation,

$$\omega_{(z)} = \frac{\lambda z}{\pi \omega_0} \quad .\cdots\cdots(7)$$

The $\omega_{(z)}$ is the size that power becomes to e^{-2}, therefore, we can write the following relation about power density.

$$I(x, y) = \frac{2P_0}{\pi \omega_x \omega_y} \exp\left(-\frac{2x^2}{\omega_x}\right) \exp\left(-\frac{2y^2}{\omega_y^2}\right) \quad \cdots\cdots(8)$$

Here, $I_{(x,y)}$ is the power density at the coordinates, P_0 is the total power, ω_x and ω_y are the spot sizes of each directions. On the beam axis (Z-axis), it is assumed that $x = y = 0$, and (8) is able to be rewritten that

$$P_0 = \frac{I_0}{2} \pi \omega_x \omega_y \quad . \cdots\cdots(9)$$

According to eq.(9), we can calculate the total power of Gaussian beam by the power density and spot sizes.

By the way, we assumed that microwave is converted into linear polarization at the focal plane of reflector previously. It is assume that the focal point of reflector is the position of a beam waist (Z=0). The minimum spot sizes in X and Y direction at beam waist were supposed geometrically. We can write next relations about the quasi optical antenna.

$$\omega_{x0} = \frac{W_{x0}}{2} = 2a \cos\alpha, \quad \omega_{y0} = \frac{W_{y0}}{2} = 2f_p \quad \cdots\cdots(10) .$$

In this time we chose the four types of step-cut waveguides. They were two different radius waveguides (a = 3.0 cm, 3.6 cm), and four different L_{sc}. Thinking geometrically, conversion efficiency doesn't depend on the radius of waveguide (ω_0 depends on radius), and quasi optical antenna is supposed to work independent of L_{sc}. But 5 GHz microwave, which we used in this time, has much longer wavelength than millimeter-wave, it was possibility that the antenna was under influence of diffraction. For this reason, we made four types of step-cut waveguides. We show the sizes of antennas and spot sizes at Z = 0 cm (beam waist), 50 cm, 75 cm, 100 cm (Table 1).

Table 1. Sizes of quasi optical antennas and the calculated spot sizes.

Type	**Ⅰ**	**Ⅱ**	**Ⅲ**	**Ⅳ**
a	3.0 cm		3.6 cm	
α	49.8 degrees		39.7 degrees	
L_{sc}	5.5 cm	9.5 cm	8.5 cm	14 cm
$2\omega_X \times 2\omega_Y$ (Z = 0 cm)	7.7 cm × 24 cm		11 cm × 24 cm	
Z = 50 cm	50.2 cm × 28.8 cm		36.4 cm × 28.8 cm	
Z = 75 cm	74.8 cm × 33.9 cm		53.2 cm × 33.9 cm	
Z = 100 cm	99.6 cm × 39.9 cm		70.3 cm × 39.9 cm	

Ⅳ. Experiment Ⅰ

4.1 Setting

At first, we measured the total power before the conversion in order to estimate the conversion efficiency. The cone-shaped horn antenna was set in length at the end of BWO, and microwave radiates out to free space.

4.2 Detecting power

We show the detecting power (Fig.6). After entering rectangular waveguide, microwave is

attenuated by attenuator and cable (Fig.7), and at last it is detected by tunnel detector. We checked the frequency with low pass filter (L.P.F). The resolution of L.P.F is limited to 1 GHz; therefore, this measurement is not too strict. However, (Fig.6) shows that the frequency is around 5 GHz. Additionally, the wave form is like to simulation that is showed in previous. Thus we think that microwave oscillate in almost 5 GHz.

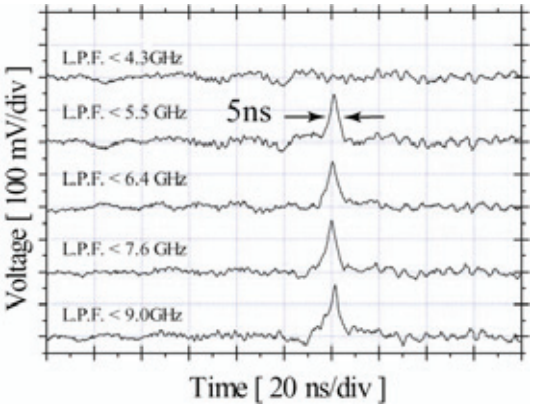

Fig.6. Detected power after passing the L.P.F.

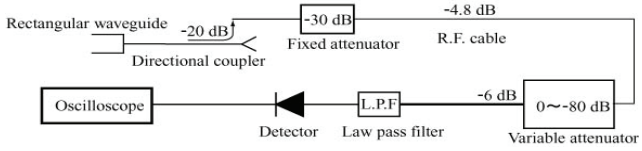

Fig.7. Detecting system.

4.3 Radiation pattern before conversion

Setting the horn antenna for reception to opposite the one for emission, we detected microwave. We could change the angle for the front (Fig.8). The result of measurement is presented in (Fig.9). The power has peak at 25 degree. It is assumed that output power is distributed in the shape of a circle uniformly, we integrated the graph. As a result the total power was about 160 MW.

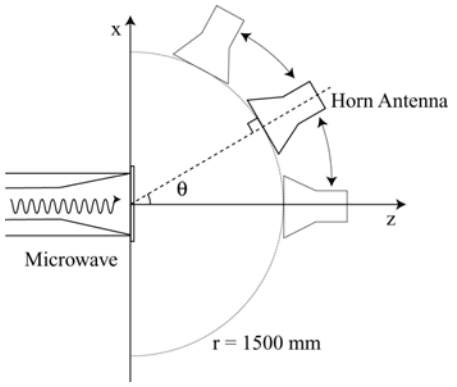

Fig.8. Power measuring method.

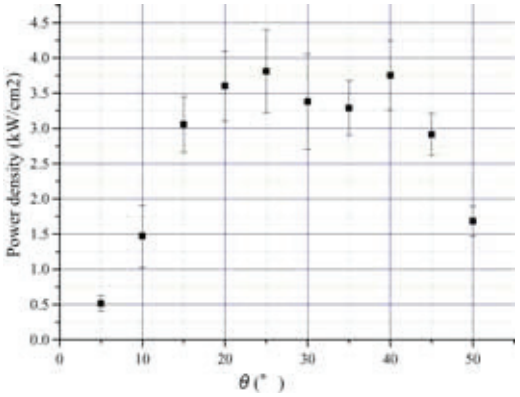

Fig.9. Power density *vs.* radiation angle.

Ⅴ. Experiment Ⅱ

5.1 Setting of quasi optical antenna

Quasi optical antenna was set behind the horn antenna. In this time, the parabolic mirror was set to be perpendicular to the ground. In consequence, the direction of electric field (X-axis) was parallel to ground.

5.2 Measurements of emission patterns with fluorescent tubes

Irradiating a microwave to a fluorescent

tube, it brightens up. The threshold value that a fluorescent tube brightens is about 30 kW/cm^2. And so, arraying fluorescent tubes in the shape of a screen, we observed emission patterns. A fluorescent screen was set at the distance of 50 cm from quasi optical antenna, and was perpendicular to *Z*-axis (Fig.10).

We show the emission pattern Figure.11.

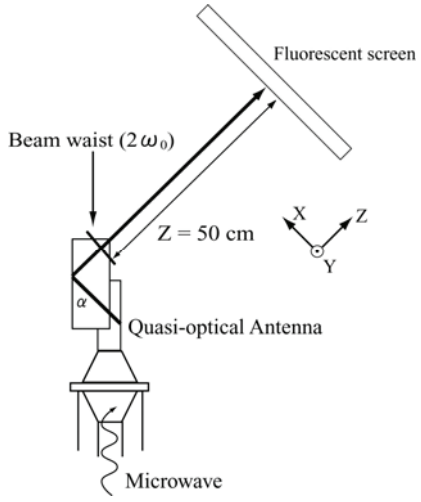

Fig.10. Fluorescent tubes array was set at the distance of 50 cm from quasi optical antenna.

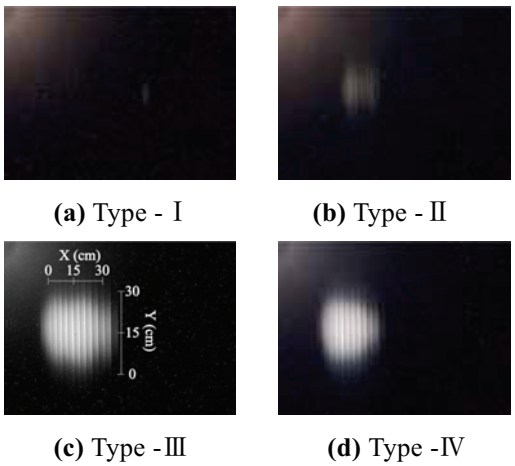

(a) Type - Ⅰ **(b)** Type - Ⅱ

(c) Type -Ⅲ **(d)** Type -Ⅳ

Fig.11. Emission pattern from quasi optical antennas.
Z = 50 cm.

The picture (a)~(d) are corresponding to Type Ⅰ ~ Type Ⅳ in Table 1. The emission patterns whose center shined strongly are enable us to making out that TM_{01} mode was converted into linear polarized mode.

And then, we made forecast that conversion efficiency was not depending on the radius of waveguide and Lsc. Especially it couldn't have been depending on L_{sc}. However, it is evident that the emission patterns were under influence of the radius of waveguide and Lsc. By the comparison of (a) and (c), of (b) and (d), the antenna that had a bigger radius shined more strongly. And by the comparison of (a) and (b), of (c) and (d), the antenna that had a longer L_{sc} flashed more strongly. Hence, it is assumed that the configuration of quasi optical antenna has optimal value.

5.3 Measurements of detecting

We measured the power of Type Ⅳ quasi optical antenna which flashed the screen the most strongly. We used the same detecting system as the previous experiment. We measured it at the distance of *Z*=100 cm. The distributions were measured along *X* and *Y* axis every 5 cm around a peak (Fig.12).

The results of measurements are shown at Figure 13.

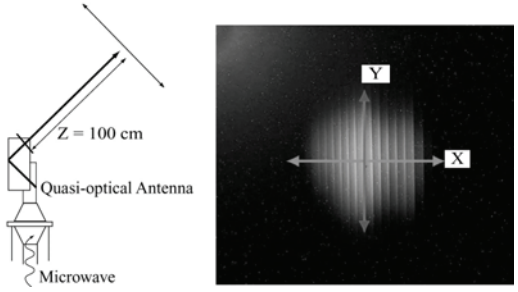

Fig.12. A measurement position and a direction.

To approximate these graphs by eq.(8), ω_x and ω_y were decided. The ω_x was 41.5 cm, ω_y was 23.5 cm. And I_0 was 41 kW/cm^2. To substitute these

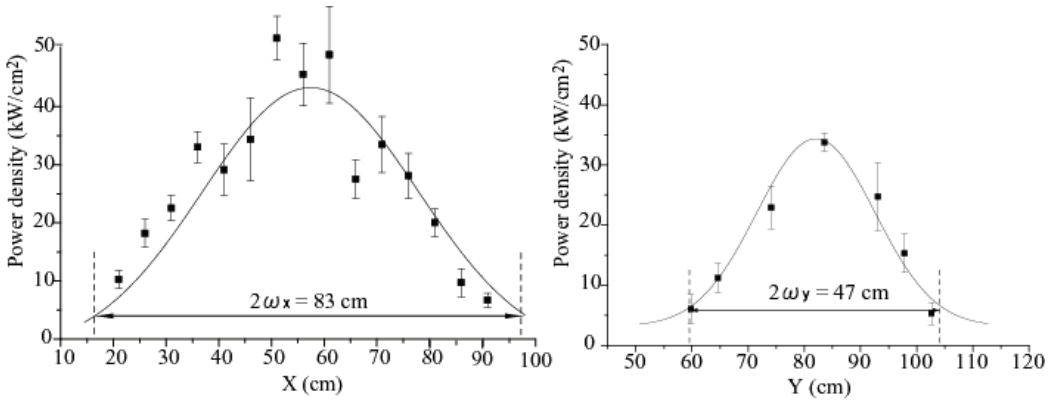

Fig.13. Distributions of power.

parameters to eq.(9), the total power after conversion was about 65 MW. By the comparison of output from horn antenna and quasi optical antenna, the conversion efficiency was 41 %.

VI. Conclusions

Our preliminary result was reported here. We have being continuing to advance the studies of the oscillator and the quasi optical antenna for increasing the output power in Gaussian beam. And we'll study the application of microwave (ablation, plasma production, and so on) for future.

References

(1) M. P. Brizhinev, S .V. Golubev, D. S. Dorozhkina, B. G. Eremin, V. G. Zorin, A. G. Livak, I. V. Plotnikov,S. V. Razin, V. E. Semenov, A. V. Strikovskii, and O. N. Tolkachev : "Microwave discharge in Vacuum on a dielectric surface", Journal of Experimental and theoretical physics, Vol.92, No.6, pp.1137-1142 (2001)

(2) N. S. Ginzburg, N. Yu. Novozhilova, I. V. Zotova, A. S. Sergeev, and N. Yu. Peskov : "Generation of powerful subnanosecond microwave pulses by intense electron bunches moving in a periodic backward wave structure in the superradiative regime." Physical Review, Vol.60, No.3, pp. 3297- 3303 (1999)

(3) N. S. Ginzburg, I. V. Zotova : "Nonlinear-theory of superradiance of moving layer of excited cyclotron oscillators." Sov. Tech Phys. Lett., 15, pp. 573 - 574 (1989)

(4) K. Kamada, K. Yamamoto, R. Nakajima, R. Ando, I. V. Zotova, R. M. Rozental, A. S. Sergeev, and N. S. Ginzburg: "S-band superradiance in slow wave structure", Proceeding of The 6th International Workshop on Strong microwaves in plasmas. (2004) to be published.

(5) I. Ogawa, T. Idehara, S. Maekawa, W. Kasparek, and G. F. Brand: "Conversion of gyrotron output into a gaussian beam using the far-field." International Journal of Infrared and Millimeter Waves, Vol.20, No.5 ,pp.801-821(1999)

(6) S. N. Vlasov, L. I. Zagryadskaya and M. I. Petelin: "Transformation of a whispering gallery mode, propagating in a circular waveguide, into a beam of waves." Radiofizika, Vol.15, No.12, pp.14-17 (1972)

(7) Otozo Fukumitsu : "Introduction to optical electronics" , in Japanese , ISBN: 978-4785690281, published from *Shoukoudou* (1988)

Evaluation of Pulse Ion Beam Ability in the Middle Energy Plasma Focus for Material Engineering

H.R.Yousefi, Y.Nakata, H.Ito and K.Masugata

Department of Electric and Electronic System Engineering, University of Toyama

Abstract

Ability of middle energy plasma focus device (20 kj) were evaluated for material application. In this technique mono-crystalline silicon were used as target and also for substrate. Amorphous silicon (a-Si) film was deposited on the substrate by 1 and 10 DPF shot. Deposited films have been characterized for their structure by X-ray diffraction (XRD).from the result, a-Si film is successfully deposited at room temperature silicon substrate using 20kj plasma focus device.

Keyword: Plasma focus, Ion beam, thin film deposition, plasma focus application

Introduction

The dense plasma focus (DPF) is a simple and cost effective device that utilizes the self-generated magnetic field to compress the plasma to very high densities (10^{25}–10^{26}m^{-3}) and temperatures (1–2 keV) [1,2]. It is a potential candidate for the generation of highly energetic high fluence (up to Mew) ions, relativistic electrons, X-rays and neutrons [3–8].

A PF consist in a pulsed capacitive discharge between two coaxial electrodes immersed in a vacuum chamber filled with a gas at pressures of the order of 1 mbar until 9. Under appropriate operating conditions, a dense (10^{18}–10^{19}) parts/cm^3, short-lived (10^{-7} s), and high-energy, magnetically compressed plasma (called the focus) is produced at the end of the electrodes, typically 1 μs later with respect to the discharge beginning. During this stage of the discharge, an ion beam with a broad energy range (up to MeV) is emitted from the focus region, and hence an ion implantation process, thin film deposition and surface modification can be expected on a substrate located so as to intercept part of the beam.

Bhuyan et al. [9] have shown that for a 2.2 kJ nitrogen filled plasma focus device with hollow copper anode the energies of accelerated nitrogen ions in ion beam at the height of 5.0 cm from the top of the anode ranges from 7 to 500 keV. Their Faraday cup measurements showed that the ion number density of lower energy ions (≤50 keV) was in excess of 4× 10^{18} m^{-3}, whereas the number density of high energy ion ≥300 keV) was of the order of 5× 10^{17} m^{-3}. Surface

modifications and coating techniques based on the interaction between energetic ion beams or plasma streams with a solid surface are of growing importance. One of the plasma devices potentially suited to perform surface treatment and coating is the plasma focus (PF) device. In fact, in recent years, the use of low energy of these devices for the quoted processes have attracted attention because several experiments have shown good results in amorphization ,thin film deposition, surface modification [10-12].therefore the motivation behind the present work is to evaluation of ability of middle energy plasma focus device for material processes.

Experiment

Our Mather- type plasma focus is energized by a capacitor bank of 44.8 µF/30 kV [13]. In this experiment the anode and cathode were of length 242 and 230mm respectively. The oxygen- free copper inner electrode, with a diameter of 50mm, has a hollow shape at the end to reduce interaction between the electron beam generated from plasma column and the electrode surface. Outer electrode (cathode) is composed of 24 copper rods with diameter 10mm, which forms the shape of a squirrel cage with an inner diameter of 100mm.The experiments were conducted to investigate the ion emission from the hydrogen filled PF device. The multiple faraday-cup (FC) assembly was positioned at different distance from the focus region and different angles (0 degree, is the axis of electrode assembly) with respect to the anode axis at as shown in Fig. 1. The FC was operated in biased ion collector (BIC) mode in our case.

A cup electrode (copper) of inner diameter 26.5 mm and depth 20mm was used as an ion collector and was placed in the grounded shield case.

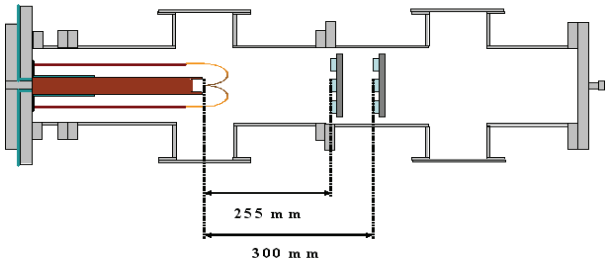

Fig 1.Schematic setup for Faraday-cup measurement

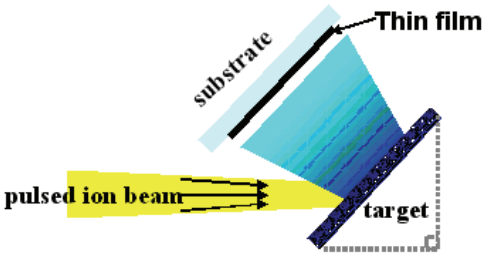

Fig 2.Schematic setup for Silicon deposition

The main part of experiment is amorphous silicon deposition by ion beam. Schematic setup for this experiment was shown in the Fig.2. The specimens used are from high purity, Mirror polished silicon wafer (size 8 · 8 ·0.5 mm^3) with

its surface in (100) orientation. The specimens are cleaned with acetone, methanol to remove the native oxide layer and surface contamination just before their introduction into the plasma focus chamber. The specimens are then mounted axially on the target at the distance of 300mm from the anode and same silicon on the substrate at 10 mm from the target. The films are deposited, at room temperature substrates, using two different numbers of focus shots viz. 1, and 10 at the same condition.

Results

Faraday-cup measurement results in the Fig. 3.indicated that ion current density in center is maximum ant toward the outermost decrease. Most of the ions are emitted in a small solid angle along the anode axis and their flux, generally, decreases with the increasing angle.

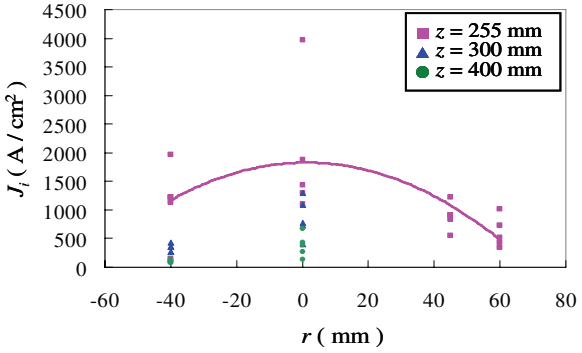

Fig.3.Ion current density in different distance and angle

XRD patterns of films deposited at the distances of 300 mm from the anode at room temperature

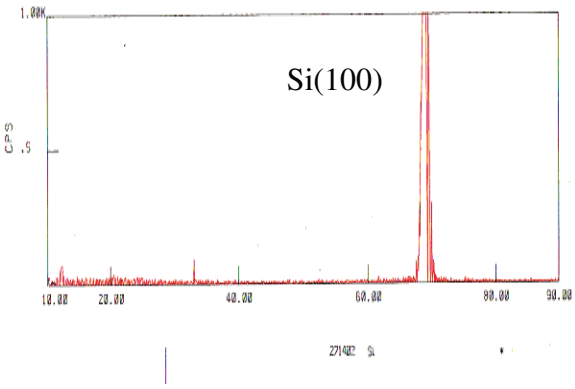

(a)

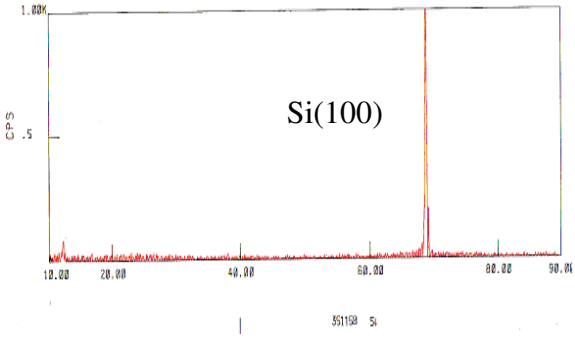

(b)

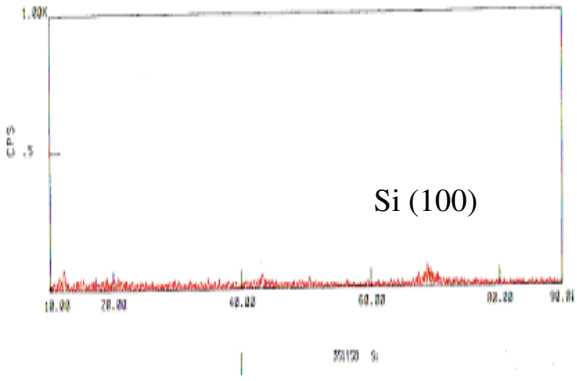

(c)

Fig.4. XRD patterns of films deposited on the Si substrate (XRD is 2Θ and scale is 1.00k). (a) virgin silicon, (b) 1 shot, (c) 10 shot respectively.

are shown in the Fig.4 (a) virgin silicon, (b) 1 shot, (c) 10 shot respectively. At the base is the pattern of untreated sample, which shows a high intensity peak of mono-crystalline silicon. The FWHM of this peak decreases after exposure 1 DPF shot and eventually diminishes with increasing deposited dose. Owing to the fact that a-Si is a highly disordered system without any long range order, the XRD spectrum of sample exposed to 10 DPF shots shows only broad hump rather than any peak-like structures. It is concluded that fine grain size is created by deposition. Successful deposition of a-Si film onto substrates at room temperature has been achieved using 20 kj plasma focus device. Films have been deposited on the mono-crystalline silicon substrate at 1 and 10 DPF shots. It is demonstrated that middle energy plasma focus can be as a pulse ion bema for material engineering processes.

References:

[1] Mather JW, Bottoms PJ. Phys Fluids (1968); 11:611

[2] Lee S, Tou TY, Moo SP, Eissa MA, Gholop AV, et al.Am J Phys(1988);56:62–6.

[3] Takao K, Honda T, Kitamura I, Masugata K. Plasma Sources Sci Technol (2003);12:407–11.

[4] Ahmad R, Hassan M, Murtaza G, Waheed A, Zakaullah M.J Fusion Energy(2003);21:217–20.

[5] Gerdin G, Stygar W, Venneri F. J Appl Phys (1981); 52: 3269–75.

[6] Patran A, Tan LC, Stoenescu D, Rafique MS, Rawat RS, Springham SP, et al. Plasma Sources Sci Technol (2005);14:549–60.

[7] Hussain S, Shafiq M, Ahmad R, Waheed A, Zakaullah M. Plasma Sources Sci Technol (2005);14:61–9.

[8] Zakaullah M, Waheed A, Ahmad S, Zeb S, Hussain S. Plasma Sources Sci Technol (2003);12:443–8.

[9] H. Bhuyan, S.R. Mohanty, T.K. Borathakur, R.S. Rawat, Indian J. Pure Appl. Phys. 39 (2001) 698.

[10] Mehboob S, Ahmad S, Shafiq M, Zakaullah M.Nuclear Instruments and methods in physics research B 252 (2006) 219-224

[11]Rawat R S, Chew W M, Lee P, White T, Lee S.Surface and coating Technology 173 (2003)276-284

[12]Mehboob S, Shafiq M, Waheed A, Ahmad R and Zakaullah M. Physics Letters A, Volume 352, Issues 1-2, (2006), P. 150-154

[13] Yousefi H R, Mohanty S, Nakata Y , Ito H ,Masugata K. Physics of Plasma 13, 114506 (2006).

OBSERVATION OF NEUTRON FLUX PRODUCED IN PLASMA FOCUS

Y. Nakata, T. Mizuno, H. R. Yousefi, I. Kitamura, H. Ito and K. Masugata
Faculty of Engineering, University of Toyama
3190 Gofuku, Toyama, 930-8555, Japan

Abstract

We have performed experimental studies of the neutron emission generated by the Mether-type plasma focus in the pressure range of 200-900 Pa. The main aim of these studies was to determine the neutron emission characteristics, which could enable an approximate settlement of the problem of the neutron emission mechanism. The time-integrated and time-resolved neutron signal and angular distribution anisotropy were measured with two detectors based on a plastic scintillator-photomultiplier combination and silver-activation counter placed at 10 m from the top of the anode. The experimental results show the different influence of thermal and non thermal mechanisms in the nuclear fusion reactions.

1 Introduction

A plasma focus device is recognized as a powerful and excellent source of intense X-rays, neutrons, and beams of ions and electrons. In the plasma focus a high voltage discharge of a capacitor bank is produced through a spark gap switch in a coaxial electrode gun surrounded by a filling gas at a pressure of some hundred Pa. The central electrode is the anode partially covered with a coaxial insulator. The discharge starts over the insulator surface and afterwards the current sheath is magnetically accelerated along the coaxial electrodes. After the current sheath runs over the ends of the electrodes the plasma is compressed in a small cylindrical column (focus), which is a few centimeters long and several millimeters in diameter. Using deuterium gas as the filling gas in the discharge chamber, fusion neutrons from the nuclear reaction (D-D reaction) are emitted in the focus. The emitted neutrons can be applied to perform radiographs and substance analysis, taking advantage of the penetration and activation properties of this neutral radiation.

The problem of a mechanism for the neutron production in pinched plasma discharges is very intriguing, and it still remains unclear. There are two main mechanisms for fusion reactions in plasma focus devices. The first is a thermal mechanism for which the D-D reactions are produced by the thermal collisions between deuterons in the bulk of the plasma focus. The second is the reaction produced by accelerated deuterons colliding with the thermal deuterons in the plasma bulk and/or the neutral gas atoms outside the plasma (beam-target effect). A large number of measurements show that the neutron and electromagnetic radiation emission spectra from plasma focus devices are characterized by a marked anisotropy[1−3]. This fact suggests that nonthermal processes, such as the beam-target effect, may play an important role in the fusion mechanism.

We have performed the recent experiments with the medium energy plasma focus device in order to settle the problem of the neutron emission mechanism. In this paper, we report the dependence of neutron yield on the deuterium filling pressure.

2 Experimental Apparatuse

The plasma focus is composed of plasma focus deice, discharging switch system and power supply. A schematic diagram of a Mather type PF is shown in Fig.1[4]. Plasma focus consists of two coaxial electrodes and a glass insulator between two electrodes. The inner electrode (anode) is a cylindrical oxygen-free copper electrode and its

length and the diameter are 242 mm and 50 mm, respectively. The outer electrode (cathode) consists of 24 oxygen-free copper rods, each of 10 mm in diameter and 230 mm in length. They are distributed symmerically on the cylinder surface of 100 mm in diameter. The insulator is made of glass and the length and the outer diameter are 125 mm and 60 mm, respectively. A capacitor bank of capacitance 44.8 μF, maximum charging voltage 80 kV was used, which was connected to the PF through 224 of coaxial cables. In the experiment the charging voltage of the capacitor bank was fixed to 30 kV. The vacuum chamber was once evacuated to $< 5 \times 10^{-3}$ Pa and after that filling gas was introduced. In the experiment a deuterium gas were used as the filling gas and pressure was adjusted to 200 $\sim$ 900 Pa by a needle valve.

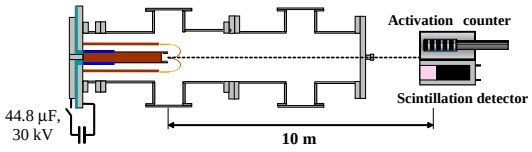

Fig.1 Schematic of the experimental system.

The time-integrated measurement of neutrons was investigated using a silver activation counter located at 10 m from the top of the anode on the axis. Simultaneously, time-resolved measurements of hard x-ray an neutron pulses were performed by means of two scintillator-photomultiplier detectors. The discharge current ($I_{\rm ch}$) was measured by the Rogowski coil.

3 Experimental Results

Discharges were performed in deuterium at different pressures, 200-900 Pa, with a charging voltage of 30 kV, i.e., $\sim$ 20 kJ stored in the capacitor bank. Figure 2 shows typical waveforms of discharge current ($I_{\rm ch}$) measured by a Rogowski coil, and output signal ($V_{\rm SCI}$) measured by a scintillator-photomultiplier detector at $z = 10$ m downstream from the top of the anode on the electrodes axis. As seen in the Fig.2(a), $I_{\rm ch}$ has a peak of 520 kA at $t = 1.7$ μs and after that 120 kA of current dip is observed, which associated with the formation of the strong pinched plasma column. In the figure, $V_{\rm SCI}$ rises sharply at the end of the current dip and has two peaks. Considering the time of flight (TOF) delay between two peaks, we can identify the first peak and the second peak as signals of the hard X-ray and the neutron, respectively. It can be clearly seen from Fig.2(b) that at high pressure the current dip is observed at 0.7 μs after the peak of $I_{\rm ch}$ and after that $V_{\rm SCI}$ rises sharply. Taking as a reference for the $\Delta t = 0$ emission time the maxima of the corresponding hard X-ray pulse, we can estimate the neutron energy from the measured time of flight and convert the neutron pulses into a neutron energy spectrum. In Fig.2 the neutron pulse is observed at around 450 ns after the hard X-ray signal. This delay time corresponds to the time of flight of 2.45 MeV neutrons, which agrees with the neutron energy obtained from the D-D reaction energy balance.

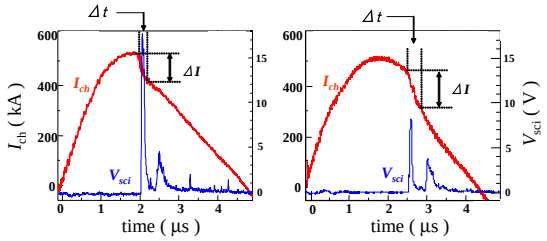

Fig.2 Typical waveforms of discharge current and scintillator signal. Gas pressures are (a) 500 Pa and (b) 800 Pa.

From the current derivative signals the pinch time versus filling pressure can be obtained and it is shown in Fig.3. The pinch compression should be coincident with the peak current in order to achieve the best efficiency. Therefore, the maximum compression of the plasma occurs close to the peak current for pressure of $\sim$ 400 Pa.

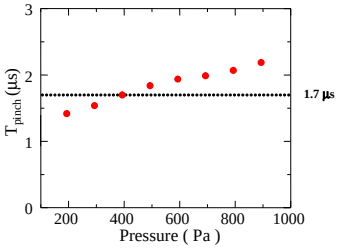

Fig.3 Pinch time vs filling pressure for deuterium.

Figure 4 shows the neutron yield measured by the activation counter as a function of the filling gas pressure. Each point is the average of

five shots and the error bars are the standard deviations. In this device, the optimum pressure for achieving the maximum neutron yield is 700 Pa. This result indicates that the neutron production processes have dependence on the filling gas pressure. We can estimate from the empirical scaling laws available in the literature for drivers with energy in the range 1-100 kJ, $Y = 10^7 E^2$ and $Y = I^{3.3}$ (the storage energy in the driver E in kilojoules and the current pinch I in kiloamperes)[5], since the silver activation counter used in the present experiment has not been calibrated.

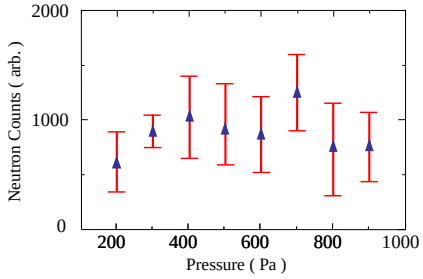

Fig.4 Neutron yield vs deuterium filling pressure.

Figure 5 shows the the angular distribution of the neutron emission. Each point is the average of five shots and the error bars are the standard deviations. It is evident from Fig.5 that the neutron yield tends to decrease with the increase of the angle to the main electrode axis. Similar results have been observed for the neutron intensity measured by two scintillator-photomultiplier detectors located at two different angles (0°, 90°) to the main electrode axis and 10 m from the top of the anode[6]. This result indicates that the neutron production process is attributed to the non-thermal process of the beam beam-target model. The different tendencies of the isotropic and anisotropic contributions seem to be related to the variation of the thermonuclear fusion cross-section and the interaction probablity between the deutron beam and the background gas. From these results, the neutrons are expected to be generated by the combined reactions of thermonuclear fusion and beam-target reaction.

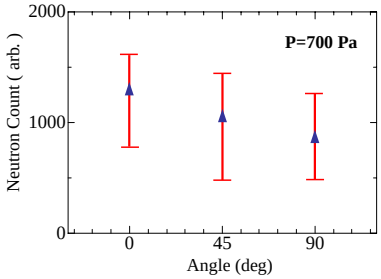

Fig.5 Angular distribution of neutron emission.

4 Summary

The experimental results indicate that two types of mechanisms are present for the neutron production: the thermal effect and the beam-target effect. Both mechanisms can coexist, but seem to be independent of each other.

We plan to carry out the experiment on the neutron emission characteristics to settle the problem of the neutron emission mechanism after the silver activation counter is calibrated. The neutron emission depends on: the electrical parameters of the discharge circuit, on the electrode geometry and on the filling gas pressure. Further investigations on optimal electrodes and insulators size should be undertaken in order to increase the neutron emission.

Acknowledgement

This work is supported in part by the Grant-in-Aid for Scientific Research from the Ministry of Education, Science, Sports and Culture, Japan.

References

[1] J. W. Mather, Phys. Fluid **8**, 366 (1965).

[2] D. E. Potter, Phys. Fluid **14**, 1911 (1971).

[3] U. Jager and H. Herold, Nuc. Fusion **27**, 407 (1987).

[4] K. Takao, T. Honda, I. Kitamura and K. Masugata, Plasma Sources Sci.Technol. **12**, 407 (2003).

[5] S. Lee, *Laser and Plasma Technology*, edited by S. Lee, B. C. Tan, C. S. Wong and A. C. Chew (World Sientific, Singapore, 1985).

[6] H. R. Yousefi, Y. Nakada, H. Ito and K. Masugata, Journal of Fusion Energy **25**, 245 (2006).

EVALUATION OF BIPOLAR PULSE GENERATOR FOR HIGH-PURITY PULSED ION BEAM

H. Ito , I. Kitamura, and K. Masugata
Faculty of Engineering, University of Toyama
3190 Gofuku, Toyama, 930-8555, Japan

Abstract

A new type of pulsed ion beam accelerator named "bipolar pulse accelerator (BPA)"has been proposed in order to improve the purity of intense pulsed ion beams. To confirm the principle of the BPA, we developed a bipolar pulse generator, which consists of a Marx generator and a pulse forming line (PFL) with a rail gap switch on its end. In this article, we report the experimental result of the bipolar pulse and evaluate the electrical characteristics of the bipolar pulse generator. When the bipolar pulse generator was operated at 70 % of the full charge condition of the PFL, the bipolar pulse with the first (-138 kV, 72 ns) and the second pulse (+130 kV, 70 ns) was successfully obtained. The evaluation of the electrical characteristics indicates that the developed generator can produce the bipolar pulse with fast rise time and sharp reversing time. At present the bipolar pulse generator is installed in the B_y type magnetically insulated ion diode and we carry out the experiment on the production of an intense pulsed ion beam by the bipolar pulse accelerator.

1 Introduction

The intensity pulsed heavy ion beam (PHIB) technology has been developed over the last two decades primarily for nuclear fusion and high energy density physics research[1]. Advances in PHIB technology have led us to a number of potential applications of PHIB to surface modification of materials[2−4]. Recently, PHIB technique has received extensive attention as a new ion implantation technology named "pulsed ion beam implantation"to semiconductor materials for the next generation, since the doping process and the surface annealing process can be completed in the same time.

The PHIB can easily be generated in a conventional pulsed power ion diode using a flashboard ion source. The purity of the PHIB, however, is usually deteriorated by absorbed matter on the anode(flashboard) surface and residual gas molecules in the diode chamber. For example, the PHIB produced in a point pinch ion diode contains many kinds of ions including protons, multiply ionized carbons, and organic ions[5,6]. Therefore, the conventional pulsed ion diode is not suitable for the application of the PHIB to the ion implantation. To improve the purity of the intense pulsed ion beam, a new type of pulsed ion beam accelerator named "bipolar pulse accelerator (BPA)"has been proposed[7]. The BPA is an electrostatic two-stage accelerator. As the initial stage of the BPA experiment, a prototype of the experimental system has been developed[8]. The system employs a B_y type magnetically insulated ion diode with an ion source of a coaxial gas puff plasma gun. To confirm the acceleration of the ion beam in the first gap, the ion diode was operated with a single polar negative pulse. The nitrogen ions were successfully accelerated from the grounded anode to the drift tube by applying the negative pulse with a voltage of 240 kV and a pulse duration of 100 ns [full width at half maximum(FWHM)] to the drift tube. The pulsed ion beam with the peak ion current density of 90 A/cm^2 and the beam pulse duration of 50 ns(FWHM) was obtained at 40 mm downstream from the anode surface. In addition, We found from Thomson parabola spectrometer measurement that N^+ and N^{2+} beams with 150-300

keV energy were accelerated with proton impurities of 150-250 keV energy.

As the next stage of the BPA experiment, we have developed a bipolar pulse generator to perform proof of principle experiments on the BPA[9]. The design parameters of the bipolar pulse generator are the negative and positive pulses of voltage ±200 kV with pulse duration of 70 ns each. The developed generator consists of a Marx generator and a pulse forming line (PFL). A multichannel rail gap switch is employed as an output switch of the bipolar pulse. In this article, we present the experimental results of the bipolar pulse and the electrical characteristics of the developed generator.

2 Basic concept of BPA

Figure 1 shows the conceptual diagram of the bipolar pulse accelerator. The proposed BPA consists of a grounded ion source, a drift tube and a grounded cathode. As seen in Fig.1, the BPA is a two-stage accelerator and operated with the bipolar pulse. In the system, a bipolar pulse of voltage $\pm V_0$, duration τ_p each is applied to the drift tube. At first the negative voltage pulse of duration τ_p is applied and ions produced in the grounded ion source are accelerated in the 1st gap toward the drift tube. The polarity of the pulse is reversed at $t = t_1$ and the positive voltage pulse of duration τ_p is applied to the drift tube. As a result, the ions are again accelerated in the 2nd gap toward the grounded cathode and the ion beam experiences total acceleration potential of $2V_0$ in the accelerator. The condition for the most effective acceleration is that the pulse duration τ_p is adjusted to the time of flight delay of the ion to pass through the drift tube, i.e., $\tau_p = L/v_i$, where v_i is the ion velocity in the drift tube and L is the length of the drift tube. This condition can be satisfied by adjusting the parameter of the bipolar pulse and the length of the drift tube. In the above condition, when the top of the ion beam reaches the 2nd gap, the pulse is reversed and the ion beam is accelerated effectively in two gaps. In addition, the merit of the BPA is that the ion source can be installed on the grounded anode, which extremely enhances the accessibility to the anode, while in the conventional PIB diode, the ion source is placed on the anode where the high voltage pulse is applied. This seems to be favorable for an active ion source which is powered by an external power supply.

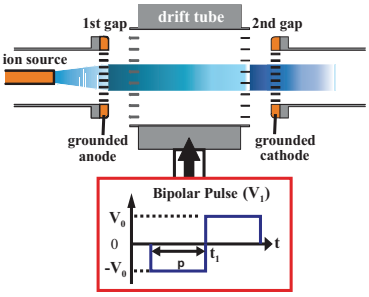

Fig.1 Schematic view of bipolar pulse accelerator.

Figure 2 illustrates the principle of the improvement of the purity of the ion beam. Let us now consider the acceleration of ions in the case that the ion beam produced in the ion source consists of N^+ ion and impurity of H^+ ion. Each ion of N^+ and H^+ is accelerated in the 1st gap toward the drift tube when the negative voltage is applied, where N^+ and H^+ ion beams are schematically described in Fig.2. As seen in Fig.2, the length of H^+ beam is much longer than that of N^+ beam due to the difference of the velocity. We assume that the length of the drift tube is designed to be same as the beam length of N^+ beam with a beam pulse duration τ_p at an acceleration voltage V_0. It is, for example, calculated to be 11.6 cm when $V_0 = 200$ kV and $\tau_p = 70$ ns. On the other hand, the length of H^+ beam at $V_0 = 200$ kV and $\tau_p = 70$ ns is 43.3 cm. When the voltage is reversed and the positive voltage is applied to

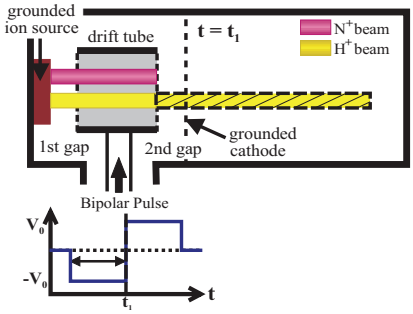

Fig.2 Principle of the improvement of the purity of the ion beam.

the drift tube ($t = t_1$), N^+ beam with the length of 11.6 cm in the drift tube is accelerated in the 2nd gap. In contrast, 73 % of the beam is out of the drift tube and decelerated in the 2nd gap by the first pulse. Hence 73 % of H^+ beam is not accelerated in the 2nd gap by the positive voltage pulse (second pulse) of the bipolar pulse and is removed in the bipolar pulse accelerator. As a result, the purity of the ion beam is improved.

3 Experimental Apparatus

Two types of the pulse forming lines to generate the bipolar pulse have been proposed, i.e., single coaxial type and double coaxial type[10]. The single coaxial type consists of a single coaxial transmission line of length $L_s = v\tau_p$ and two switches which serve as a reversing switch and an output switch, where v is the transmission velocity of the electrical signal on the line. The feature of the line is as follows: (i) simple device and (ii) the ratio of the duration of the negative and positive pulses can be adjusted by changing the trigger timing of two switches. The double coaxial type consists of a double coaxial transmission line and one switch serving as the main output switch and has the following features, (i) the length of the line is short, that is, half of the single coaxial type and (ii) the power loss in the switch is reduced, since single switch is used. In both types, each peak voltage of the bipolar pulse is expected to be half of the charging voltage of the PFL.

Figure 3(a) illustrates the cross-sectional view of the bipolar pulse generator in the present experiment, which consists of basically a Marx generator, a PFL, a transmission line(TL) and a dummy load. The designed output of the bipolar pulse generator is the negative and positive pulses of voltage ±200 kV with pulse duration of 70 ns each. In the present system, the double coaxial type is employed as the PFL for the formation of the bipolar pulse. The line consists of three coaxial cylinders with a rail gap switch on the end of the line, which is connected between the intermediate and outer conductors. The PFL is filled with the deionized water as a dielectric and charged positively by the low inductance Marx generator with maximum output voltage of 300 kV through the intermediate conductor. The waveform of the bipolar pulse is very sensitive to the performance of the rail gap switch, that is, the rise time and the time to reverse the polarity are dependent on the system's inductance including the inductance of the output switch. In order to realize the bipolar pulse with the fast rising and reversing time, the multichannel rail gap switch with an enhanced trigger circuit is utilized as the output switch of low inductance. The detailed structure of the rail gap switch is shown in Fig.3(b). It consists of essentially a trigger electrode and a pair of main electrodes (an inner and an outer electrode of 239 mm^{ϕ} and 261 mm^{ϕ}, respectively) separated by a spacing of 11 mm. The main electrodes are made of iron of 20 mm in thickness and have semicircular cross-section of 20 mm in diameter in the end of the electrodes. The knife edged trigger electrode made of copper is placed between the main electrodes and has diameter of 250 mm at top of the edge. These electrodes are carefully aligned and installed in the acrylic vessel.

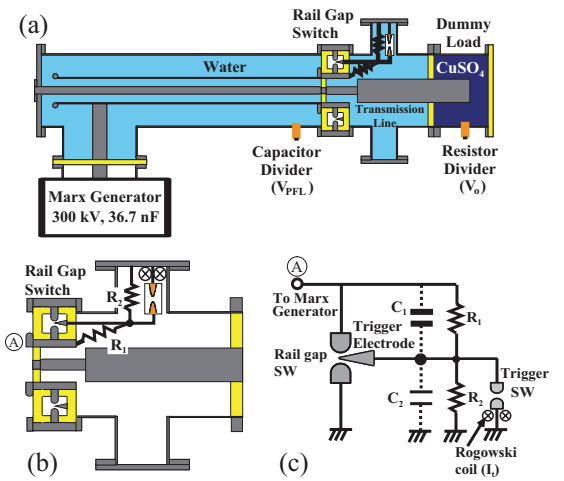

Fig.3 (a) Experimental apparatus, (b) Detailed structure of rail gap switch, (c) Trigger circuit of rail gap switch.

Figure 3(c) shows the circuit of the rail gap switch with the enhanced trigger circuit. The trigger circuit consists of a self-breakdown spark gap switch and two resistors (R_1, R_2) for a voltage divider which is required to eliminate any field en-

hancement in the main gap of the rail gap switch. Here C_1 and C_2 in the figure mean the stray capacitance. The ceramic resistors of 100 Ω are utilized as R_1 and R_2. In the circuit, the point A is connected to the intermediate conductor of the PFL and is kept at the charging voltage of the PFL in the charging phase, whereas the trigger electrode is kept at half of the charging voltage of the line. When charging of the PFL is finished, the spark gap switch is self-broken and the potential of the trigger electrode is dropped to the ground level, which initiates the breakdown of the first gap between the trigger electrode and the inner electrode of the rail gap switch. Subsequently the second gap (between trigger electrode and outer electrode of rail gap switch) breaks down, since the trigger electrode potential swings toward the charging voltage of the PFL. As a result, the rail gap switch is triggered and the bipolar pulse is transmitted to the load. The rail gap switch and the spark gap switch are operated with pure SF_6 gas. The pressure in both switches can be adjusted to control the optimum trigger timing for each experimental condition.

The bipolar pulse voltage (V_0) and charging voltage of the PFL (V_{PFL}) are measured by the resistive voltage divider and capacitive voltage divider placed near the rail gap switch, respectively. The values of V_{PFL} and V_0 are calculated by the ratio factor of the two voltage dividers (K=48500 and 1840, respectively). The Rogowski coil with the coefficient of 614 A/V is applied to measure the current of the trigger switch (see Fig.3(c)).

4 Experimental Results

Figure 4 illustrates the typical waveforms of the charging voltage of the PFL (V_{PFL}), bipolar pulse output (V_0) and current of the trigger SW (I_t) at the charging voltage of 40 kV for the Marx generator in the case of (a) the trigger switch is over pressured not to function as the trigger circuit and (b) the pressure of the trigger switch is optimized to function as the trigger circuit. Here the filling pressure of the rail gap switch is 4.0 atm and the impedance of the dummy load is set at Z_L=7.5 Ω, which is almost same as the characteristic impedance of the line between the inner and intermediate conductors. As seen in Fig.4(a), when the charging voltage of the PFL reaches the peak of 280 kV, the rail gap switch is self-broken at $t \approx 225$ ns and the square bipolar pulse, which consists of the first pulse with a voltage of -138 kV and a pulse duration of 72 ns (FWHM) and the second pulse with a voltage of +130 kV and a pulse duration of 70 ns (FWHM), is successfully obtained. Considering that the output voltage of the Marx generator and the ringing gain of the present system are 240 kV and about 1.2, respectively, the peak voltage of the first pulse (negative pulse) is almost equal to the half of the maximum charging voltage of the PFL as we expected. In contrast the voltage of the second pulse is smaller. The reduction of the voltage in the second pulse seems to be due to the resistance of the rail gap switch. On the other hand, it can be clearly seen from Fig.4(b) that in the triggered operation the bipolar pulse is successfully produced after the breakdown of the rail gap switch is initiated at $t \approx 200$ ns by the trigger with the rise time of about 30 ns.

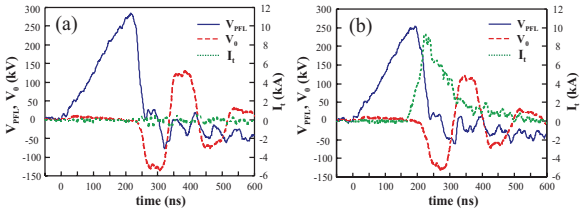

Fig.4 Waveforms of V_{PFL}(solid line), V_0(dashed line) and I_t(dotted line). Rail gap switch is operated in (a) self-breakdown mode and (b) triggered mode.

Figure 5 shows the dependence of the output voltage of the bipolar pulse on the charging voltage of the Marx generator (V_M) at the impedance of the dummy load Z_L=10 Ω. Here the rail gap switch is operated in the self-breakdown mode and the filling pressure of the rail gap switch is adjusted so that the breakdown can be initiated almost at the same time for each condition. It is clearly seen from Fig.5(b) that the output voltage is proportional to the charging voltage of the Marx generator.

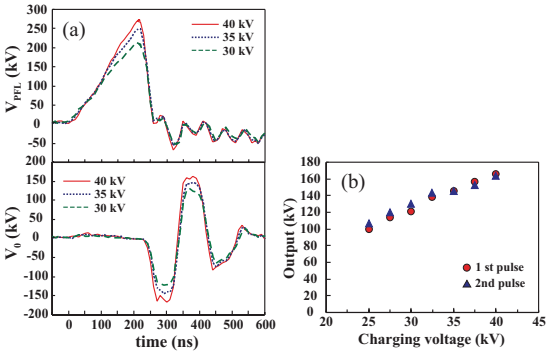

Fig.5 (a) Typical waveforms of V_{PFL} and V_0 and (b) output voltage as a parameter of the charging voltage of the Marx generator.

Figure 6 shows the dependence of the output waveform on the impedance of the dummy load (Z_L). We can see that the bipolar pulse is obtained in each Z_L condition. For the case of the lower impedance than the characteristic impedance of the line ($Z_L < 7.6\ \Omega$), the reflected waves are caused by the impedance mismatch between the TL and the dummy load, while as the impedance of the load approaches the characteristic impedance of the TL, i.e., the impedance matching condition is satisfied it decreases and vanishes. Thus, you may see from Fig.6 that the matching condition is around Z_L=10 Ω. This value does not agree with the designed characteristic impedance (7.6 Ω) of the TL. However, this disagreement can be explained as follows. In reality, the ceramic resistor with 20 cm length by 2 cm diameter is used as the voltage divider in the trigger circuit and inserted parallel to the inner conductor of the TL. We consider that this disagreement of the impedance matching condition may be attributed to the influence of the inserted resistor on the characteristic impedance of the TL.

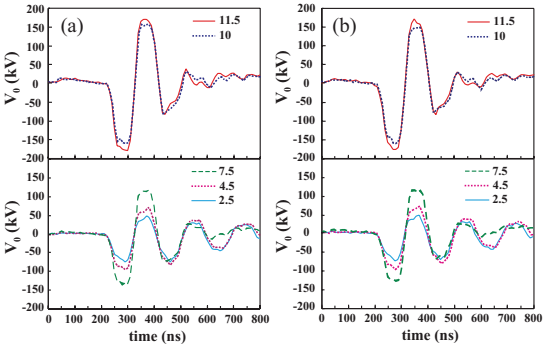

Fig.6 Dependence of the output waveform on the impeadance of the dummy load in case of (a) self-breakdown mode and (b) triggered mode.

The negative voltage pulse is observed right after the bipolar pulse, even though the impedance matching condition between the TL and the load is satisfied, as seen in Fig.5 and Fig.6. This is considered to be due to the impedance mismatch at the output end of the resistive voltage divider. Figure 7 displays the bipolar pulse waveform measured by the capacitive voltage divider in case of (a) Z_L=7.5 Ω and (b) Z_L=10 Ω, where the rail gap switch is operated in the self-broken mode and the same experimental parameters are utilized. The waveform of the charging voltage V_{PFL} is shown as the reference. It is evident from the comparison between Fig.7 and Fig.6(a) that the main part of the bipolar pulse is almost similar waveform, that is, square bipolar pulse and that the negative voltage pulse after the bipolar pulse is reduced. The reflected negative pulse due to the impedance mismatch between the TL and the load is observed for the case of Z_L=7.5 Ω [Fig.7(a)], whereas it vanishes for Z_L=10 Ω [Fig.7(b)]. Hence we can say that the impedance matched load is around 10 Ω.

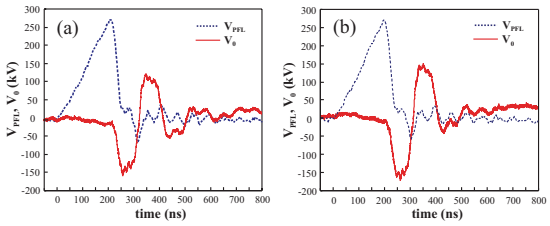

Fig.7 Typical waveform of bipolar pulse V_0(solid line) measured by capacitive voltage divider in case of (a) Z_L=7.5 Ω and (b) Z_L=10 Ω.

It is evident from Fig.6 that the rising time (10-90 % rise time) and the reversing time (90-90 % reverse time) of the bipolar pulse are almost constant for every load. For the self-broken operation, the rising time and the reversing time are evaluated to be around 30 ns and around 35 ns, respectively, whereas for the triggered operation the bipolar pulse has the rise time of around 35 ns and the reverse time of around 45 ns. These results show that the bipolar pulse waveform in the triggered mode tends to become duller than that in the self-broken mode. The above result can be explained by the following reason. In case of the triggered mode, the transition time of the rail gap

switch depends on the rise time of the trigger. In the circuit, the rise time of the trigger is limited by the stray capacitance and the resistor for the voltage divider, as seen in Fig.3(c). Thus, the rise time is estimated to be about 30 ns, which is in fairly good agreement with the experimental result $\sim$ 30 ns (see Fig.4(b)). In order to investigate the dependence of the reversing time of the bipolar pulse on the transition time of the output switch, the circuit simulation of the present system was performed. The simulation results show that the waveform of the bipolar pulse tends to become duller with the increase of the transition time. According to Ref.[10], the performance of the rail gap switch is extremely improved by increasing the number of conducting channels and the switching inductance of the multichannel rail gap switch can be reduced to less than 10 nH when using the mixture of SF_6 with N_2. There seems to be need for making improvements including the performance of the rail gap switch and the setting of the trigger circuit in order to produce the bipolar pulse with faster rise time and sharper reversing time. However, the developed bipolar pulse generator has good enough performance to carry out BPA experiments. Thus, we plan to perform the experimet on the production of an intense pulsed ion beam by the bipolar pulse accelerator after the bipolar pulse generator is installed in the B_y type magnetically insulated ion diode. Figure 8 illustrates the experimental system of the bipolar pulse accelerator.

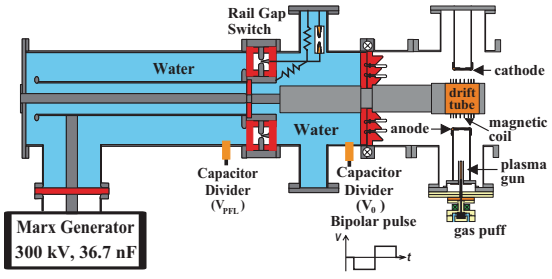

Fig.8 Experimental system of bipolar pulse accelerator.

Figure 9 shows the detail of the ion beam acceleration used in the experiment. The system consists of a grounded anode, a drift tube, a grounded cathode and a magnetically insulated acceleration gap(MIG). The anode and the cathode are the copper electrodes of diameter 78 mm, thickness 5 mm. The electrodes are uniformly drilled with apertures of diameter 4 mm, which gives the beam transmission efficiency of 58 %. The drift tube is connected to a high voltage terminal of the bipolar pulse generator. The magnetic coil of the MIG is installed on the rectangular drift tube and produces the uniform magnetic field of y-direction with strength of 0.4-0.5 T in the acceleration gap of $d_{\mathrm{A-K}}$=10 mm. The coil is powered by a capacitor bank of 500 μF and charging voltage 5 kV.

A gas puff plasma gun is used as the source plasma of the ion beam and consists of a high-speed gas puff valve and a coaxial plasma gun. To apply the pulsed current to the gas puff coil and the plasma gun, capacitor banks of 5 μF and 1.5 μF are used, respectively. Each capacitor is usually charged to 5 kV and 20 kV, respectively. Since it takes about a hundred μs to open the valve of the gas puff and several tens μs for N_2 gas to reach the gas nozzle of the plasma gun, the capacitor bank of the plasma gun is discharged with a delay time of τ_{d} around 300 μs. The bipolar pulse generator is fired at τ_{pp} = 9-20 μs after the rise of the the discharge current of the plasma gun, as shown in Fig.9. At present a biased ion collector (BIC) is installed inside the drift tube in ordr to confirm the acceleration of ions in the 1st gap.

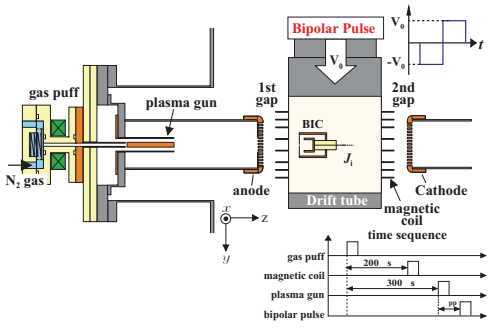

Fig.9 Cross-sectional view of ion beam acceleration.

5 Conclusion

We developed the bipolar pulse generator to perform proof of principle experiments of the bipolar pulse accelerator. The production of the bipo-

lar pulse with fast rise time and sharp reversing time was confirmed experimentally. We are planning to carry out the two-stage acceleration experiment by the bipolar pulse and to evaluate the beam quality in detail and modify it by optimizing the gap structure.

Acknowledgement

This work is supported in part by the Research Foundation for the Electrotechnology of Chubu and the Grant-in-Aid for Scientific Research from the Ministry of Education, Science, Sports and Culture, Japan.

References

[1] J. P. VanDevender and D. L. Cook, Science **232**, 831 (1986).

[2] A. D. Pogrebnjak, G. E. Remnev, I. B. Kurakin, A. E. Ligachev, Nucl. Instrum. & Methods in Phys. Res. B **36**, 286 (1989).

[3] D. J. Rej, *et al.*, Nucl. Instrum. & Methods in Phys. Res. B **127/128**, 987 (1997).

[4] B. X. Han, H. T. Zhang, W. J. Zhao, S. Yan, X. Y. Le, W. Xiang, T. M. Wang and G. E. Remnev, Suf. Coat. Technol. **158/159**, 482 (2002).

[5] Y. Hashimoto, M. Yatsuzuka, and S. Nobuhara, Jpn. J. Appl. Phys. **32**, 4838 (1993).

[6] K. Masugata, H. Okuda, K. Yatsui and T. Tazima, J. Appl. Phys. **80**, 4813 (1996).

[7] K. Masugata, Nuclear Instrum. & Methods in Phys. Res. A **411**, 205 (1998).

[8] K. Masugata, Y. Shimizu, Y. Fujioka, I. Kitamura, H. Tanoue and K. Arai, Nucl. Instrum. & Methods in Phys. Res. A **535**, 614 (2004).

[9] K. Igawa, T. Tomita, I. Kitamura, H. Ito and K. Masugata, Research Report, NIFS-PROC-64, pp.39-42 (2006).

[10] K. Masugata, H. Tsuchida, H. Saitou, and K. Yatsui, IEEE Trans. on Plasma Science **25**, 97 (1997).

DIAGNOSIS OF PULSED HEAVEY ION BEAM BY MAGNETICALLY INSULATED ION DIODE

H. Miyake, T. Ebie, R. Ou, I. Kitamura, H. Ito and K. Masugata
Faculty of Engineering, University of Toyama
3190 Gofuku, Toyama, 930-8555, Japan

Abstract

A magnetically insulated ion diode with an active ion source of a gas puff plasma gun has been developed in order to generate a high-intensity pulsed heavy ion beam for the implantation process of semiconductors and the surface modification of materials. When the ion diode was operated at diode voltage $\approx$ 190 kV, diode current $\approx$ 15 kA and pulse duration $\approx$ 100 ns, the ion beam with an ion current density of 54 A/cm^2 was obtained at 50 mm downstream from the anode. It was found from the evaluation of ion species and energy of the ion beam by a Thomson parabola spectrometer (TPS) that N^+ and N^{2+} beams of 100-300 keV energy were accelerated with proton impurities of 90-190 keV energy. The purity of the beam was estimated to be 94 %. In addition, to produce the pulsed metallic ion beam we developed the B_y type ion diode using a vaccum arc plasma gun instead of the gas puff plasma gun. The aluminum ion beam with an ion current density of 53 A/cm^2 was obtained at 50 mm downstream from the anode. We found from TPS measurement that the ion beam consisted of the Al^{2+} and Al^{3+} beams with the energy of 100-300 keV and the proton impurities with the energy of 110-170 keV.

1 Introduction

High-intensity pulsed heavy ion beam (PHIB) technology has been developed over the last two decades primarily for nuclear fusion and high energy density physics research[1]. One of most interesting topics is the application of PHIB to develop a unique pulsed energy source as a tool for the surface modification of materials[2−5]. Especially for the implantation process, PHIB technique has received extensive attention as a new type of ion implantation technology, since the ion implantation and the surface heat treatment or the surface annealing can be completed in the same time[6].

The pulsed ion beams usually are generated in conventional magnetically insulated ion diodes (MID) with transverse magnetic field in the acceleration gap to suppress the electron flow and enhance the ion flow. The conventional MID, however, has the fault that the producible ion species is limited to the material of electrode and that the beam usually contains much quantity of impurity ions[7], since the surface flashover ion source is used. Therefore, the conventional pulsed ion diode is not suitable for the implantaton process. We have developed a new type of B_y type MID with an active ion source of a gas puff plasma gun in order to produce the PHIB with acceptable purity. The nitrogen ion beam with ion current density $\sim$ 13 A/cm^2 and the purity of the beam $\sim$ 85 % has been obtained[8]. The ion current density, however, is not intense enough to apply PHIB to the implatation process.

A coaxial type Marx generator with a voltage of 200 kV and a current of 15 kA was developed and installed in MID to enhance the ion current density. As a result, the ion beam with a current density of J_i = 54 A/cm^2 and a pulse duration of 90 ns(FWHM) was obtained at 55 mm downstream from the anode[9]. In this paper, we report the evaluation of the ion species and the energy spectrum of the ion beam. In addition, the preliminary results of the experiment on the pulsed metallic ion beam by the MID using a vaccum arc

plasma gun are described.

2 Experimental Setup

A schematic configuration of the intense pulsed heavy ion diode system is illustrated in Fig.1. The system consists of a high voltage pulsed power generator, a gas puff plasma gun, a B_y type magnetically insulated ion acceleration gap (diode), and a stainless-steel vacuum chamber with a diffusion pump package. The Marx generator with the stored energy of 240 J at a charging voltage 50 kV is used as the pulsed power generator of the ion diode. The output parameter of the generator is voltage 200 kV, current 15 kA and pulse duration 100 ns(FWHM), which is applied to the anode of the ion diode. The vacuum chamber is evacuated to 5×10^{-3} Pa.

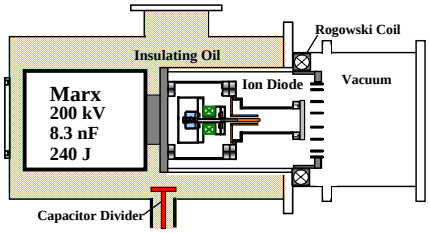

Fig.1 Schematic of the Ion Diode System.

Figure 2 shows the detail of the ion diode. The diode consists of a cylindrical anode of 115 mm length by 60 mm diameter and a cathode of grid structure. The acceleration gap length($d_{\mathrm{A-K}}$) is adjusted to 10 mm. The top of the anode is a stainless-steel plate, in which 37 holes of 5 mm diameter are drilled at the central area of the anode in order to allow the source plasma to inject into the acceleration gap. The cathode has a grid structure to pass through the accelerated ions. The cathode also acts as a multi-turn magnetic field coil in order to generate a transverse magnetic field in the acceleration gap to insulate the electron flow and enhance the ion flow. Thus, as shown in Fig. 2, the cathode(coil) has a shape like 8-character and is made of phosphor bronze strip of 10 mm width and 1 mm thickness. The coil is powered by a capacitor bank of 250 μF and charging voltage 5 kV. By applying a pulse current of 10 kA with rise-time 50 μs, a uniform magnetic field of 0.7 T is produced in the gap.

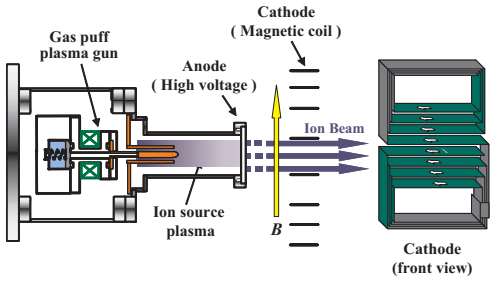

Fig.2 Cross-sctional view of B_y type MID.

The gas puff plasma gun is used as the ion source in order to produce the pulsed ion beam with high purity and is installed inside the anode. The plasma gun consists of a coaxial plasma gun and a high-speed gas puff valve. The plasma gun has a pair of coaxial electrodes, i.e. an inner electrode of 80 mm length by 6 mm outer diameter and an outer electrode of 18 mm inner diameter. The inner electrode has six gas nozzles of 1 mm diameter. The gas puff valve consists of a nylon vessel, an aluminum valve and a driver coil. The vessel is pre-filled with N_2 gas up to 1.4 atm. By discharging the capacitor bank of 20 μF and charging voltage 5.5 kV, a pulsed strong magnetic field is produced in the driver coil, which pushes the valve. As a result, the valve opens quickly in the time order of 100 μs and the gas expands with a supersonic velocity and is injected into the plasma gun via the nozzles on the inner electrode. After the injection of the gas, the ion source plasma is produced by discharging the capacitor bank of the plasma gun with the optimal delay time, since it takes $\sim$ 150 μs to open the valve and several tens μs for N_2 gas to reach the gas nozzle on the inner electrode of the plasma gun. The ion current density of the plasma produced by the plasma gun is estimated to be 28 A/cm^2 by a biased ion collector (BIC) placed at 90 mm downstream from the top of the plasma gun where the anode is placed in the acceleration experiment. The capacitor bank of 3.3 μF for the plasma gun is charged up to 17 kV.

The diode voltage (V_{d}) and diode current (I_{d}) are measured by the capacitive voltage divider and Rogowski coil, respectively. The values of diode voltage and diode current are calculated by the ratio factor of the voltage divider 136000 and

the coefficient of the Rogowski coil 27 kA/V. A biased ion collector(BIC) is used for the measurement of the ion current density .

3 Experimental Results

3.1 Evaluation of Pulsed nitrogen ion beam

Figure 3 shows typical waveforms of the diode voltage ($V_{\rm d}$), the diode current ($I_{\rm d}$) and the ion current density of the accelerated beam ($J_{\rm i}$). Here, the high voltage pulsed power generator is triggered at a delay time τ_d=10 μs after the rise of the discharge current of the plasma gun and $J_{\rm i}$ is measured by the BIC placed on the axis at $z = 50$ mm downstream from the surface of the anode. As seen in the Fig.3(a), $V_{\rm d}$ rises in 75 ns and has a peak of 190 kV, whereas I_d rises with $V_{\rm d}$ and has a peak of 15 kA at $t = 80$ ns. It can be seen from Fig.3(b) that the ion beam with a current density of $J_{\rm i} = 54$ A/cm^2 and a pulse duration of 90 ns(FWHM) is obtained at 30 ns after the peak of $V_{\rm d}$. Here, the waveform of $V_{\rm d}$ is shown as the reference. Considering the time of flight delay, the ion beam corresponding the peak of $J_{\rm i}$ seems to be accelerated around the peak of $V_{\rm d}$.

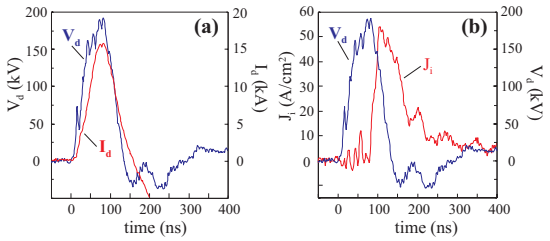

Fig.3 Typical waveforms of (a) diode voltage $V_{\rm d}$, diode current $I_{\rm d}$ and (b) ion current density $J_{\rm i}$.

A Thomson parabola spectrometer(TPS) was used for the evaluation of the ion species and the energy spectrum of the ion beam. Figure 4 shows the schematics of TPS used in the experiment. The TPS is constructed of a 1st pinhole, a 2nd pinhole, a magnetic deflector, an electric deflector and an ion detecting plate of CR-39. The spot size(d) of the beam on the detector is given by

$$d = (D_1 + D_2)(L_2/L_1) + D_2$$

where D_1 and D_2 are the diameters of the 1st and the 2nd pinholes, respectively, L_1 the distance beteween two pinholes, and L_2 the distance between the 2nd pinhole and the detector. In our experiment, we have chosen $D_1 = D_2 = 0.3$ mm, $L_1 = 20$ mm and $L_2 = 60$ mm, hence, giving $d = 2.1$ mm. The deflecting magnetic field of 0.8 T and the electric field of 0.6 MV/m are applied in the vertical direction. Thus, ions are deflected in the vertical direction and the horizontal direction by the electric field and the magnetic field, respectively. Figure 5 shows the typical track pattern on CR-39 obtained by TPS measurement. The measurement were done for 3 shots. It is clearly seen from Fig.5 that singly and doubly ionized nitrogen ions are observed with impurity of hydrogen ions. Since each ion track on CR-39 is produced by an irradiation of single ion, we have evaluated the ion number ratio on each ion species by counting the track number. The energy range and the number ratio of each ion species evaluated from the track pattern are summarized in table I. We see from the table that 6 % of impurity ions of protons are included in the beam, hence the purity of the beam is evaluated to be 94 %.

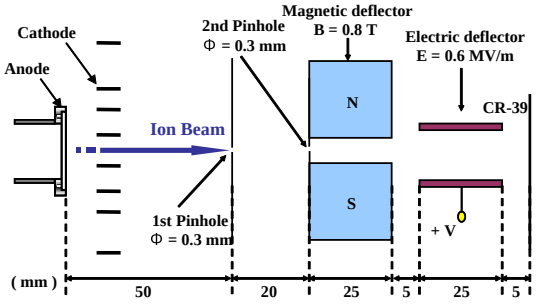

Fig.4 Schematic of Thomson parabola spectrometer.

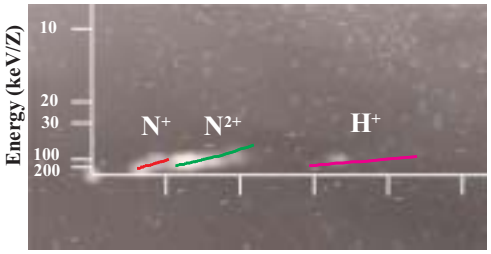

Fig.5 Typical track pattern on CR-39 by TPS.

Table.1 Energy and number ratio of each ion species evaluated by TPS.

Ion species	Energy (keV)	Number ratio (%)
N^+	110-300	94
N^{2+}	100-300	
H^+	90-200	6

3.2 Generation of pulsed metallic ion beam

Pulsed metallic ion beams have received extensive attention for the material processes, however, they cannot be obtained yet. We have developed the vacuum arc discharge ion source as an intense pulsed metallic ion source[8,10]. Figure 6 shows the experimental setup to evaluate the characteristics of the vacuum discharge ion source. As shown in in the inset of Fig.6, a coaxial type configuration is used as the vacuum discharge electrodes. A capacitor bank of 1 μF and charging voltage 30 kV is connected anode to cathode and the discharge is triggered by applying 20 kV spark between the trigger electrode and the cathode. The experiment is done in the vacuum of 4×10^{-3} Pa.

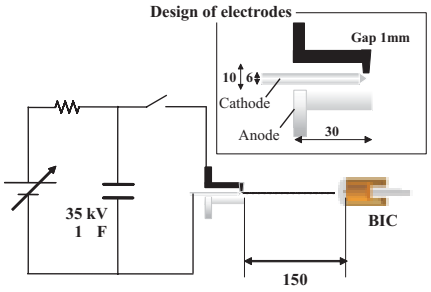

Fig.6 Experimental setup of vacuum arc discharge ion source.

The ion current density of the plasma (J_i) produced by the plasma gun was evaluated by the BIC placed on the central axis at 150 mm downstream from the top of the plasma gun. Figure 7 shows the typical waveforms of the discharge current (I_a) and the ion current density (J_i). As seen in Fig.7, the discharge current I_a has a sinusoidal waveform of peak current 12.5 kA and quarter cycle 2.2 μs. The ion beam with the peak current density J_i=254 A/cm^2 and the pulse duration of 1.5 μs is observed at about τ_peak = 7.4 μs after the rise of I_a.

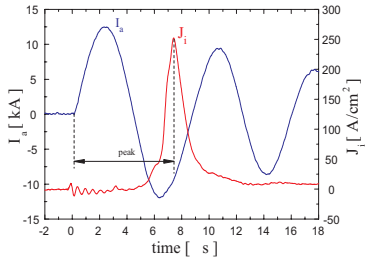

Fig.7 Typical waveforms of I_a and J_i.

In order to evaluate the drift velocity of the plasma by a time of flight method (TOF), two BIC's are placed at 100 and 150 mm downstream from the discharge gap, respectively. The TOF delay time between two BIC signals is 1.9 μs, which gives the drift velocity of 2.6×10^4 m/s. Assuming aluminum ions it corresponds to the ion energy of 95 eV.

The vaccum arc plasma gun is installed into the B_y type ion diode in order to produce the pulsed metallic ion beam. Both ion diode system and measurement setup are the same as the experimental system for the nitrogen ion beam except that the vaccum arc plasma gun is employed as the ion source. Figure 8 shows typical waveforms of the diode voltage (V_d), the diode current (I_d) and the ion current density of the accelerated beam (J_i). As seen in Fig.8(a), V_d rises in 50 ns and has a peak of 200 kV. On the other hand, I_d rises with V_d and has a peak of 10 kA at t = 75 ns and after that decreases. Figure 8(b) shows the ion current density of the accelerated beam J_i measured by the BIC placed on the axis at z = 50 mm downstream from the surface of the anode. From the figure, we see that the ion current density of 53 A/cm^2 was generated with a pulse width of 40 ns(FWHM) after the rise of V_d.

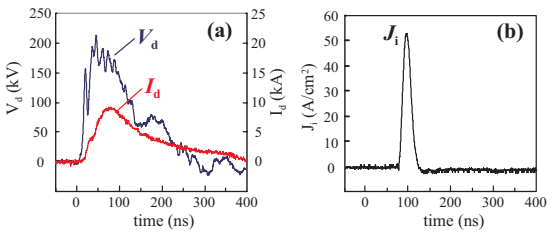

Fig.8 Typical waveforms of (a) diode voltage V_d, diode current I_d and (b) ion current density J_i.

The ion species and the energy spectrum of the ion beam was evaluated by using the above-mentioned TPS. Figure 9 shows the typical track pattern on CR-39. Here, the measurement were done for 1 shot. We found from the figure that the ion beam consisted of Al^{2+} and Al^{3+} beam with an energy of 100-300 keV and impurity of proton with an energy of 110-170 keV. This result means that the pulsed metallic ion beam is suc-

cessfully obtained by the magnetically insulated ion diode with an active ion source of the vaccum arc plasma gun.

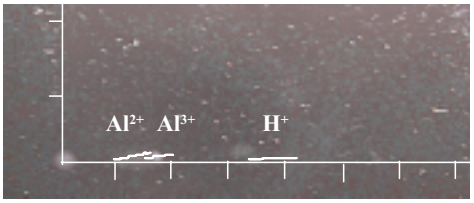

Fig.9 Typical track pattern on CR-39 by TPS.

4 Summary

We have developed the magnetically insulated ion diode using two type of plasma guns, i.e. a gas puff plasma gun and a vacuum arc plasma gun in order to generate variety of ion beams. In case of the gas puff plasma gun, when the ion diode was operated at diode voltage 190 kV, diode current 15 kA, and pulse duration 100 ns (FWHM), the nitrogen ion beam with an ion current density of 54 A/cm^2 and a pulse duration of 90 ns was obtained at 50 mm downstream from the anode. From the evaluation of the energy and ion species of the beam by a Thomson parabola spectrometer, we found that the ion beam consisted of N^+ and N^{2+} beam with an energy of 100-300 keV and impurity of proton with an energy of 90-190 keV. The purity of the nitrogen beam was estimated to be 94 %. In case of the vacuum arc plasma gun, the aluminum ion beam with an ion current density of 53 A/cm^2 was obtained at 50 mm downstream from the anode when the diode voltage and the diode current are 200 kV and 10 kA, respectively. The evaluation by TPS measurement shows that Al^{2+} and Al^{3+} beam of energy 100-300 keV were accelerated with impurity of protons of energy 110-170 keV. We need to measure the purity of the aluminum ion beam.

Acknowledgement

This work is supported in part by the Grant-in-Aid for Scientific Research from the Ministry of Education, Science, Sports and Culture, Japan.

References

[1] J.P. VanDevender and D.L. Cook, Science **232**, 831 (1986).

[2] K.Yatsui, Laser Particle Beam **7**, 733 (1989).

[3] H.A. Davis, G.E. Remnev, R.W. Stinnett and K. Yatsui, Mater. Res. Bull. **21**, 58 (1996).

[4] H. Akamatsu, Y. Tanihara, T. Ikeda, K. Azuma, E. Fujiwara and M. Yatsuzuka, Jpn. J. Appl. Phys. **40**, 1083 (2001).

[5] C.A. Meli, K.S. Grabowski, D.D. Hinshelwood, S.J. Stephanakis, D.J. Rej and W.J. Waganaar, J. Vac. Sci. Technol. **A13**, 1182 (1995).

[6] K. Masugata, *et al.*, Proc. 25th Int. Power Modulator Sympsoium, 2002 (Hollywood, CA, USA, 2002) pp.552-555.

[7] K. Masugata, H. Okuda, K. Yatsui and T. Tazima, J. Appl. Phys. **80**, 4813 (1996).

[8] K. Masugata, R. Tejima, M. Higashiyama, J. Kawai, I. Kitamura, H. Tanoue and K. Arai, Plasma Device and Operations **13**, 57 (2005).

[9] H. Ito, M. Higashiyama, S. Takata, I. Kitamura and K. Masugata, Research Report, NIFS-PROC-64, pp.43-48 (2006).

[10] I. Brown, Rev. Sci. Instrum. **65**, 3061 (1994).

EFFECT OF LONGITUDINAL SELF-ELECTRIC FIELD DURING PULSE COMPRESSION FOR HIGH-CURRENT HEAVY-ION BEAMS

T. Kikuchi, S. Kawata*, and K. Horioka**

Department of Electrical and Electronic Engineering, Utsunomiya University, Utsunomiya 321-8585, Japan
*Department of Energy and Environmental Science, Utsunomiya University, Utsunomiya 321-8585, Japan
**Department of Energy Sciences, Tokyo Institute of Technology, Yokohama, 226-8502, Japan

ABSTRACT

Three dimensional beam dynamics during a longitudinal pulse compression is numerically investigated by using a multi-particle code developed with a reduced electric field model. Longitudinal self-electric field causes a deformation of the beam particle distribution in phase space during the beam transport with the pulse compression. An rms transverse emittance growth is additionally increased along the beam transport due to the disruption in the longitudinal distribution of the beam particle.

1 Introduction

In a heavy ion inertial fusion (HIF) system [1] , energy of several MJ should be injected as a short time pulse to a fuel pellet. The target pellet illuminated by the energy driver is rapidly imploded into the center. The implosion driven can cause a high energy density state at the center of the pellet, and the high-temperature dense plasma can produce a lot of thermonuclear reactions. An intense heavy-ion beam (HIB) is one influential candidate as the energy driver, and the physics of space-charge-dominated beams is crucial in the HIF researches [1].

Required parameter values of HIB are several GeV particle energy, ∼100 kA total current, and ∼10 ns short pulse duration [2]. The beam parameters are far from those of conventional particle accelerator system. Therefore the beam dynamics and control are important research issues in HIF.

Not only for HIF, but also research fields on high energy density physics (HEDP) and warm dense matter (WDM) sciences [3] driven by HIB illuminations require the generation of a high-current HIB.

At the final stage, the beam pulse must be longitudinally compressed from ∼100 to ∼10 ns. Induction voltage modulators, which have a precise waveform controllability, are useful devices for the bunch compression [4]. For an effective pellet implosion, we should transport and compress the bunch of HIB with a low emittance growth. A final focus and beam illumination are crucial, but a large emittance interferes the focusing to the small fuel pellet [5]. For this reason, the final pulse compression and the final focusing are a key technology in the HIF driver system. In these regions, the intense HIB is in the space-charge-dominated state, and beam instabilities may occur during the beam transport. Redistribution of particles in phase space can also cause the emittance growth, because nonequilibrium particle distribution will approach with dissipation to a thermal equilibrium state [6].

In our previous studies [7, 8, 9], the beam dynamics was investigated by using a two dimensional multi-particle code including the longitudinal pulse compression model. We carry out numerical simulations by using a three dimensional particle code in this study. The longitudinal and

transverse beam parameter changes are discussed from the numerical simulation results during the pulse compression. Disruption of the longitudinal particle distribution is shown in the beam transport, and implies that an emittance growth larger than one near center of the beam bunch is caused due to the longitudinal particle motions.

2 Simulation model and beam parameters

The calculation code used, which is based on a particle-in-cell (PIC) method [10] , takes into account of a self-electrostatic and an external applied magnetic fields, and can be described in a three dimensional Cartesian coordinate. The particle motions are calculated in the fully three dimensional space by neglecting a self-magnetic field.

The electric field created due to the space charge is calculated by using the Poisson equation,

$$\nabla^2\phi = \frac{\partial^2\phi}{\partial x^2} + \frac{\partial^2\phi}{\partial y^2} + \frac{\partial^2\phi}{\partial z^2} = -\frac{\rho}{\epsilon_0}, \qquad (1)$$

where ϕ is the electrostatic potential, ρ is the charge density, and ϵ_0 is the permittivity of free space. By solving Eq. (1), the electric field can be completely determined by $\boldsymbol{E} = -\boldsymbol{\nabla}\phi$, however the higher computational cost is unaffordable for a lot of parameter studies. Vorobiev and York proposed a sub-three-dimensional PIC method [11], and the approach is as follows. The three dimensional Poisson equation Eq. (1) can be replaced as

$$\frac{\partial^2\phi}{\partial x^2} + \frac{\partial^2\phi}{\partial y^2} = -\rho', \qquad (2)$$

where

$$\rho' = \frac{\rho}{\epsilon_0} - \frac{\partial E_z}{\partial z}. \qquad (3)$$

If Eq. (3) can be solved with including the transverse information, we can obtain the transverse electric field by solving the two dimensional Poisson equation as shown in Eq. (2).

Assuming the large aspect ratio to longitudinal and transverse directions for the beam bunch, we employ the simplified calculation model for the longitudinal electric field in this study. The transverse electric fields are normally calculated by

$$E_x = -\frac{\partial\,\phi}{\partial x}, \qquad (4)$$

$$E_y = -\frac{\partial\,\phi}{\partial y}, \qquad (5)$$

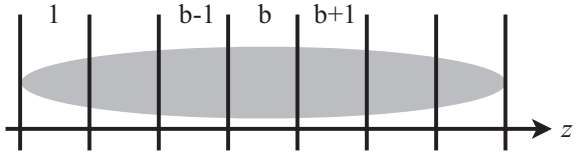

Figure 1: Sliced bunch model for the self-electric field calculations.

while by assuming the long wave approximation the longitudinal electric filed can be given as

$$E_z = -\frac{g}{4\pi\epsilon_0{\gamma_0}^2}\frac{d\lambda}{dz}, \qquad (6)$$

where γ_0 is the relativistic factor at the central energy for the beam and λ is the line charge density. For a space-charge dominated regime, g is the geometry factor defined by

$$g \sim \log\frac{r_p^2}{r_x r_y}, \qquad (7)$$

where r_p is the outer boundary pipe radius, r_x and r_y are effective beam radii estimated as

$$r_x = 2\sqrt{\langle(x_p - \langle x_p\rangle)^2\rangle}, \qquad (8)$$

$$r_y = 2\sqrt{\langle(y_p - \langle y_p\rangle)^2\rangle}, \qquad (9)$$

where x_p and y_p are the transverse positions of the beam particle at the index p.

To reduce the computational cost, the beam bunch is longitudinally sliced and separated to calculate the transverse and longitudinal electric fields as shown in Fig. 1. At each time-step the bunches sliced are identified by using the index b. The transverse electric fields are calculated at each slice. For this reason, the horizontal and vertical electric fields are rewritten as

$$E_{xb} = -\frac{\partial\,\phi_b}{\partial x}, \qquad (10)$$

$$E_{yb} = -\frac{\partial\,\phi_b}{\partial y}, \qquad (11)$$

at each slice. Here the subscripts b indicate the sliced bunch index. The electrostatic potential at each slice can be calculated by

$$\frac{\partial^2\phi_b}{\partial x^2} + \frac{\partial^2\phi_b}{\partial y^2} = -\rho_b', \qquad (12)$$

where

$$\rho_b' = \frac{\rho_b}{\epsilon_0} - \frac{dE_{zb}}{dz}. \qquad (13)$$

Here

$$\frac{dE_{zb}}{dz} = -\frac{1}{4\pi\epsilon_0{\gamma_0}^2}\frac{d}{dz}\left(g_b\frac{d\lambda_b}{dz}\right). \qquad (14)$$

The Poisson equation at each slice can be numerically solved by using a multigrid and SOR methods [12].

The beam parameters are assumed as Table 1 [2]. The initial generalized perveance is assumed to be

Table 1: Beam parameters.

Ion species	Pb^{1+}
Number of ions	6.25×10^{14}
Particle energy [GeV]	10
Initial beam current [A]	400
Final beam current [kA]	10
Initial pulse duration [ns]	250
Final pulse duration [ns]	10

3.58×10^{-6}. The initial undepressed and depressed phase advances are $\sigma_0 = 72$ deg and $\sigma = 65.2$ deg at 3 m in the longitudinal direction. A continuous focusing (CF) configuration is assumed for the transverse confinement system. The transverse focusing coefficients $k_x = k_y = 0.157$ m^{-2} are constant for the CF model.

The transverse calculation region is fixed at the square of 10 cm × 10 cm, and the outer boundary condition is given as a conductor wall. As a result, the pipe radius r_p is assumed as 5 cm in this study.

The rms matched Gaussian [13] beam is chosen as the initial particle (non-stationary) distribution for the transverse plane. The longitudinal charge distribution is assumed to be uniform before the bunch compression, on which a velocity tilt of 5 % is applied.

3 Longitudinal and Transverse Beam Parameters during Pulse Compression

We simulate numerically the beam dynamics during the pulse compression with the CF focusing model as discussed in the previous section.

Figure 2 shows the line charge density profiles at each longitudinal position during the beam transport. Due to the head-to-tail velocity tilt given initially, the beam bunch is longitudinally compressed during the transport, and the line charge density can be increased with the pulse compression.

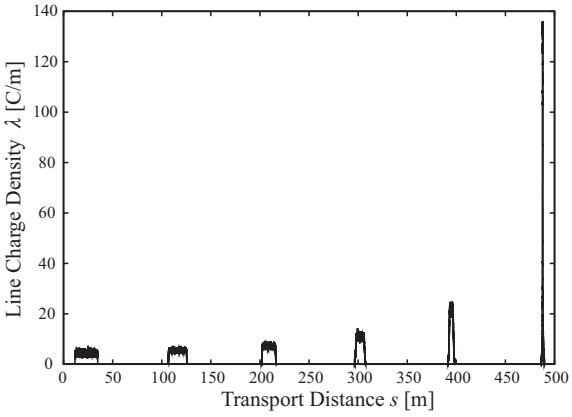

Figure 2: Line charge density along the beam transport direction.

Figure 3 shows the particle map in the longitudinal phase space and the longitudinal electric field at each transport distance s. As shown in Fig. 3, the particle distribution profile can be rotated in the longitudinal phase space, and the amplitude of the longitudinal electric field is increased due to the line charge density growth. At $s = 460$ m, a disruption of the smooth particle distribution in the longitudinal phase space is indicated by Fig. 3. The disruption is caused by increasing the amplitude of the longitudinal electric field due to the pulse compression.

The emittance value can be used to evaluate the beam quality. We define the average of unnormalized rms transverse emittance ε as

$$\varepsilon = \frac{\varepsilon_{x,rms} + \varepsilon_{y,rms}}{2}, \qquad (15)$$

where $\varepsilon_{x,rms}$ and $\varepsilon_{y,rms}$ are the unnormalized rms emittances for horizontal and vertical directions given by

$$\varepsilon_{x,rms} = \left[\langle x_p^2\rangle\langle x_p'^2\rangle - \langle x_p x_p'\rangle\right]^{1/2}, \qquad (16)$$

and

$$\varepsilon_{y,rms} = \left[\langle y_p^2\rangle\langle y_p'^2\rangle - \langle y_p y_p'\rangle\right]^{1/2}, \qquad (17)$$

where the prime ($\prime$) indicates the slope, i.e., $x_p' = dx_p/dz_p$ and $y_p' = dy_p/dz_p$, respectively. The initial emittance ε_i is assumed to be ε_i =10 mm-mrad, and $\varepsilon_{x,rms} = \varepsilon_{y,rms} = \varepsilon_i$. The evolutions of the emittance growth $\varepsilon/\varepsilon_i$, which indicates the ratio of the average emittance to the initial one along the transport distance, are shown in Fig. 4.

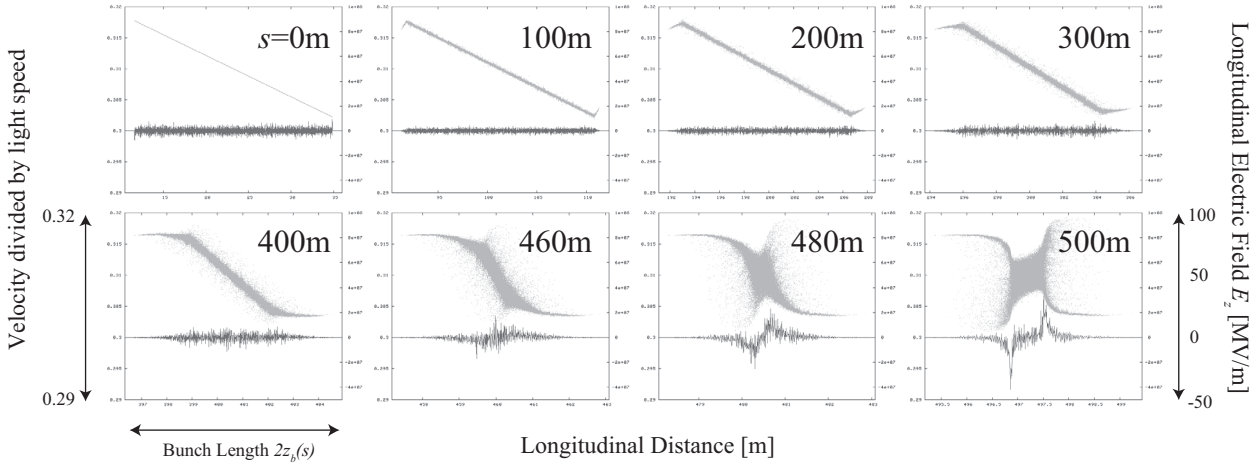

Figure 3: Particle distribution (dots) and longitudinal electric field (lines) at each transport distance in the longitudinal phase space during beam transport with pulse compression.

The emittance growth over the entire beam is calculated by considering all beam particles, and the emittance growth near center is evaluated by the particles included in the range of ±10 cm fixed from the longitudinal center of the beam bunch. As shown in Fig. 4, the emittance growth evaluated near center of the beam bunch is lower than one over the entire beam bunch. As a result, the large transverse emittance growth over the entire beam bunch can be caused due to the disruption of the particle distribution in the longitudinal phase space at $s \geq 460$ m as shown in Fig. 3.

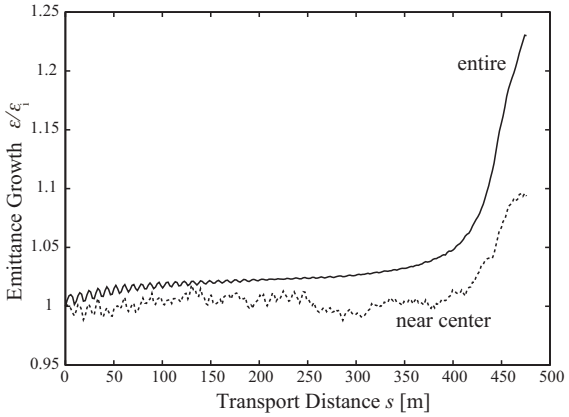

Figure 4: Evolution of the rms emittance during the beam transport with the pulse compression. The solid curve indicates the emittance growth over the entire beam bunch, and the dotted line shows one evaluated near center of the beam bunch.

4 Conclusions

A high-current HIB dynamics during the beam transport with a longitudinal pulse compression was numerically investigated by using a three dimensional particle simulation code. The used code was developed to solve the three dimensional particle motions with the reduced electric field due to the space charge effect and the applied external magnetic field for the transverse confinement of the beam.

A disruption of smooth particle distribution in phase space for the longitudinal pulse compression was indicated, and was found to be caused due to the longitudinal self-electric field. A comparison of emittance growth between the all particles in the beam bunch and the particles included near center of the beam bunch implies that the rms emittance growth over the entire beam can be increased due to the disruption of the longitudinal particle distribution.

Acknowledgments

This work was carried out under the collaborating research program at National Institute for Fusion Science. This work was supported by JSPS (Japan Society for the Promotion of Science) No. 17740361 and MEXT (Ministry of Education, Culture, Sports, Science and Technology).

References

[1] J.J. Barnard, J. Fusion Energy **17**, 223 (1998).

[2] J.J. Barnard, R.O. Bangerter, A. Faltens, T.J. Fessenden, A. Friedman, E.P. Lee, B.G. Logan, S.M. Lund, W. Meier, W.M. Sharp, and S.S. Yu, Nucl. Instrum. Methods in Phys. Res. **A415**, 218 (1998).

[3] T. Sasaki, *et. al.*, in this proceedings.

[4] K. Horioka, M. Nakajima, M. Watanabe, M. Honda, E. Hotta, M. Shiho, M. Ogawa, J. Hasegawa, J. Kishiro, and K. Takayama, Laser Part. Beams **20**, 609 (2002).

[5] T. Someya, A.I. Ogoyski, S. Kawata, and T. Sasaki, Phys. Rev. ST Accel. Beams **7**, 044701 (2004).

[6] S.M. Lund, D.P. Grote, and R.C. Davidson, Nucl. Instrum. Methods in Phys. Res. **A 544**, 472 (2005).

[7] T. Kikuchi, M. Nakajima, K. Horioka, and T. Katayama, Phys. Rev. ST Accel. Beams **7**, 034201 (2004).

[8] T. Kikuchi, T. Someya, S. Kawata, M. Nakajima, K. Horioka, and T. Katayama, Nucl. Instrum. Methods in Phys. Res. **A 544**, 262 (2005).

[9] T. Kikuchi, S. Kawata, M. Nakajima, and K. Horioka, NIFS-PROC-64, 71 (2006).

[10] R.W. Hockney and J.W. Eastwood, *Computer Simulation Using Particles*, McGraw-Hill, New York, (1981).

[11] L.G. Vorobiev and R.C. York, Phys. Rev. ST Accel. Beams **3**, 114201 (2000).

[12] U. Trottenberg, C.W. Oosterlee, and A. Schüller, *MULTIGRID*, Elsevier, San Diego, (2001).

[13] Y.K. Batygin, Nucl. Instrum. Methods in Phys. Res. **A 539**, 455 (2005).

Beam Manipulation with Controllable Induction Voltage Cell

Takato Ishii*, Toru Sasaki, Mitsuo Nakajima, Tohru Kawamura, and Kazuhiko Horioka
Department of Energy Sciences, Interdisciplinary Graduate School of Science and Engineering, Tokyo Institute of Technology, 4259 Nagatsuta, Midori-ku, Yokohama 226-8502, Japan

In order to simulate beam manipulation in high power acceleration system, a proto-type induction modulator with voltage adder configuration is developed. The modulator is composed of 5-unit of induction cells and FET-based voltage drivers. The induction unit can generate a voltage with sinusoidal shape and those module pulses are superimposed at an acceleration gap. Using this modulator, electron beams are accelerated and longitudinally compressed. Effects of self-electric field and initial emittance for the bunch compression ratio are discussed based on the beam manipulation experiments.

Keywords: Induction acceleration,Pulse modulator,Waveform synthesis,Intense beams, Bunch compression

I. INTRODUCTION

Huge accelerators have been developed so far to enhance the particle energy as a tool for high energy physics. Except for the size and cost issues, the acceleration technology itself is relatively well established for the generation of high energy particles. On the other hand, application of particle beams to such as the energy driver of inertial fusion, needs extremely high current beams rather than high energy beams. Then the generation of high flux particles and transport of high current beams are of critical issues for high power acceleration technology.

Induction accelerator can generate high current beams of order of kA. High power induction acceleration has been studied for plasma heating or energy driver of inertial confinement fusion. [1][2][3][4] In addition, induction acceleration cavity is partly placed in conventional RF Synchrotron in KEK(High Energy Accelerator Research Organization) Induction Synchrotron.[5][6]

Conventional high power induction accelerators have a lot of issues including controllability and repeatability. In particular, high current beams are difficult to transport because they are dominated by the space charge field. To create high current beam, a method of avoiding the space charge effect is inevitable. In the concept of Heavy Ion Fusion(HIF), long pulse and low current beams must be compressd in proportion to beam energy as shown in Fig.1.[7][8][9] To compress the beam bunch (Beam Bunching), the acceleration waveforms have to be controlled with high accuracy.

From above-mentioned backgrounds, we have developed induction acceleration module composed of 5 units. This module utilizes a voltage adder configuration to control the voltage waveform at high current level.

II. INDUCTION ACCELERATION AND VOLTAGE ADDER METHOD

The principle of induction acceleration is usually explained by a transformer model. The induced electromotive force is derived by the Maxwell's equations,

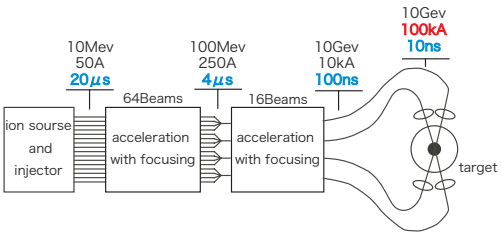

FIG. 1: HIF concept using induction accelerator

$$rot\boldsymbol{E} = \frac{\partial \boldsymbol{B}}{\partial t} \tag{1}$$

$$\oint \boldsymbol{E} \cdot d\boldsymbol{\ell} = -\int \frac{\partial \boldsymbol{B}}{\partial t} \cdot d\boldsymbol{S}. \tag{2}$$

When $\frac{\partial \boldsymbol{B}}{\partial t} = const$, relation between acceleration voltage V and pulse width τ is derived by following equation.

$$V\tau = \Delta \boldsymbol{B} \cdot \boldsymbol{S} \tag{3}$$

This equation is not contain any term of beam current. This means the induction accelerators have intrinsically high ability to drive the current.

In addition, as the core is surrounded with conductor, it can be stacked to concentrate the electrical potential into the acceleration gap.

We have developed an induction modulator using voltage adder configuration to control the voltage waveforms. In this method, acceleration voltages for the bunching are generated by adding multiple sinusoidal waves of half period. By controlling the peak voltage and the phase of the sinusoidal waves, any shape of voltage can be synthesized.

This method have the following advantages. First, sinusoidal waves can be generated by a simple LC circuit. Second, the electric power consumption per unit module can be controlled at low level so as to use semiconductor switching devices.

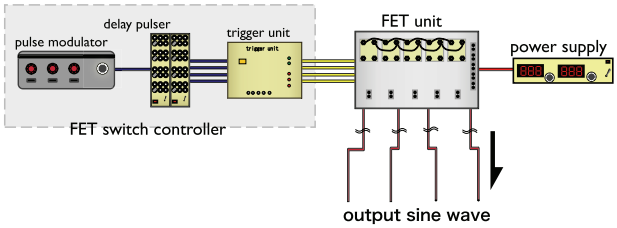

FIG. 2: Schematic of the voltage controller

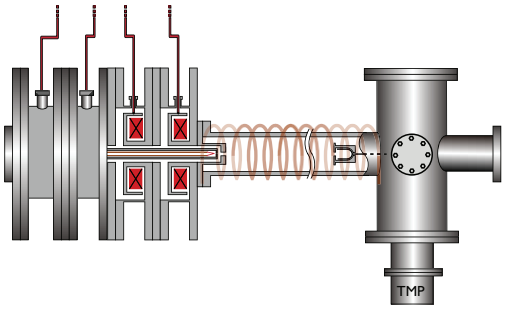

FIG. 3: Acceleration cavity and transport line

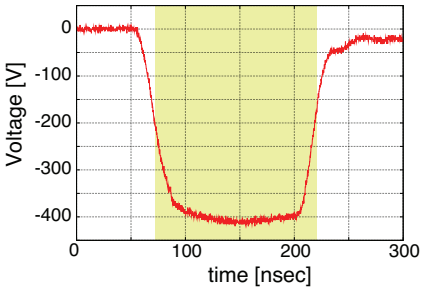

FIG. 4: Extraction voltage at beam injector

III. EXPERIMENTAL SETUP

A. Voltage controller

A schematic diagram of the equipments for generating the acceleration voltage are shown in FIG.2. The FET unit consists of a LC circuit and MOSFET switching devices. The delay pulser can independently control each module.

B. Acceleration cavity and transport line

In this experiment, 4 modular units are used to make the induction acceleration cavity (FIG.3) . Each units are independently driven and the generated voltages are added in the acceleration gap. Magnetic cores made of FINEMET were used for the induction module.

As the source of charged particles, electro-thermal electrons generated from tungsten filament are used. Beam dynamics in a high power ion accelerators can be simulated by the electron beam source in the laboratory with selection of proper scaling parameters for beam velocity and/or charge/mass ratio; for example, $\beta(= v/c)$ value of 400eV electron is equal to 100MeV heavy ions.

At first, the electrons generated from the filament are extracted by field emission(the extraction pulse voltage is shown in FIG.4). The extracted beam was accelerated at the acceleration gap by the synthesized voltage. In this study, waveforms of beam current were observed through a magnetically guided transport line with 6cm in diameter, as a fuction of the transport distance that is from 5cm to 180cm. To confine the transverse motion of the beam, about 300G solenoidal magnetic field is applied along the longitudinal axis. From this beam transport experiments, 4 parameters of the beam bunch can be measured; arrival time of beam head, arrival time of beam end, bunch length, and distribution of current density.

IV. EXPERIMENTAL RESULT

The electron beams were manipulated with 2 modes :acceleration mode and compression mode. The synthesized waveform for acceleration is shown in FIG.5(a) and for beam compression is shown in FIG.5(b). The shadow areas in the figures indicate the effective time duration of beam acceleration.

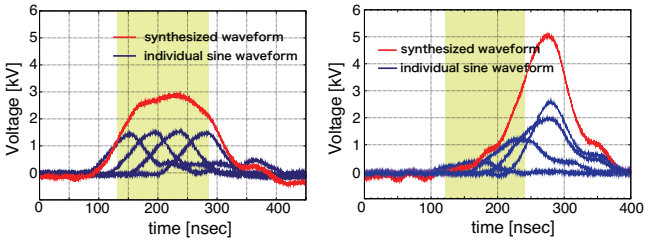

(a) Synthesized waveform for acceleration

(b) Synthesized waveform for compression

FIG. 5: Acceleration voltage consists of multiple sine waves

Typical results of acceleration experiment are shown in FIG.6 and FIG.7. The shadow area in the figure are defined for beam width. As shown in the figure, in case of acceleration mode, the injected beam was transported with the same pulse width.

Typical results of beam waveform for the compression mode are shown in FIG.8 and FIG.9. As shown in these figures, the beam was compressed to one third of initial pulse length through the 180cm transport.

Possible factors that degrade the bunching ration of the charged particle beams in the compression experiment are: inaccuracy of the voltage waveform, initial

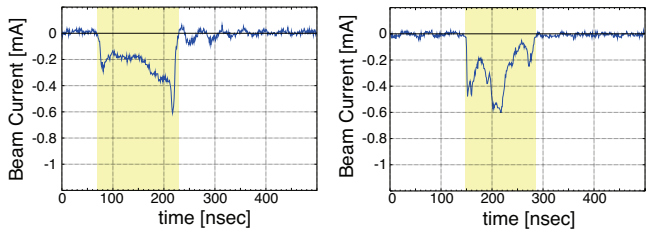

(a) transport distance=5cm (b) transport distance=180cm

FIG. 6: Typical current waveform at acceleration experiment

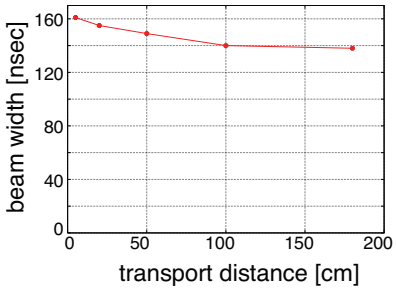

FIG. 7: Variation of beam width along the transport line for acceleration experiment

emittance, its growth by the self electrical field, and an uncleared collective effect. To discuss these factors, we made a simple time-of-flight simulation. In the simulation, electron beam with uniform velocity of 400eV was injected and accelerated by the synthesized voltage shown in FIG.5(b). The comparison between the experimental result and the calculation result is shown in FIG.10. From the comparison, effects of space charge effect is indicated as a cause of the decrease of compression ratio.

To explain which factor is dominant to the decrease of compression ratio, additional simulation was made. In the additional simulation, injected beam had been applied a velocity gradient for the bunching as shown in FIG.11. However we could observe only a slight variation on the current waveform. From this result we can conclude that initial emittance is not the dominant factor in this experimental condition. It becomes apparent that self electrical field is a dominant factor for the beam expansion.

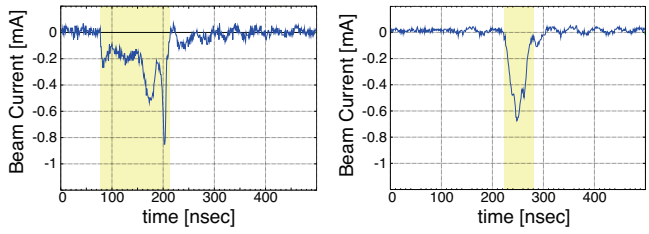

(a) transport distance=5cm (b) transport distance=180cm

FIG. 8: Typical current waveform at compression experiment

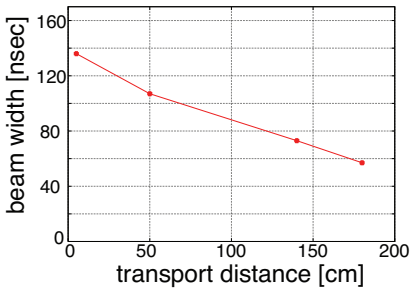

FIG. 9: Variation of beam width along the transport line for compression experiment

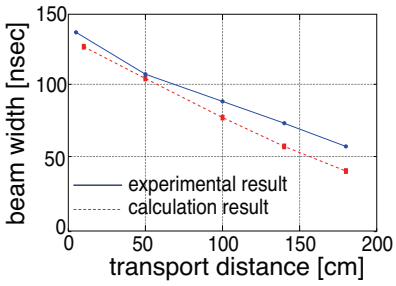

FIG. 10: Comparison between experiment and calculation result

The time scale of collective motion of charged particles can be represented as a period of plasma oscillation $1/\omega_p$. Here, ω_p of non-neutral electron beam. A period of plasma oscillation derived from the current density is about 20nsec. This is adequately short compared with the beam transport time (about 150nsec). So in this experiment electrons in the beams must move collectively by force of self electric field and this motion may also affect the decrease of compression ratio.

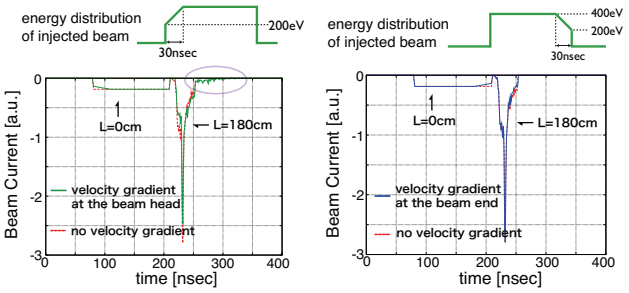

(a) have velocity gradient at beam head (b) have velocity gradient at beam end

FIG. 11: Calculation result when injected beam have velocity gradient

V. SUMMARY

Altough longitudinal beam compression is inevitable in high power (high current) accelerators, beam dynamics in the bunch compression process is not yet clarified.[10] We proposed a simulated experiment for the bunch compression based on electron beam transport experiments. For the beam manipulation experiments, we developed a system composed of an electron beam injector, an induction voltage modulator, and a magnetically guided beam transport line. We have demonstrated applicability of the induction voltage modulator for the beam experiments.

Using the experimental system, electron beams were manipulated with two modes : acceleration and bunch compression mode. From the preliminary experiments the following results were obtained.

In acceleration mode, an electron beam was accelerated and transported with the same pulse width by the acceleration voltage with flat-top waveform. In compression experiment, the electron beam was longitudinally compressed from 140nsec to 55 nsec.

To evaluate the effects of space charge field and initial emittance in the compression process, numerical simulation was done. Results show that, in this condtion, self electrical field is a dominant factor to the decrease of compression ratio.

From above-mentioned discussion, we can conclude that our experimental system can simulate physical phenomena of space charge dominated beam. We are expecting that this device is useful tool for evaluating the effect of velocity gradient, emittance growth, and the collective behavior of the bunching beam, on the compression process.

Acknowledgments

This work was partly supported by Ministry of Education, Culture, Sports, Science and Technology.

[1] M.Shiho, A.Watanabe, T.Koarai, S.Maebara, H.Ishizuka, K.Takayama, J.Kishiro, K.Horioka, M.Ogawa, S.Kawasaki; Nucl. Instr. Meth., A393, pp.289-294 (1997) .

[2] K.Horioka, T.Kawamura, M.Nakajima, T.Sasaki, K.Kondo, et.al.; Nucl. Instr. Meth., A577, pp.298-302 (2007) .

[3] I.Morimoto, X.D.Zheng, S.Maebara, J.Kishiro, K.Takayama, K.Horioka, H.Ishizuka, S.Kawasaki, M.Shiho; Direct Observation of Beam Bunching in BWO Experiments; Nuclear Instr. Methods, A-475, pp.509-513 (2001).

[4] T.C.Sangster, J.J.Barnard, T.V.Cianciolo, G.D.Craig, A.Friedman, D.P.Grote, E.Halaxa, R.L.Hanks, G.Kamin, H.C.Kirbie, B.G.Logan, S.M.Lund, G.Mant, A.W.Molvik, W.M.Sharp, S.Eylon, D.Berners, T.J.Fessenden, D.L.Judd, L.Reginato, H.S.Hopkins, A.Debeling, W.Fritz, and J.Meredith: 'Status of experiments lesding to a small recirculator' Nuclear Instr. Methods, A-415, 310-314 (1998)

[5] Ken Takayama,Kunio Koseki et. al."Observation of Acceleration of a Single Bunch by Using the Induction Device in the KEK Proton Synchrotron"PRL 94,144801(2005)

[6] K.Takayama and J.Kishiro,Nucl. Inst. and Meth.A451/1,304-317(2000)

[7] R.O.Bangerter, Fusion Eng.Des.44(1998) 71

[8] Alex Fridman, "Owerview of Heavy Ion Fusion Accelerator Research in the U.S" American Institute of Fhysics 0-7354-0101-0/02(2002)

[9] Edward.P.Lee and J.Hovingh,American Institute of Fhysics Conference Priceedings,No249,PT.2,1713-1724(1992)

[10] T.Kikuchi, K.Horioka, M.Nakajima, S.Kawata,"Beam Dynamics during Longitudinal Bunch Compression of High Current Ion Beams", Nucl. Inst. and Meth., A577, 103-109 (2007)

Simulation on energy depostion process due to anisotropic fast electron transport in high density plasma

Wataru Sekine, Mitsuo Nakajima, Kazuhiko Horioka, and Tohru Kawamura
Department of Energy Sciences, Tokyo Institute of Technology, Nagatsuta 4259, Midori-ku, Yokohama, 226-8502, Japan

Energy deposition process by relativistic fast electrons produced by ultra-intense laser pulses is discussed. The process is calculated with a two dimensional Fokker-Planck simulation code including binary and collective collisions coupled with electromagnetic field. We focused on Velocity Distribution Function (VDF) dependence in the simulation. The results show that the spread angle of the fast electrons distribution affects energy depostion area and deposited energy is concentrated in the vicinity of the propagation axis of the fast electrons. It may be also suggested that self-pinch effect of a fast electron beam causes large deposition energy.

Keywords: Energy deposition process, Fast electrons, Fokker-Planck equation

I. INTRODUCTION

There are some interesting issues on Inertial Confinement Fusion (ICF) with Fast Ignition (FI) scheme [1,2]. In the scheme, an additional higher intensity laser pulse (10^{18-20}W/cm^2) is needed, and effective heating is caused by relativistic fast electrons produced by the laser pulse. The energy of the fast electrons is up to about a few tens MeV [3-5].

Main purpose in this study is to reveal energy deposition process from energetic electrons to a background bulk plasma coupled with electromagnetic field. Particularly, the dependence of anisotropic Velocity Distribution Function (VDF) of fast electrons on energy deposition is studied. The VDF is a function of position, velocity, and time namely, $f(r, v, t)$. For evaluating deposited energy, two dimensional Fokker-Planck simulation code has been developed including binary and collective collisions coupled with electromagnetic field.

II. DEVELOPMENT OF A FOKKER-PLANCK SIMULATION CODE

To describe the motion of fast electrons, kintetic method [6-8] is used. The advantage of the treatment of VDF is that the dependence of anisotropic VDF on energy deposition can be examined explicitly.

Fokker-Planck equation can be obtained as follows [9].

$$\frac{\partial f_{e(beam)}}{\partial t}+\frac{\boldsymbol{p}}{\gamma m_e}\cdot\nabla f_{e(beam)}+q\left(\boldsymbol{E}+\frac{\boldsymbol{p}}{\gamma m_e}\times\boldsymbol{B}\right)\cdot\frac{\partial f_{e(beam)}}{\partial \boldsymbol{p}}$$

$$=\sum_{j=e,i(bulk)} C_{\mathrm{FP}}(f_{e(beam)}, f_j)+C_{\mathrm{LB}}(f_{e(beam)}, f_{e(bulk)})+S, \tag{1}$$

where m_e is electron mass, γ is a Lorentz factor, $\boldsymbol{p}$ is momentum vector of fast electrons, $\boldsymbol{E}$ and $\boldsymbol{B}$ are electric and magnetic field, respectively. $f_{e(beam)}$ stands for the VDF of fast electrons, and $f_{e,i(bulk)}$ are for background electrons and ions. S means a source term.

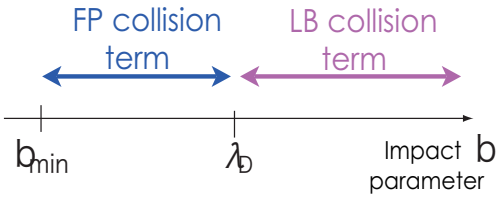

FIG. 1: FP collision term can be described in the range of $b \leq \lambda_D$,and LB collision term in $b \geq \lambda_D$. (b:impact parameter, λ_D:Debye length, b_{min}:minimum impact parameter)

C_{FP} of the right hand side stands for a Fokker-Planck (FP) collision term, which means binary collisions between fast electrons and bulk electrons or ions. C_{LB} of the right hand side stands for a Lenard Balescu (LB) collision term, which means collective collisions [10,11]. The collective collisions can describe Langmuir-wave excitation. Detailed description about two collision terms are reported in Ref.12-14. FIG.1 shows the domain of FP and LB collision terms respectively.

Electromagnetic field generated in plasma can be given by the Maxwell's equations.

$$\boldsymbol{J}=\boldsymbol{J}_f+\boldsymbol{J}_b, \tag{2}$$

$$\nabla\times\boldsymbol{B}=\mu_0\boldsymbol{J}, \tag{3}$$

$$\boldsymbol{E}=\eta\boldsymbol{J}_b, \tag{4}$$

$$\nabla\times\boldsymbol{E}=-\frac{\partial\boldsymbol{B}}{\partial t}, \tag{5}$$

where $\boldsymbol{J}_f$ is fast electron current density, and $\boldsymbol{J}_b$ is return current density of bulk electrons. It is assumed that the return current flows to keep current neutrality with fast electron current. η means background plasma resistivity [15].

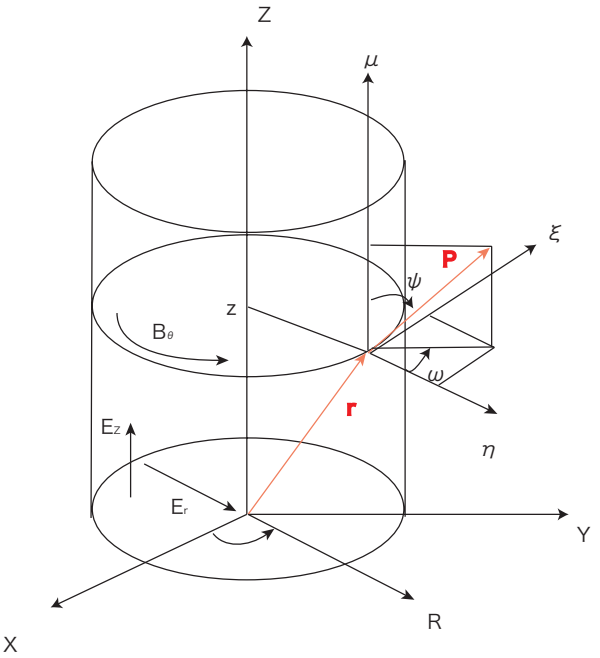

FIG. 2: Simulation system ($\boldsymbol{r}$ is a position vector, and $\boldsymbol{p}$ is a momentum vector.) Fast electrons are injected at $z = 0$ initially. Uniform plasma density and temperature are assumed.

III. SIMULATION CONDITIONS

A schematic drawing of a simulation system is presented in FIG.2. In the simulation, two dimensional cylindrical coordinate is adopted, and three dimensional spherical coordinate for momentum space [9].

Here, the initial plasma density is assumed to be 10^{29} m^{-3}, and plasma temperature is 300 eV. The simulation size is 24 μm in r-direction and 30 μm in z-direction. This size is large enough to describe energy deposition process by relativistic fast electrons.

The initial VDF of fast electorons can be given as follows.

$$f(\boldsymbol{r}, \boldsymbol{p}, t) = f(\boldsymbol{r}) f(\boldsymbol{p}) N(t). \tag{6}$$

$f(\boldsymbol{r})$ is assumed to be uniform in r-direction, and $N(t)$ is density of fast electrons and it is assumed to be constant as $10^{27}\mathrm{m}^{-3}$ In the next section, the dependence of energy deposition on the spread angle in the momentum space is discussed.

IV. SIMULATION RESULTS AND DISCUSSTION

At first, the fast electrons of 1MeV are injected at z=0 into plasma. Energy deposition rate P_{dep} is shown in FIGs.3-7. Here, P_{dep} includes deposited energy by collisions, and Joule heating by return current. FIG.3 shows

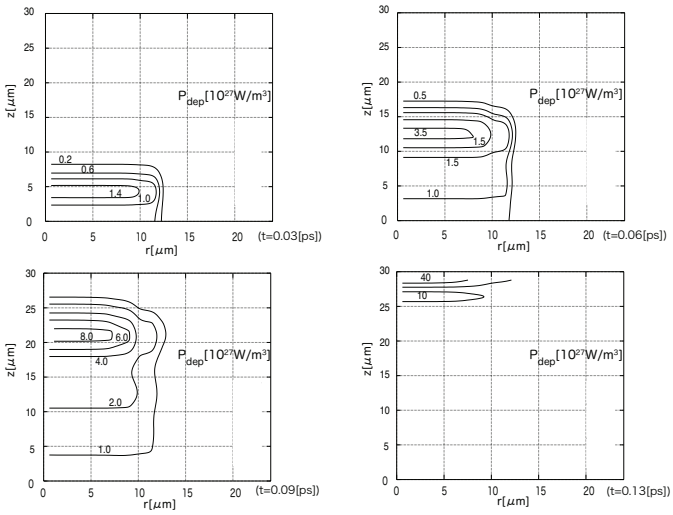

FIG. 3: Energy deposition rate at $\psi = 10°$

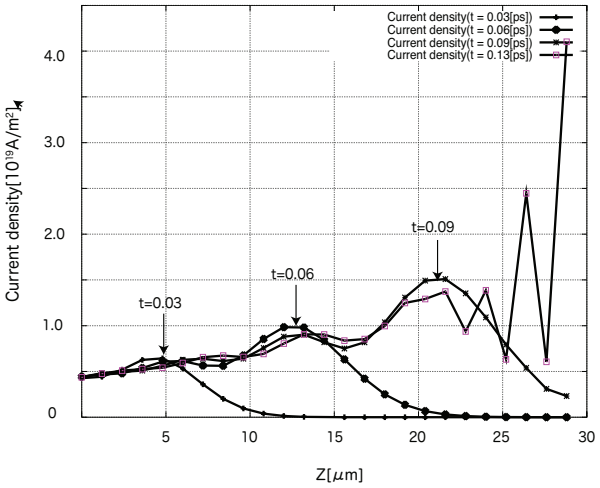

FIG. 4: Spatial profiles of the fast electron current density

a time evolution of the energy deposition rate with contour lines in r-z space, where $\psi = 10°$. P_{dep} is the order of $10^{27}\mathrm{W/m}^3$. FIG.4 shows the spatial profiles of the fast electron current density in the vicinity of the z-axis at $\psi = 10°$. An enhancement of fast electron current density is shown, and it is expected that the increase in the current density is due to the pinch effect of the fast electron beam by electomagnetic field. At the peak of P_{dep} in FIG.3 (t=0.06 ps and t=0.09 ps), the current density is the highest. It may be suggested that the self-pinch effect of the fast electron beam causes large deposition energy. FIG.5 shows energy deposition rate at $\psi = 30°$. The peak of P_{dep} moves into plasma along the z axis. FIG.6 and 7 show the energy deposition rate at $\psi = 50°$ and $\psi = 70°$, respectively. The peak depostion area is located near the incidence of the fast electron beam.

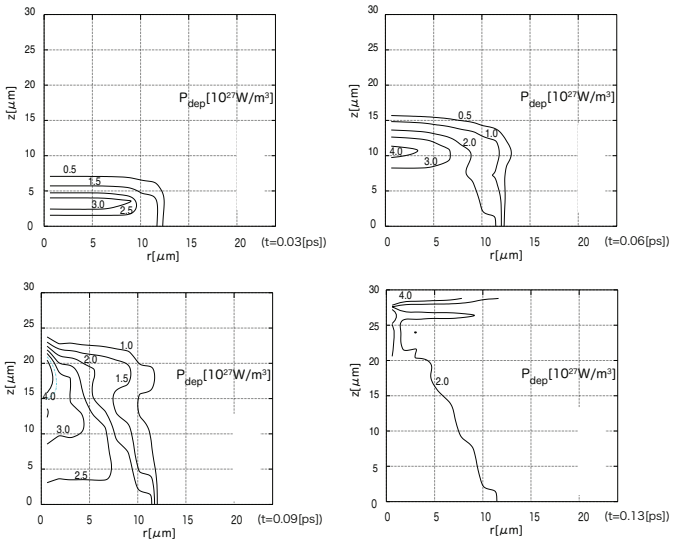

FIG. 5: Energy deposition rate at $\psi = 30^\circ$

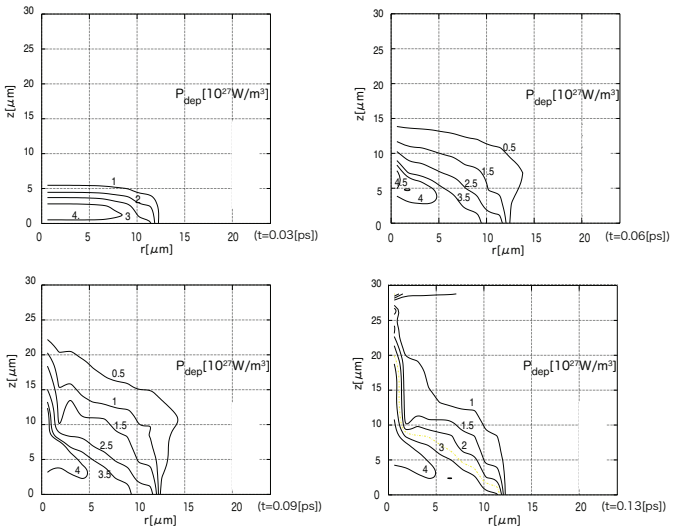

FIG. 6: Energy deposition rate at $\psi = 50^\circ$

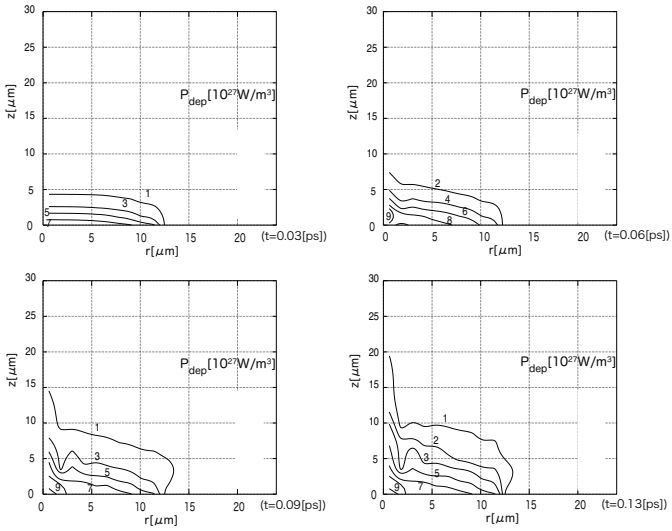

FIG. 7: Energy deposition rate at $\psi = 70^\circ$

V. CONCLUSIONS

Energy deposition by relativistic fast electrons relevant to fast ignition is studied. Two dimensional Fokker-Planck simulation code including binary and collective collisions coupled with electromagnetic field has been developed. As a result, deposited energy is concentrated in the vicinity of the propagation axis of the fast electrons, and the anisotropy of the fast electron transport is enhanced with increase in the spread angle of the fast electron motion in the momentum space. It may be also suggested that the self-pinch effect of a fast electron beam causes large deposition energy.

ACKNOWLEDGMENTS

One of authors (W.S.) would like to thank Prof. Makoto Shiho of Tokyo Institute of Technology for fruitful discussions.

[1] M. Tabak *et al.*, *Phys. Plasmas*, **1** (1996) 1626
[2] R. Kodama *et al.*, *Nature*, **412** (2001) 798
[3] Y. Sentoku *et al.*, *Phys. Rev. Lett.*, **90** (2003) 155001
[4] S. Atzeni, J. Meyer-ter-Vehn, *The physics of inertial fusion* (Clarendon press, Oxford, 2004)
[5] T. E. Cowan *et al.*, *Phys. Rev. Lett.*, **84** (2000) 903
[6] D. R. Nicholson, *Introducition to Plasma Theory* (John Wiley and Sons. Inc, New York, 1983)
[7] M. N. Rosenbluth, *et al.*, *Phys. Rev.* **107** (1951) 1
[8] F. F. Chen, *Introduction to plasma physics* (Plenum Press, New York, 1974)
[9] T. Yokota, Ph.D. thesis, University of Kyushu (2005)
[10] A. Lenard, *Ann Phys.* (New York) **10** (1960) 390
[11] R. Balescu, *Phys. Fluids*, **3** (1960) 52
[12] B. J. Braams and C. F. F. Karney, *Phys.Fluids*, *B***1** (1989) 7
[13] K. Nakashima and H. Takabe, *Phys. Plasmas*, **9** (2002) 1505
[14] H. van Erkelens, *Physica*, *A***107** (1980) 48
[15] L. Spitzer, Jr., *Physics of Fully Ionized Gases* (Wiley and sons, New York, 1962)

Quasi-uniform Tamped Target for Beam-driven Warm Dense Matter Experiments

Toru Sasaki,[1,*] Takashi Kikuchi,[2] Mitsuo Nakajima,[1] Tohru Kawamura,[1] and Kazuhiko Horioka[1]

[1] *Department of Energy Sciences, Tokyo Institute of Technology, Nagatsuta 4259, Midori-ku, Yokohama, 226-8502, Japan*

[2] *Department of Electrical and Electronic Engineering, Utsunomiya University, Yohtoh 7-1-2, Utsunomiya 321-8585, Japan*

A tamped target is proposed for making quasi-uniform warm dense matter using highly energetic heavy ion beams. The target is composed of two layers, in which an inner material is set to be low-Z low density matter, in contrast, an outer shell filled by high-Z high density matter. We compare hydrodynamic behaviors of a mono-layer target to the tamped target driven by modified KEK 500 MeV booster. Results show that both targets can reach a warm dense state. In particular, the tamped target can achieve well defined warm dense state with long scale. We also discuss diagnostics for the tamped target.

Keywords: warm dense matter, heavy ion beam, equation of state, high energy density physics, beam plasma interactions

I. INTRODUCTION

Properties of matters at warm dense state are of great interest concerning the interiors of giant planets and the hydrodynamics of fuel pellet of inertial confinement fusion (ICF)[1–4]. The structure and the dynamics are influenced by the equation of state (EOS) as well as the transport coefficients by coupled ions and degenerated electrons. In recent years, we are able to produce the warm dense state in a laboratory by some experimental methods (i.e., intense laser, exploding wire using pulsed-power discharges)[5–12]. A new approach using irradiation of heavy ion beams is also proposed by some research-groups in GSI[13, 14], virtual national laboratory (VNL)[15], and a group in KEK[16]. One of important points of warm dense state measurements is to keep a consistency in determination of the thermodynamic state (i.e., density, temperature, and pressure).

The intense ion beams have advantages; they can deposit their energy with good uniformity over an extended volume. Also the stopping power in materials is basically well known with high accuracy and is insensitive to details of the chemical structure. In addition to the warm dense matter (WDM) and high energy density physics (HEDP) studies by using ion beams, the beam energy should be focused in a local area of the target to make the higher energy density state. The beam power is proportional to the kinetic energy and the beam current. The higher kinetic energy causes the longer stopping range in the target. Therefore, WDM study using intense highly energetic beam can easily evolve the matter's physical parameters in large scale length. However, for observing physical parameter, the target should be in equilibrium and uniform.

In this study, we propose to make a quasi-uniform and large scale target using highly energetic beams. For measuring physical parameters of WDM, the target structure should be as simple as possible. For evaluating the uniformity of large scale target, the behavior of WDM target should be evaluated by using two dimensional hydrodynamics simulation including beam deposition process. Additionally, we concerned how to observe the target physical parameters and achievable parameter region of warm dense matter using an induction synchrotron KEK modified 500 MeV booster.

II. BEAM PARAMETERS AT KEK MODIFIED 500 MEV BOOSTER

An ion accelerator, modified KEK 500 MeV booster using induction synchrotron technology, is under consideration as an all-ion accelerator [17]. This accelerator is capable of generating an extremely long bunch, which stores the beam particle under the space-charge limit in transverse direction and the ring size, using fast switching power supply. Therefore, the property of the induction modulators brings us a significant freedom of beam handling, and greatly extends the available longitudinal phase space of charged particles [18, 19]. The induc-

*Electronic address: sasaki@es.titech.ac.jp

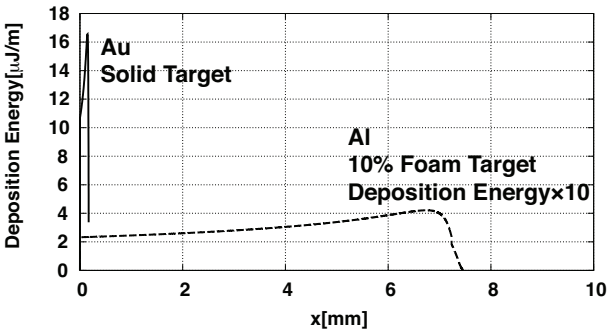

FIG. 1: Deposition profiles of uranium projectile in solid gold target and in aluminum foam target at room temperature.

tion synchrotron has a potential for various applications, for example, the super-bunch hadron collider, a proton driver for the second generation of neutrino oscillation experiment, materials modification and direct processing, WDM, and HEDP study, etc.. In particular, research on WDM and HEDP topics need a broad parameter range. Ease of changing the species and controlling the energy of ion beam are advantages for extending the parameter regime in WDM and HEDP study.

The modified booster is expected to be able to provide about 10^{10} uranium ions having an energy of a 500 MeV/u. For the WDM study, the provided ion beams should be compressed longitudinally and also in transverse direction at the final stage. The ion beam is focused order of a few hundred μm radius with a few mm range using half mini-beta system. The longitudinal direction is compressed up to about 100 ns from the modified 500 MeV booster to the target chamber.

III. RESULTS AND DISCUSSIONS

A. Simulation model

The dynamics in the target is given by the following fluid equations of mass, momentum, and energy conservations:

$$\frac{\partial \rho}{\partial t} + (\boldsymbol{u} \cdot \nabla)\, \rho = -\rho \nabla \cdot \boldsymbol{u} \tag{1}$$

$$\frac{\partial \boldsymbol{u}}{\partial t} + (\boldsymbol{u} \cdot \nabla)\, \boldsymbol{u} = -\frac{\nabla p}{\rho} \tag{2}$$

$$\frac{\partial T}{\partial t} + (\boldsymbol{u} \cdot \nabla)\, T = -\frac{p_{\rm th} \nabla \cdot \boldsymbol{u}}{\rho C_v} + \frac{E_{\rm dep}}{\rho C_v} \tag{3}$$

where ρ is the density, $\boldsymbol{u}$ is the velocity, T is the temperature, p is the pressure, $p_{th} = T\,(\partial p/\partial T)_\rho$, $C_v = (\partial e/\partial T)_\rho$ is the specific heat, and E_{dep} is the deposition energy from the beam, respectively. We calculate the hydrodynamics of target with two dimensional cylindrical r-z geometry using the cubic interpolated pseudo-particle combined unified procedure (CIP-CUP) method[20]. The method can treat compressible and incompressible fluids simultaneously without employing any special boundary conditions. To solve the hydrodynamic motion, the QEOS[21] is used. The thermal and radiation transport are neglected in present study. These transports and

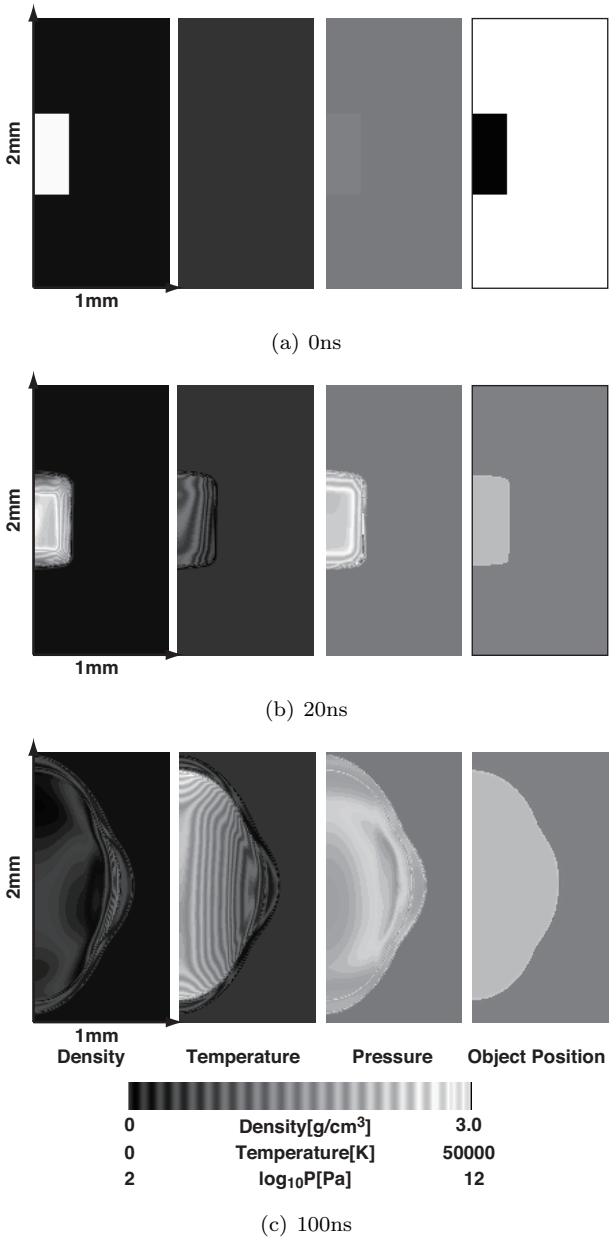

FIG. 2: Evolution of mono-layer target induced by heavy ion beam irradiation.

EOS are the unclearified part for warm dense state, and a sophisticated modeling will be made through a semi-empirical fitting of the hydrodynamics.

The energy deposition of heavy ions was calculated using a stopping power. We used a well-known expression for the effective charge of the heavy ion beam presented in Refs.[22] and [23]. The stopping power $E_{\rm stop}$ of a target includes the energy deposited in target nuclei $E_{\rm nucl}$, bound electrons $E_{\rm bound}$, free electrons $E_{\rm free}$, and ions $E_{\rm ion}$[24] as:

$$E_{\rm stop} = E_{\rm nucl} + E_{\rm bound} + E_{\rm free} + E_{\rm ion}. \quad (4)$$

To coupled with fluid equation (3), the specific deposition energy $E_{\rm dep}$ is derived from the stopping power $E_{\rm stop}$ along the z-direction as:

$$E_{\rm dep} = \frac{E_{\rm stop}\Delta z}{V} \quad (5)$$

where Δz is the mesh distance of z-direction, and V is the volume of the mesh.

In this calculation, the beam radius is set to be 350 μm with a Gaussian distribution, and the beam longitudinal profile is assumed to be rectangle with Kapchinskij-Vladimirskij distribution. The expected beam emittance growth at radial direction is estimated to be about 35 μm using 5 mm target length. We assumed that the target radius to be 250 μm, which was bigger than the shifts at radial direction. Therefore, we neglected the transverse beam emittance. The emittance of longitudinal direction shifted the peak deposition point. We estimated that if the 500 MeV/u uranium beam has 10% longitudinal emittance, the peak deposition point extends about 50μm using aluminum 10% foam target. We can neglect the shift of the deposition profile for those targets.

Figure 1 shows a comparison of the deposition profile of gold with solid density and 10% aluminum in room temperature foam using uranium ion projectile with 500 MeV/u. As shown, the 10 % aluminum foam target is expected to be able to make a large scale and quasi-uniform state in combination with gold solid target. To evaluate uniformity and the scale length, we calculate the hydrodynamic behaviors of a mono-layer target and a tamped target.

B. Mono-layer target

We calculate a beam driven cylindrical aluminum target. The target is initially 250 μm in radius and 600 μm in length. The behavior of mono-layer target is shown in Fig. 2. Figure 2 (a) illustrates the initial density, temperature, pressure, and object position, respectively. As shown in Fig. 2 (c), at 100 ns, we can see the strong density gradient in radial direction at the target center. The target temperature increased up to 4 eV at 100 ns. At 100 ns, the mono-layer aluminum target becomes 1.75mm in length, and 650 μm in radius. The target size increased about three times compared to that of the initial value.

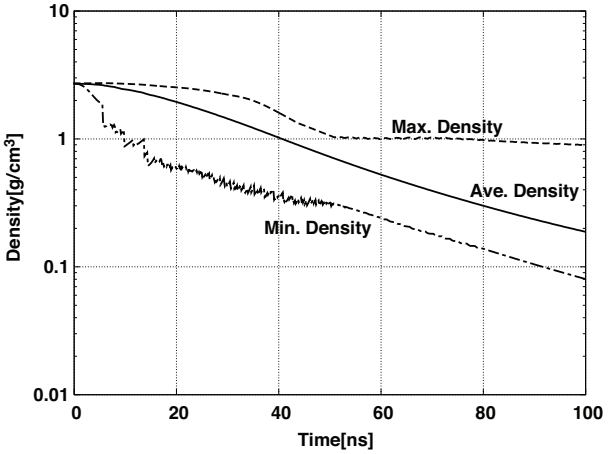

FIG. 3: Time evolution of average density, maximum density, and minimum density on a mono-layer aluminum target.

Figure 3 shows the evolutions of maximum, minimum, and average density. The minimum and the maximum density behaviors are different until 50 ns. After 50 ns, the reduction of maximum density settles at about 1 g/cm^3. However, the minimum density decreased to 0.1 g/cm^3. The reason of the different minimum and maximum density evolutions are that the target radius is bigger than the beam radius. The irradiated region became higher temperature and pressure compared with the unirradiated region. Therefore, the irradiated region can expand with the density reduction. The two-dimensional hydrodynamic simulation shows that the mono-layer target makes complex structure as shown in Figs. 2 (c) and 3.

C. Tamped target

Since the deposition profile of aluminum foam is uniform as shown Fig. 1, the tamped target is expected to be able to make a large scale, quasi-uniform structure during and after beam irradiation. The initial size of the target of aluminum foam is 250 μm in radius and

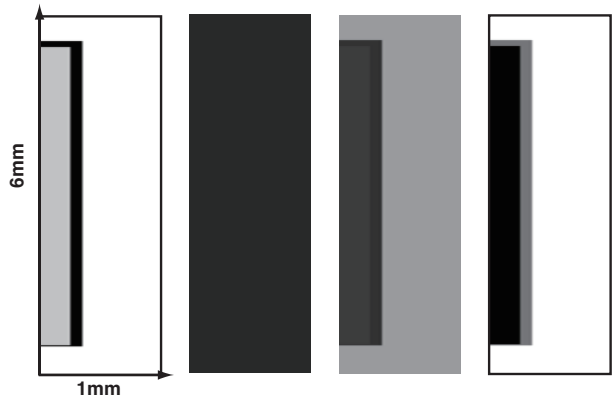

(a) 0ns

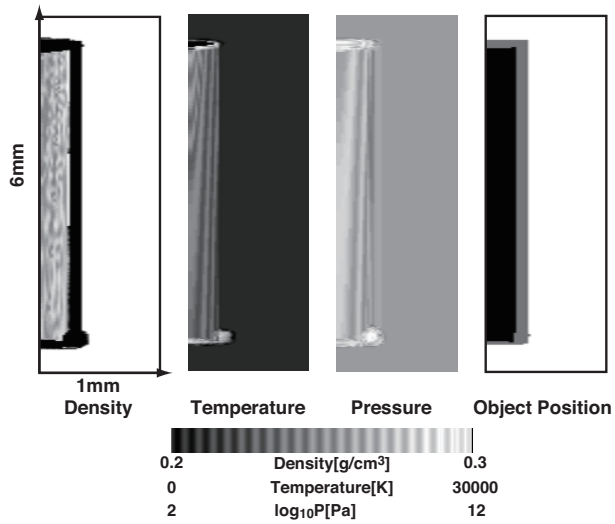

(b) 20ns

FIG. 4: Evolution of tamped target behaviors for formation of dense, uniform condition.

5 mm in length. The aluminum foam is coated by the gold with solid density, which is 20 μm in thickness for a part of beam injection, and is 100 μm in thickness for the other part. A preliminary result of hydrodynamic simulation for a beam driven cylindrical tamped target is shown Fig. 4. The behavior of target is shown in Fig. 4. Fig. 4 (a) show the initial density, temperature, pressure, and object position, respectively. As shown in Fig. 4 (b), the density profile of aluminum foam have uniform around 0.27 g/cm^3. Comparing Fig. 2 (b) with 4 (b), the tamped target can keep the quasi-uniform region until 20 ns from the beam input. This means the tamped target enable us to observe the long scale (4 mm) WDM.

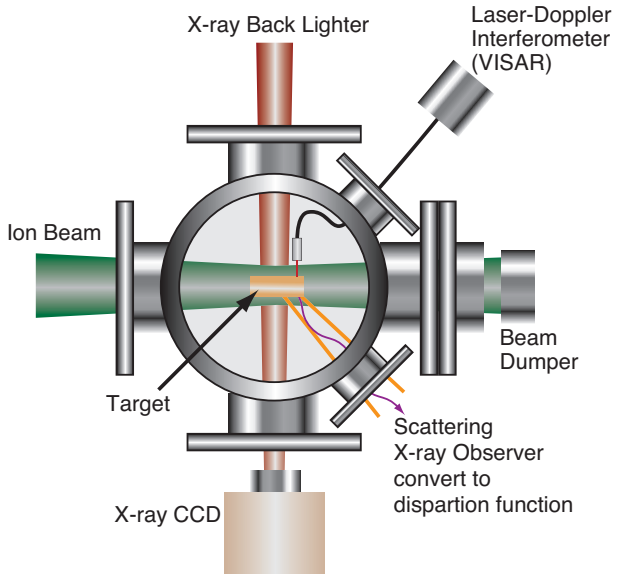

FIG. 5: A sketch of expected beam irradiation experiments for WDM studies using tamped target.

D. Diagnostic method

A sketch of expected beam irradiation experiments for WDM studies is shown in Fig. 5. An X-ray CCD with X-ray back lighter observes target hydrodynamic behaviors. A VISAR system observes dynamic pressure at tamper surface. The target temperature can be controlled by beam parameters. Recently, plasmons was observed in WDM using high power laser experiments by scattering X-ray.[11] Electron temperature and density are estimated by X-ray spectroscopy. However, those diagnostic methods are not yet sophisticated for reliable evaluation of the target's physical parameters. For determining the parameters, we should also seek to find a target structure to ease the estimation, like a exploding wire device in water. Additionally, we should study to control the achievable warm dense state by the beam parameters.

IV. CONCLUSION

We proposed a tamped target for making a quasi-uniform warm dense state based on highly energetic ion beam irradiation. For the estimation of target hydrodynamics, two dimensional cylindrical hydrodynamic code including ion beam deposition profile was developed. The results show the target can reach a warm dense state with the induction synchrotron modified from KEK 500 MeV

booster. The tamped target can make a quasi-uniform profile with 4 mm in length. We also discussed the diagnostics using the tamped target. For determining the parameters, we should design an appropriate target structure, for making a dense, uniform state. Additionally, we should study to control the achievable warm dense state by the beam parameters. We are planning to evaluate the EOS model from comparative study of the hydrodynamic behaviors. We also concern the possibility of programmed target heating with the induction synchrotron.

ACKNOWLEDGMENTS

This work was partly supported by the Grant-in-Aid of the ministry of education, science and culture of Japan.

[1] R. C. Davidson, ed., *Frontiers in High Eneregy Density Physics* (NATIONAL ACADEMIES, 2003).
[2] S. Ichimaru, H. Iyetomi, and S. Tanaka, Phys. Rep. **149**, 91 (1987).
[3] J. Lindl, Phys. Plasma **2**, 3933 (1995).
[4] T. Someya, A. I. Ogoyski, S. Kawata, and T. Sasaki, Phys. Rev. ST AB **7**, 044701 (2004).
[5] P. Renaudin, C. Blancard, G. Faussurier, and P. Noiret, Physical Review Letters **88**, 215001 (2002).
[6] I. Krisch and H. J. Kunze, Phys. Rev. E **58**, 6557 (1998).
[7] S. Saleem, J. Haun, and H. J. Kunze, Phys. Rev. E **64**, 056403 (2001).
[8] T. Sasaki, M. Nakajima, T. Kawamura, and K. Horioka, Journal of Plasma Fusion Research **81**, 965 (2005).
[9] T. Sasaki, Y. Yano, M. Nakajima, T. Kawamura, and K. Horioka, Laser and Particle Beams **24**, 371 (2006).
[10] H. Yoneda, H. Morikami, K. Ueda, and R. M. More, Phys. Rev. Lett. **91**, 075004 (2003).
[11] S. H. Glenzer, O. L. Landen, P. Neumayer, R. W. Lee, K. Widmann, S. W. Pollaine, R. J. Wallace, G. Gregori, A. Holl, T. Bornath, et al., Physical Review Letters **98**, 065002 (2007).
[12] T. Sasaki, Y. Yano, M. Nakajima, T. Kawamura, and K. Horioka, Nuclear Instruments and Method A (to be published).
[13] E. Dewald, C. Constantin, S. Udrea, J. Jacoby, D. Hoffmann, C. Niemann, J. Wieser, N. Tahir, A. Kozyreva, A. Shutov, et al., Laser and Particle Beams **20** (2002).
[14] A. Kozyreva, M. Basko, T. schlegel, A. Tauschwiz, and D. H. H. Hoffmann, Physical Review E **68**, 056406 (2003).
[15] L. R. Grisham, Physics of Plasmas **11**, 5727 (2004).
[16] K. Horioka, M. Shiho, T. Kawamura, M. Nakajima, T. Sasaki, K. Kondo, Y. Yano, T. Ishii, M. Ogawa, Y. Oguri, et al., in *Proceedings of The 2nd International Workshop on Recent Progress in Induction Accelerators (RPIA2006)* (2006), pp. 11–15.
[17] K.Takayama, Y.Arakida, T.Dixit, T.Iwashita, T.Kono, E.Nakamura, K.Otsuka, Y.Shimosaki, K.Torikai, and M.Wake, Phys. Rev. Lett. **98**, 054801 (2007).
[18] K. Horioka, M. Nakajima, M. Watanabe, M. Honda, E. Hotta, M. Shiho, M. Ogawa, J. Hasegawa, J. Kishiro, and K. Takayama, Laser and Particle Beams **20**, 609 (2002).
[19] P. K. Roy, S. S. Yu, E. Henestroza, A. Anders, F. M. Bieniosek, J. Coleman, S. Eylon, W. G. Greenway, M. Leitner, B. G. Logan, et al., Phys. Rev. Lett. **95**, 234801 (2005).
[20] F. Xiao, T. Yabe, T. Ito, and M. Tajima, Comput. Phys. Comm. **102**, 147 (1997).
[21] R. M. More, K. H. Warren, D. A. Young, and G. B. Zimmerman, Phys. Fluids **31**, 3059 (1988).
[22] T. Peter and J. Meyer-ter Vehn, Physical Review A **43**, 1998 (1991).
[23] T. Peter and J. Meyer-ter Vehn, Physical Review A **43**, 2015 (1991).
[24] T. A. Mehlhorn, J. Appl. Phys. **52**, 6522 (1981).

Evaluating Conductivity of Warm Dense Matter using Wire Discharges in Water

Yuuri Yano, Toru Sasaki, Mitsuo Nakajima, Tohru Kawamura, and Kazuhiko Horioka*
Department of Energy Sciences, Tokyo Institute of Technology,
Nagatsuta 4259, Midori-ku, Yokohama, 226-8502, Japan

A method of measurements for electrical conductivity of matter is established in a warm dense region. Warm dense matter (WDM) is produced using wire discharges in water, and the state of matter is characterized by measurements of the density and the temperature. The experimentally obtained electrical conductiviy is compared with the Spitzer, the Lee-More, and the Ichimaru formulae. Result shows that, in the high density regime, the experimental data for conductivity of copper can not be explained well by the aforementioned models.

Keywords: Electrical Conductivity, Pulse-Power, Warm Dense Matter, Wire Explosion

I. INTRODUCTION

All of the state of matter can be defined in a density-temperature diagram. However in low temperature and high density regime(-10^5K, 10-10^4g/m^3), appropriate models are not yet established to describe the equation of state and transport coefficients. Materials in this regime is characterized as Warm Dense Matter (WDM). When we heat a solid, the matter evolves from solid to a plasma through a warm dense state. Therefore, when we study the evolution of matter in a broad parameter region, it is crucially important to study the WD state.

Properties of matter in a warm dense state are of interest concerning interiors of giant planet (e.g., Jupiter) and hydrodynamics of the fuel pellet of inertial confinement fusion. In the WDM, accurate experimental data are lacking. Therefore, we would like to get experimental data and make a scaling law, in particular, electrical conductivity of the WDM. To make the scaling law, it is important to estimate the electrical conductivty as a function of temperature and density over a wide parameter region.

In recent years, we are able to produce the WDM in a laboratory by some experimental methods ([3][10][11][13][14][15][16][17][21]). They are based on the way to use irradiation of ultra-short laser pulse, a plasma formation in isochoric vessels and a wire explosion using pulsed dishcarges. A new approach using irradiation of heavy ion beam is also proposed by research groups at GSI ([1][4][7][6][19][20]), VNL; virtual national laboratory ([2][5]), and KEK[8]. They are planning to study the high energy density and WDM physics, based on a beam heated plasma target with well-defined energy deposition region or the Bragg-peak region.

There are two main topics in this study. Firstly, we point out that the state of matter should be well defined by two thermodynamical variables; density, temperature and/or pressure. Under the well defined condition, we can establish a method for evaluating the electrical conductivity. Secondary, we compare the experimental electrical conductiviy with available models, and the applicability of them in WDM regime is discussed. The WDM is produced using pulse-powered exploding wire discharges in water. Electrical conductivity and density of the plasma are estimated by the experimentally obtained voltage, current and the hydrodynamic evolution of the wire explosion. Temperature of the plasma is estimated via spectroscopy. With this method, we can define the state of the WDM almost accurately over a wide range of parameter region on density-temperature diagram.

II. EXPERIMENTAL METHOD AND SETUP

Figure 1 is a schematic diagram of the experimental setup for wire discharges in water. When the pluse power drive the current in the wire, it is Joule heated and evaporates. The hot dense gas explodes accompanied by a cylindrically propagating shock wave in water. Next to the expansion, discharge is induced in the gas and the wire evolves to a plasma.

Experimental setup is shown in Figure 2. A capacitor bank; C consists of cylindrically arranged $8 \times 0.4\mu$F low inductance capacitors. The stray inductance is estimated to be 105nH and the electric discharge voltage is typically 10kV to ensure vaporization of wire. The discharge is controlled by a gap switch and a thyratron pulser. We used Tungsten or copper wire with 24.5mm in length and 25 or 50 μm in radius. The skin depth is estimated to be larger than the radius of wire, during the discharge time.

Advantages of this device is as follows; 1 Axial symmetry plasma is generated. 2 Density of the plasma can be maintained by the tamping effect of water. 3 Plasma resistivity and input energy can be measured directly using the waveforms of current and voltage. 4 Conductivity data can be measured in a wide parameter regime by changing a condition of wire discharge. 5 The density, the temperature, and the conductivity of plasma can be simultaneously obtained in one shot.

*Electronic address: khorioka@es.titech.ac.jp

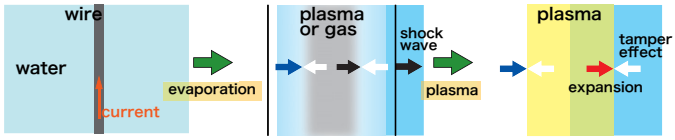

FIG. 1: Schematic diagram of wire discharges in water

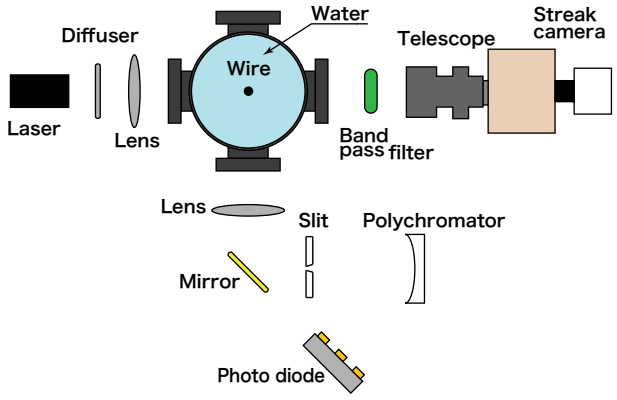

FIG. 2: Top view of experimental setup

The expansion of plasma is observed by a streak of shadow imaging. Using it and Eq.(1), the density of plasma is estimated;

$$\rho_{wire}(t) = \left(\frac{r_0}{r_{wire}(t)}\right)^2 \rho_0, \tag{1}$$

where r_0 is initial radius of plasma, and $r_{wire}(t)$ is the radius of plasma, and ρ_0 is initial density of plasma, and $\rho_{wire}(t)$ is the density of plasma.

The time evolution of input energy $E_{input}(t)$ can be estimated by the following equation (2),

$$E_{input}(t) = \int_0^t \left(V(t) - L\frac{dI(t)}{dt}\right) I(t)dt, \tag{2}$$

where V(t) is the voltage, I(t) is the current, L is the circuit inductance.

The current I(t) and the voltage V(t) are measured by a Rogowski coil and a high voltage probe. Using them, the value of plasma resistance is directly estimated. However, the experimentally obtained voltage is contain inductive contribution. Thus, the effective resistance $R_{wire}(t)$ of plasma is estimated using the next equation;

$$R_{wire}(t) = \frac{V(t) - LdI(t)/dt}{I(t)}. \tag{3}$$

The electrical conductivity $\sigma(t)$ is estimated using Eq.(3), and expansion of plasma using the following equation;

$$\sigma(t) = \frac{1}{R_{wire}(t)} \frac{l}{\pi(r_{wire}(t))^2}, \tag{4}$$

where $R_{wire}(t)$ is the radius of plasma, and l is the length.

Plasma temperature is estimated from intensity ratio of plasma light emission. To measure the ratio, a spectrometer is made using a flat field grating (Shimadzu Corporation) and photodiode (S5971: Hamamatsu Photonics). The light emission was measured at 458nm and 658nm. The wavelength is calibrated by a laser (frequency doubled YAG; $\lambda = 632$nm). The spectral sensitivity is calibrated by a xenon lamp (L7810: Hamamatsu Photonics). In the experiment, plasma emission is focused on the slit with 0.3mm width.

The emission intensity can be

$$B(\lambda, T) = \frac{2hc^2}{\lambda^5} \frac{1}{e^{hc/k_B T\lambda} - 1}, \tag{5}$$

where λ is wavelength, c is the speed of light, h is the Planck's constant, k_B is the Bolztmann constant, and T is temperature.

III. RESULTS AND DISCUSSIONS

Figure 3 shows typical waveforms of current and voltage, and Figure 4 is a streak-shadow image of copper wire explosion taken by the streak camera. Figure 5 shows typical input energy history of copper plasma. The wire length is 24.5mm, and the radius is 50μm. As shown in Figure 3, waveform of the current has two peaks. The first peak corresponds to liquid-vapor phase transiotion.

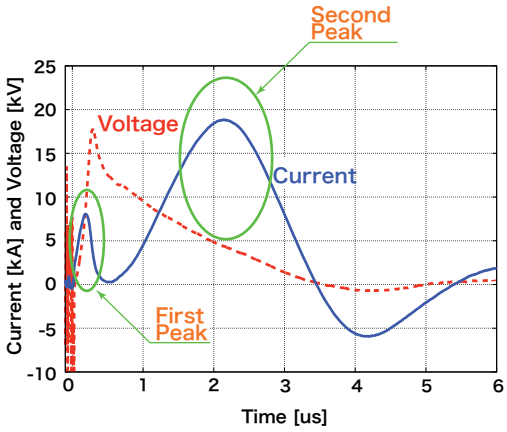

FIG. 3: Typical waveforms of current and voltage

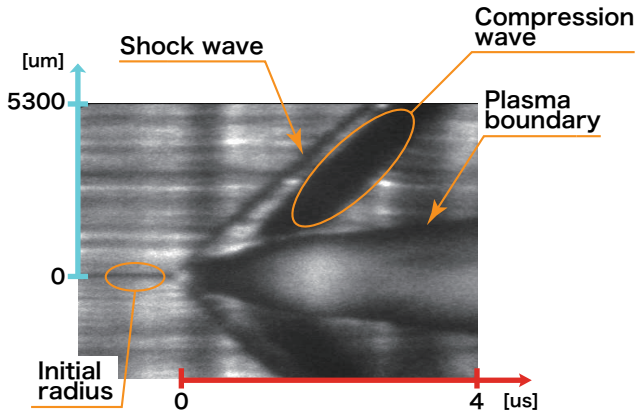

FIG. 4: Streak image of the wire explosion

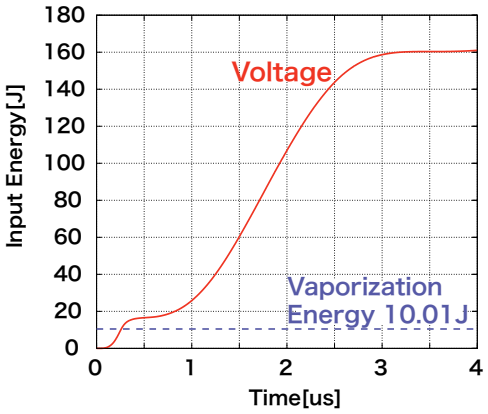

FIG. 5: Typical input energy history of copper plasma

As shown in Figure 5, the integrated input energy of copper plasma arrives at evaporation energy at 0.2 μs discharge time. In this timing, evaporation of wire is observed from Figure 4, and shock wave is driven in water. The wire is considered to be dense weakly ionized plasma. The current increases again and the wire gas evolves to a warm plasma at the second peak in Figure 3. As shown in Figure 4, the current increase drives compression waves in the shock compressed region.

The spectrum of plasma emission is observed using a fast framing camera and analyzed assuming local thermodynamic equilibrium (LTE) condition. Figure 6 shows the emission spectra at discharge time of 2μs, 3μs and 4μs. The visible light of plasma is observed between 500nm and 550nm. Thin copper plasma has line emissions at 510nm, 515nm and 521nm. However, the broad spectrum is observed as shown in Figure 6. Therefore, we concluded that LTE can be assumed at observed time. The plasma temperature can be estimated using the wavelength intensity ratio of plasma emission based on Eq.5.

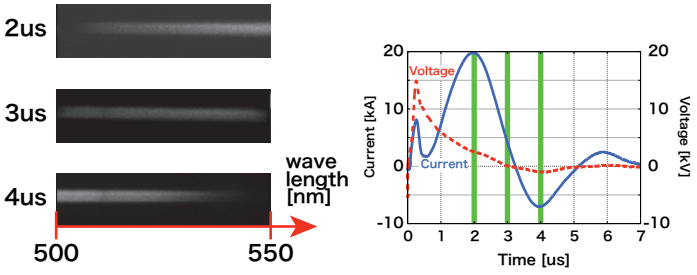

FIG. 6: Typical spectrum of Cu plasma

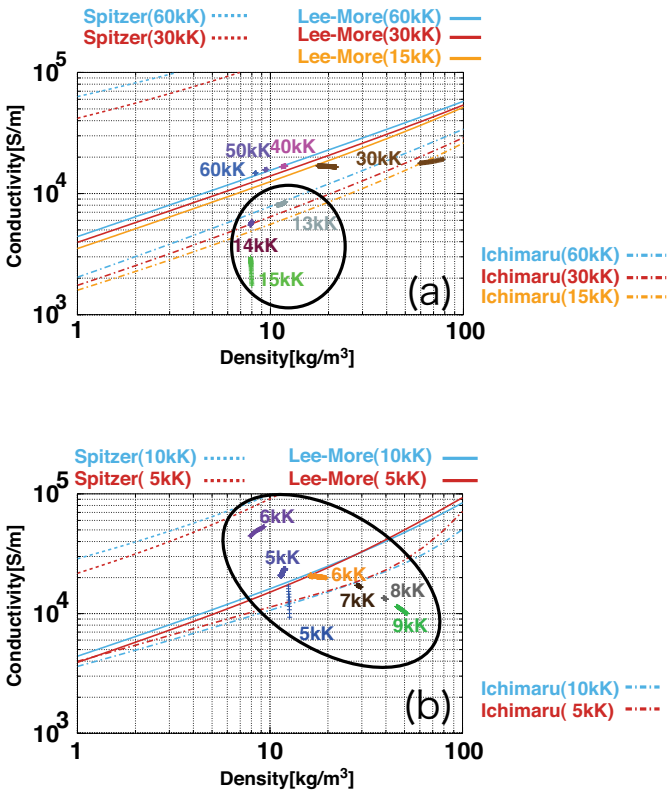

FIG. 7: Comparison of measured conductivity and theoritical one for (a) tungsten (b) copper

Figure 7 (a) and (b) show the conductivities in density-coductivity diagrams. They show the comparison of experimental results with theoretical estimation based on the Spitzer[18], the Lee-More[12], and the Ichimaru[9] formulae. The plots show experimental results, and numbers at the side of plots show the temperature, for tungsten in Figure 7 (a) and copper (b) respectively. At high temperature, the measured conductivity almost consistent with the Lee-More model as shown in Figure 7 (a). When temperature decreases, the measured one approaches to the Ichimasu model. However, the quantitative behavior of measured conductivity can not be explained by the conventional models in the

whole parameter region. In case of copper, the measured values do not consistent with conventional conductivity models. The measurements also indicate that the temperature dependence is much stronger than the model predictions.

IV. CONCLUSION

In this study, copper and tungsten plasma in warm dense state are produced using pulse-power discharges in water. A method of electrical conductivity measurement is established under the well-defined condition. In the estimation, the state of matter is well defined by temperature and density measurements. The density of plasma is estimated by time evolution of the plasma boundary using streak camera. The temperature of plasma is estimated via spectroscopy. The electrical conductivity of plasma is estimated by the waveforms of current and voltage, and the evolution of plasma boundary, together with the temperature measurements.

Results show that in the high density regime (-$10 \mathrm{kg/m^3}$), the experimental conductivity data reveal that conductivity of copper and tungsten can not be explained well using conventional conductivity models, probably because of an unclarified WD effect.

Efforts to make more detailed data base and consideration of more sophisticated model based on them are the issues of future works.

[1] Constantin, C., Dewald, E., Niemann, C., Hoffmann, D.H.H., Udrea, S., Varentsov, D., Jacoby, V., Funk, U.N., Neuner, U. & Tauschwitz, A. 2004. Laser Part. Beams 22, 59-63.

[2] Davidson, R.C. (2003). The National Academies Press.

[3] DeSilva, A.W. & Katsouros, J.D. (1999). Internat. J. Thermophys. 20, 1267-77

[4] Dewald, E., Constantin, C., Udrea, S., Jacoby, J., Hoffmann, D.H.H., Niemann, C., Weiser, J., Tahir, N.A., Kozvreva, A., Shutov, A. & Sinars, D.B. (2001). Laser part. Beams 20, 399-403.

[5] Grisham, L.R. (2004). Phys. Plasmas 11, 5727-5729.

[6] Hoffmann, D.H.H., Blazevic, A., Ni, P., Rosmej, O., Roth, M., Tahir, N.A., Tauschwitz, Y. (2005). Laser Part. Beams 19, 377-391.

[7] Hoffmann, D.H.H., Fortov, V.E., Lomonosov, I.V., Mintsev, V., Tahir, N.A., Varentov, D. & Wieser, J. (2002) Phys. Plasmas 9, 3651-3654.

[8] Horioka, K., Shiho, M., Kawamura, T., Nakajima, M., Sasaki, T., Kondo, K., Yano, Y., Ishii, T., Ogawa, M., Oguri, Y., Hasegawa, J., Kawata, S., Kikuchi, T., Takayama, K., Torikai, K. (2006). Proceedings of RPIA 2006, 11-15.

[9] Ichimaru, S., Iyetomi, H. & Tanaka, S. (1987). Phys. Rep., 149:91

[10] Krisch, I. & Kunze, H.J (1998). Phys. Rev. E 58, 6557-6564.

[11] Lee, R.W., Balidis, H.A., Cauble, R.C., Landen, O.L., Wark, J.S., Ng, A., Rose, S.J., Lewis, C., Riley, D., Gauthier, J.C. & Audebert, P. (2002). Laser Part. Beams 20, 527-536.

[12] Lee, Y.T. & More, R.M. (1987). Phys. Fluids, 27:1273

[13] Ng, A., Ao, T., Perrot, F., Dharma-Wardana, M.W.C. & Foord, M.E. (2005). Laser Part. Beams 23, 527-537.

[14] Renaudin, P., Blancard, C., Faussurier, G. & Noiret, P. (2002). Phys. Rev. Lett. 88, 215001-1-4.

[15] Saleem, S., Haum, J. & Kunze, H.J. (2001). Phys. Rev. E. 64, 056403-1-6.

[16] Sasaki, T., Nakajima, M., Kawamura, T., & Horioka, K. (2005). Plasmas Fus. Res. 81, 965-966.

[17] Sasaki, T., Yano, Y., Nakajima, M., Kawamura, T., Horioka, K. (2006). Laser Part. Beams 24, 371-380.

[18] Spitzer, L., Jr. & Harm, R. (1953). Phys. Rev. 89, 977-981.

[19] Tahir, N.A., Udrea, S., Deutsch, C., Fortov, V.E., Grandjouan, G., Gryazonv, V., Hoffmann, D.H.H., Hulsmann, P., Kirk, M., Lomonosov, I.V., Piriz, A.R., Shutov, A., Spiller, P., Temporal, M. & Varentov, D. (2004). Laser Part. Beams 22, 485-493.

[20] Temporal, M., Lopez-Cela, J.J., Piriz, A.R., Grandjouan, N., Tahir, N.A. & Hoffmann, D.H.H. (2005). Laser Part. Beams 22, 137-142.

[21] Yoneda, H., Morikami, H., Ueda, K. & More, R.M. (2003). Phys. Rev. Lett. 91, 075004-1-4.